Magnetic Resonance of Hyperpolarised Helium-3 at Low Magnetic Fields

Kayum Safiullin

To cite this version:

Kayum Safiullin. Magnetic Resonance of Hyperpolarised Helium-3 at Low Magnetic Fields. Medical Physics [physics.med-ph]. Université Pierre et Marie Curie - Paris VI, 2011. English. NNT : . tel-00753219

HAL Id: tel-00753219
https://theses.hal.science/tel-00753219

Submitted on 18 Nov 2012

UNIVERSITÉ PARIS 6 - PIERRE ET MARIE CURIE

Département de Physique **Laboratoire Kastler Brossel**
École Normale Supérieure

THÈSE de DOCTORAT de l'UNIVERSITÉ PARIS 6
Spécialité : Physique

présentée par

Kayum SAFIULLIN

pour obtenir le grade de DOCTEUR de l'UNIVERSITÉ PARIS 6

Magnetic Resonance of Hyperpolarised Helium-3 at Low Magnetic Fields

---

Soutenue le mardi 27 09 2011
devant le jury composé de :

M. Pierre-Jean NACHER................. Directeur de thèse
M. Claude FERMON......................... Rapporteur
M. Yannick CREMILLIEUX............ Rapporteur
M. Jean-Michel RAIMOND............. Examinateur
M. Luc DARRASSE........................... Examinateur
M. Jim WILD...................................... Examinateur
M. Murat TAGIROV......................... Examinateur

M. Zbigniew OLEJNICZAK............ Membre invité

Résumé

Dans ce travail nous avons étudié le problème du rapport signal à bruit (RSB) en IRM à très bas champ magnétique et exploré des applications potentielles en utilisant du gaz ^{3}He hyperpolarisé. Nous avons comparé deux méthodes d'élargissement de bande passante sans perte de RSB : une contre-réaction et un couplage inductif de la détection. Nous avons mis en oeuvre la contre-réaction, plus appropriée à très bas champ. Des mesures d'atténuation par diffusion dans un gaz d'^{3}He en géométrie cylindrique ont été faites par échos multiples de spin ou de gradient dans une large gamme de conditions correspondant à la diffusion dans les voies aériennes des poumons. Un bas champ permet d'utiliser des faibles gradients sur des durées longues, sans influence de la susceptibilité des matériaux. Nos mesures fournissent un ensemble de données destiné à une comparaison directe avec des modèles théoriques et d'autres résultats publiés. Une nouvelle séquence (Slow Low Angle Shot, SLASH) est proposée pour l'imagerie de gaz à bas champ. Des séries d'images à 2D dans des fantômes montrent qu'elle offre une résolution d'image et un RSB meilleurs que pour une séquence FLASH. Par ailleurs, des cartes de diffusion apparente dans des poumons fixés de petit animal ont été obtenues à partir d'images 2D et 3D. Les résultats sont compatibles avec ceux des mesures globales de diffusion par échos de spin dans ces mêmes poumons, et sont similaires aux résultats in vivo publiés. Ces poumons fixés sont donc un fantôme commode et pertinent pour des études méthodologiques. Les mesures de diffusion en bas champ, insensibles aux effets de susceptibilité, ont été faites sur une large gamme de temps de diffusion.

Mots-clés: résonance magnétique, bas champ, hélium-3 hyperpolarisé, IRM, diffusion gazeuse.

Abstract

In this work signal to noise ratio issues (SNR) of MRI at ultra-low field have been studied and potential applications using hyperpolarised ^{3}He gas have been explored. Two detection bandwidth broadening techniques have been considered: active feedback and coil coupling scheme. Active feedback was shown to be a more appropriate solution and has been implemented. Systematic diffusion-induced attenuation measurements in cylindrical ^{3}He gas samples have been performed over a very wide range of conditions using multiple spin-echo and gradient-echo schemes. Low gradient strengths and long gradient durations can be used at low fields, only limited by the inhomogeneity of the applied field and not by the susceptibility problem met at high fields. Our measurements provide a wide body of data for direct comparison with theoretical models and other data. A new imaging sequence (Slow Low Angle Shot, SLASH) is proposed for imaging at low fields. Series of 2D imaging experiments in phantoms proved that it provides a better image resolution and SNR than a FLASH sequence. Besides that, ADC maps in preserved lungs were created from 2D and 3D images. The obtained ADC histograms are consistent with the results of global CPMG diffusion measurements in the same preserved lungs and are similar to published in-vivo results, which makes this convenient inflatable porous system a relevant lung phantom for methodological studies. Since low-field ADC measurements in lungs are immune to susceptibility gradients, they can be performed over a wide range of diffusion times.

Keywords: magnetic resonance, low field, hyperpolarised helium-3, MRI, gas diffusion.

Contents

Introduction

Magnetic Resonance Imaging (MRI) is a non-invasive technique based on nuclear magnetic resonance (NMR) phenomena used to visualize structure of the objects. The first nuclear magnetic resonance image on hydrogen nuclei was published in 1973 [1]. Magnetic resonance imaging of lung airspaces using laser-polarised gases (^{3}He or ^{129}Xe) has been pioneered in 1994 [2], and studied since then by a growing number of groups. A large number of pre-clinical and clinical lung MRI studies were performed [3–6]. Detailed anatomical and functional images of the lung can be obtained with MRI of gases in a safe, non-invasive way. Lung MRI using HP gases also allows to study lung airways in a dynamic way. Our team at Laboratoire Kastler Brossel (LKB) has been involved into the HP MRI since the very beginning, taking advantage of its know-how in helium polarization and in NMR of gases. Collaborative work has been pursued with a team at Kremlin-Bicetre Hospital and through EU projects. Many lung MRI experiments were performed at high magnetic fields (1.5 T, 3T) on commercial proton MRI scanners adapted for ^{3}He. It has been shown [7], that the use of hyperpolarised gases allows for high and nearly field-independent signal-to-noise ratio (SNR) over a broad range of field values. High field experiments require massive and expensive superconductive magnets, which are hard to transport, have a fixed orientation of the static magnetic field. Also, application of high fields produces a variety of local gradients inside the tissue due to local magnetic susceptibilities. Such local field distortions decrease the reliability of the measured data. The advantages of using very low magnetic fields in hyperpolarised helium-3 MRI have been discussed before [7, 8]. Low fields lead to a very long signal lifetimes (up to many seconds) and negligible rf power deposition. Susceptibility effects does not play a significant role at low fields. The cost of a low-field instrument is also much lower: the magnetic field can be created by a set of resistive coils, and moreover, the space orientation of the MRI setup can be easily changed. The high SNR remains in a wide range of magnetic fields, until the thermal noise of the detection circuit becomes a dominating source of noise. Successful demonstrations of human lung MRI at such fields have been reported by a number of groups [7, 9, 10]. Research at very low field (order of mT) is currently pursued at LKB in Paris and at Harvard in Boston. One of the main differences between gas and liquid NMR, is the fast diffusion of the gas atoms or molecules. This is especially important for He gas, which has a high diffusion coefficient. Diffusive motion during MRI experiments leads to a fast signal attenuation in a presence of field gradients. This fact limits the range of usable imaging parameters and the image resolution. However, diffusion weighted MRI and apparent diffusion coefficient mapping are two of the potential applications of the HP gas MRI. Gas diffusion mapping in the lung airspaces is sensitive to their microstructure, it allows to discover structural destructions and marks of various destructive diseases [11, 12]. Gas diffusion in the lungs is restricted, diffusion effects can depart from the expectations for free diffusion. Assumption of a free diffusion is commonly used for data processing simply using a modified apparent diffusion coefficient (ADC). At low fields, a wide range of the diffusion conditions and regimes are accessible experimentally. This research work was performed since Jan. 15, 2007 and is a part of the task "”Low- and ultra low field Helium3 imaging”" of the work program of the Phelinet project (EU-funded FP6 Research and Training Network), shared by 3 partners: the LKB in Paris, the Kremlin-Bicetre Hospital team, and a team in Cracow. To explore the potential of ultra-low fields for imaging, a dedicated MRI magnet system, a compact 1:4-scaled model of a whole-body unit has been built previously in the LKB laboratory [13]. It has been designed to image 10-cm objects up to 6mT (200 kHz), and is suitable for small animal MRI. In this work signal to noise ratio issues for MRI at ultra-low field have been studied and potential applications using hyperpolarised ^{3}He gas have been explored. The work can be divided into a few key parts. It includes studies of broadband detection solutions, including computations and comparison between an active feedback scheme and coupled coils in detection circuits. Further enhancement and characterization of the properties of our imaging setup, such as signal-to-noise ratio, and detection bandwidth were made. Series of diffusion experiments with detailed analysis were made for various ^{3}He glass cells in order to explore the crossover diffusion regimes between free diffusion and restricted gas diffusion that could be met in lung MRI depending on imaging parameters and airway sizes. Studies using helium-3 phantom cells of the impact of diffusion on NMR signal attenuation in crossover diffusion regimes where no reliable theory exists for the interpretation of data obtained in clinical research are presented. 2D and 3D MR imaging experiments using this setup have been performed on preserved lung samples and lung phantoms with the demonstration of benefits of a new MRI sequence and methods of ^{3}He MRI at low fields. Maps of signal attenuation, related to the restricted gas diffusion in the lung microstructure, have been obtained.

Chapter 1

Increasing detection bandwidth in low field NMR and MRI

NMR and MRI rely on sensitive detection of precessing magnetization at Larmor frequency. Direct detection of the associated magnetic field that oscillates at Larmor frequency is efficiently performed using SQUID or atomic magnetometers at very low magnetic fields (e.g. $<$ mT) for various applications [14–20]. But the most widespread detection method relies on inductive detection using a coil. Usually the coil surrounds the sample and the e.m.f. is induced in it according to Faraday's law. The circuit with the detection coil is usually tuned with the capacitor to have a resonance at the NMR frequency. This provides several benefits, such as enhancement of the e.m.f., possibility for an impedance matching to cable amplifiers, frequency selection, etc. In this chapter two methods of detection bandwidth increase are considered. Series of computations are reported. Both methods are compared and discussed. An optimal solution for MRI at ultra low fields is selected to implement in our imaging apparatus. Its implementation and tests are described in Chapter 2.

1.1 Detection bandwidth issues in MRI

The use of a simple tank circuit in a detection provides a limited detection bandwidth. The detection bandwidth is a very important parameter for the imaging experiments because it limits both resolution and field of view of the image. An image resolution depends on the strength of the applied magnetic field gradients. Large field gradients lead to a wide distribution of Larmor frequencies over the sample and high resolution, but the detection system must operate correctly within this range of Larmor frequencies. Also, the final images need to be corrected for the frequency response of the detection circuit. This process of correction for high-Q coils with narrow bandwidth introduces an effective and disproportionate attenuation of a signal in the central part of the image in comparison to a signal and noise level near the edges of the image. Hence, it decreases the signal to noise ratio of the image. Small shift of the resonance frequency of the high-Q coil (maybe caused by loading, change in parasitic capacitance, etc.) can shift the frequency response of the circuit relatively so much that Larmor frequencies will not match with detection bandwidth frequencies, this can lead to significant change and error on the final image. For a high-field experiment it is possible to achieve desired values of the detection bandwidth using simple high-Q tank circuits, as soon as the bandwidth is supposed to be much smaller than the Larmor frequency. In low-field MRI the values of desired bandwidth can be the same order as the Larmor frequency. For example, in our case, for 2.7 mT magnetic field the desired bandwidth $\Delta f = 10$ kHz, but the Larmor frequency $f_L = 85$ kHz. It is obvious that such a relatively broad bandwidth is hard to obtain with high quality tank circuits. A traditional way to broaden the detection bandwidth of the tank circuit is to damp it with a resistor. Damping affects the signal at the output, but for some cases can be still suitable detection circuit in terms of bandwidth limits. In our experiments, the desired bandwidth $\Delta f = 10$ kHz sets the desired Q-factor value of the circuit to $Q = 8.5$. Having such low Q factor requires introduction of a high resistance to the circuit, but any additional resistance in the circuit introduces additional losses and corresponding Johnson noise into the signal. In many cases it is impossible to combine desired broad bandwidth with desired SNR and level of the output voltage.

1.2 A simple tank circuit

Before describing different broadening techniques we must characterize the simple tank circuit (Figure 1.1). A circuit with ideal capacitor, inductance and resistance (i.e. elements without parasitic inductance, capacitance and active resistance) will be considered in this section. It contains a resistor with resistance R, a capacitor with capacitance C and a detection coil with inductance L.

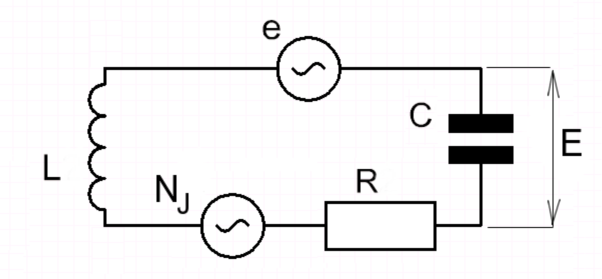

Figure 1.1: Equivalent scheme of a simple tank circuit: the voltage generator e stands for e.m.f. generated in the coil with the inductance L during NMR signal acquisition, and the voltage generator N_J for the Johnson noise voltage corresponded to the resistance R of the circuit. E is the voltage across the capacitor C.

The e.m.f. e appears in the coils due to the NMR signal

$$e = 4\pi\omega_0 MAn\eta \tag{1.1}$$

where A is the area of the detection coil, n - number of turns in the coil, η - filling factor of the coil by the sample, M- transverse magnetization, ω_0 - resonance frequency. As we can see, e.m.f. appeared in the detection coil depends on its geometry.

The total impedance Z of the tank circuit presented in Figure 1.1 at an angular frequency ω for a given resistance R, capacitance C and inductance L could be written as:

$$\bar{Z} = R + j\omega L - \frac{j}{\omega C} \tag{1.2}$$

The signal on the output (the voltage across the capacitor) is

$$E = \frac{e}{Z}\frac{1}{j\omega C} \tag{1.3}$$

and the ratio of output and input voltage $\frac{E}{e}$, which is a relative response of the circuit, is defined as

$$\frac{E}{e} = -\frac{j}{Z\omega C} \tag{1.4}$$

In Figure 1.2 the calculated relative response E/e and the corresponding bandwidth are plotted for circuits with different Q-factors for the case of $L = 1.25$ mH and resonance frequency $f_0 = 85$ kHz. Increasing the losses that are determined by the resistance R in the circuit allows to have higher bandwidth, but lower signal level on the output. With resistance in the circuit it is not possible to avoid the corresponding Johnson noise (thermal noise) N_J. For the resistance R at a given temperature T the spectral density of Johnson noise

$$N_J = \sqrt{4k_B T R} \tag{1.5}$$

To conveniently discuss the SNR for this tank circuit, we introduce the SNR factor f_{SNR} within the bandwidth Δf:

$$f_{\mathrm{SNR}} = \frac{E/e}{N_J} \tag{1.6}$$

An example of calculated SNR and relative response frequency dependences in the range of interest for the circuits with $L = 1.25$ mH and $f_0 = 85$ kHz are plotted in Figure 1.3 for different Q-factor values: 18, 90 and 180. They are normalized to the maximum values for the circuit with $Q = 180$. Figure 1.3 demonstrates that simple damping of the circuit allows to increase the detection bandwidth of the ideal circuit, but decreases SNR and output voltage at the same time for the fixed e.m.f. In this chapter all further results of SNR and relative response of the circuits calculations will be scaled for simplicity on this maximum values of a simple tank circuit with $Q = 180$, as it is the maximum Q factor achieved on practice for detection coils used in this work (Section 2.1.5).

1.3 A real tank circuit with preamplifier

The power dissipation and losses in the real circuit are determined by the existence of the resistance R. Consequently, circuit resistance determines the quality factor of the circuit. The sum of the parasitic losses in the coil R_L, in the capacitor R_C and in the connecting wires $R_{c.w.}$ also contribute to the total circuit resistance R_{total}.

$$R_{total} = R + R_L + R_C + R_{c.w.} \tag{1.7}$$

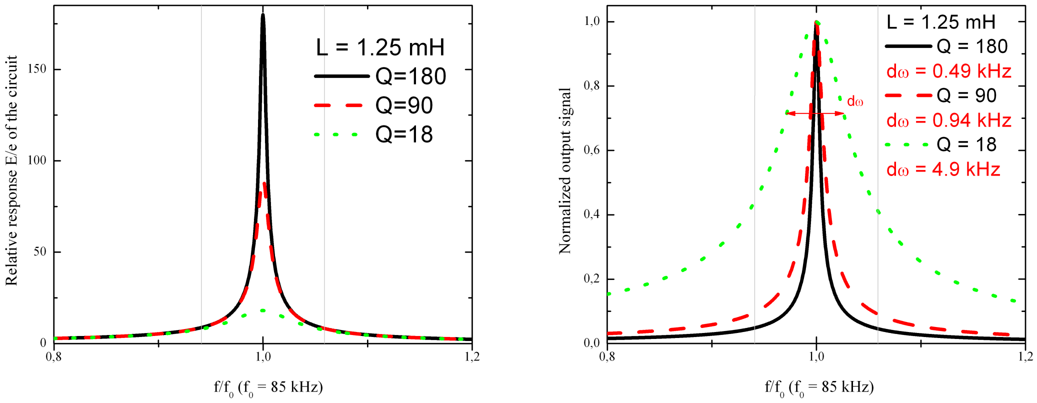

Figure 1.2: Resonance curve (left plot) and corresponding bandwidth (right plot) of a simple tank circuit calculated for a different Q-factors (solid lines - Q = 180, dashed - Q = 90, dotted - Q = 18). Inductance L = 1.25 mH and resonance frequency f_0 = 85 kHz are the same for all circuits. Detection bandwidth values are given on the graphs.

In general case, resistance R also depends on frequency and temperature due to skin and proximity effects. In our calculations these effects will not be considered and the total circuit resistance $R_{total} = R$. In order to build high-Q circuits it is important to take care of minimizing all the losses in the different components of the circuit.

However, the e.m.f. due to the NMR signal is not the only source of voltage e in the circuit. There are different sources of noise beyond Johnson noise (thermal noise) N_J, such as the preamplifier noise N_A and the picked up noise N_{pu} from parasitic external sources.

The noise of the preamplifier can be introduced into the circuit as equivalent voltage and current generators with noise densities V_n and I_n, respectively. Then the preamplifier noise density could be written as

$$N_A = \sqrt{V_n^2 + (I_n Z)^2} \tag{1.8}$$

If we drive an op-amp from a source resistance, the total noise over a bandwidth Δf will be a product of the amplifier's noise voltage, the voltage generated by the source resistance, and the voltage caused by the amplifier's I_n flowing through the source impedance.

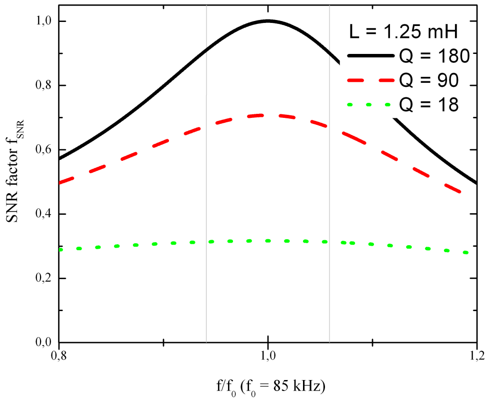

Figure 1.3: SNR factor of a simple tank circuit calculated for a different Q-factors (solid lines - Q = 180, dashed - Q = 90, dotted - Q = 18). Inductance L = 1.25 mH and resonance frequency $f_0 = 85$ kHz are the same for all circuits. SNR curves are normalized to the maximum SNR value of the $Q = 180$ circuit. Detection bandwidth values are given on the graphs.

$$N = \sqrt{N_J^2 + N_A^2}\sqrt{\Delta f} \tag{1.9}$$

$$N = \sqrt{4k_BTR + V_n^2 + (I_nZ)^2}\sqrt{\Delta f} \tag{1.10}$$

For very low source impedance, the latter term $(I_nZ)^2$ contributes insignificantly to the total noise and usually is negligible.

1.4 Coupled coils in the detection system

Our goal in this work is to consider various types of circuits that are suitable for the detection in MRI in terms of SNR, relative response, bandwidth, etc, particularly in the experimentally used frequency range. In this section we will perform necessary calculations and analysis with a general model of two circuits with inductive coupling (Figure 1.4). We will find out important equations for the universal system and then consider particular cases.

1.4.1 Theoretical description

The typical behavior of coupled coils circuits is well-described in [21].

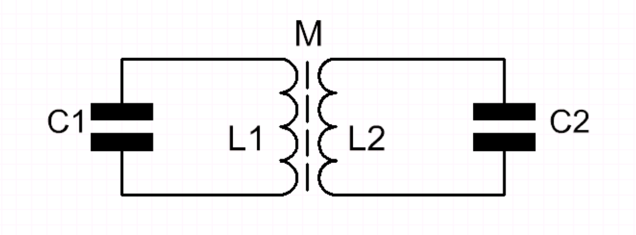

Figure 1.4: Scheme of inductively coupled circuits that consist of inductively coupled coils L_1 and L_2, and capacitances C_1 and C_2.

Two circuits ($i = 1; 2$) consist of ideal resistance R_i, capacitance C_i and inductance L_i each. Both circuits have inductive coupling with a mutual inductance M. In general case, both inductances L_1 and L_2 can be used for detection. If a coil is sensitive to the magnetization (i.e., produces some e.m.f.), it can be represented in the scheme by an equivalent ideal coil and a voltage generator in series. In the calculation of *e.m.f.* gain at the output and signal-to-noise ratio, the following universal scheme is used (Figure 1.5).

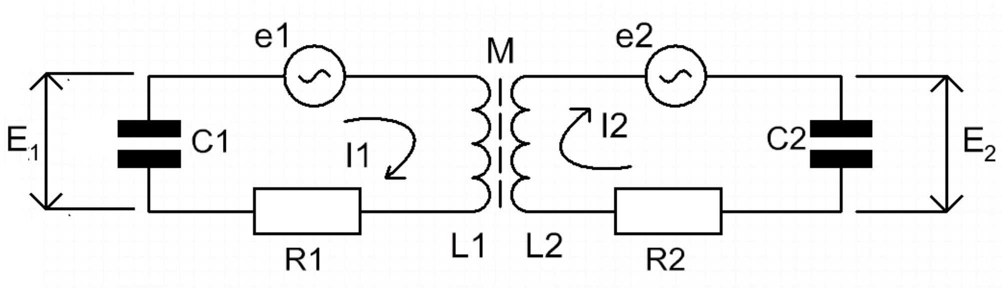

Figure 1.5: Universal scheme of two inductively coupled circuits with inductances L_1 and L_2, capacitances C_1 and C_2, resistances R_1 and R_2. The voltage generators e_1 and e_2 stand for e.m.f. generated in the coils during NMR signal acquisition. $E_{1,2}$ are the voltages across the capacitors $C_{1,2}$.

Here, L_1 - is the inductance of the coil that is coupled with the spins and introduces the e.m.f. e_1 in the primary circuit, L_2 - the one that also coupled with the spins and introduces the e.m.f. e_2 to the secondary circuit. Both coils are magnetically coupled with each other, with the coupling coefficient k. R_1 and R_2 - are resistances of primary and secondary circuits, C_1,C_2 are their capacitances. The outputs E_1 and E_2 of the circuits are defined as the voltage drops on capacitances C_1 and C_2. A relative response $|E/e|$ will be defined as ratio of the output voltage E and the e.m.f. e that is considered as an input signal. This value is proportional to the resonant response of the circuit. For simplicity, in general we will consider only $E_2/e_{1,2}$.

We can simplify the general scheme (1.5). If inductances of primary and secondary circuits are magnetically coupled with coupling coefficient $k = M/\sqrt{L_1 L_2}$, they can be introduced as an additional mutual inductance M in each circuit and then both circuits can be considered separately. According to this fact and Kirchhoff's voltage law, the following linear system of equations can be written:

$$\left(R_2 + j\omega L_2 - \frac{j}{\omega C_2}\right) I_2 - j\omega M I_1 = e_2 \tag{1.11}$$

$$-j\omega M I_2 + \left(R_1 + j\omega L_1 - \frac{j}{\omega C_1}\right) I_1 = e_1 \tag{1.12}$$

Introducing the impedances $Z_{1,2}$ of each circuit:

$$Z_{1,2} = R_{1,2} + j\omega L_{1,2} - \frac{j}{\omega C_{1,2}} \tag{1.13}$$

then determinant Δ of set of linear equations above is

$$\Delta = Z_1 Z_2 + \omega^2 M^2 \tag{1.14}$$

and the primary and secondary currents are:

$$I_1 = \frac{\begin{vmatrix} Z_2 & e_2 \\ -j\omega M & e_1 \end{vmatrix}}{\Delta} = \frac{Z_2 e_1 + j\omega M e_2}{\Delta} \tag{1.15}$$

$$I_2 = \frac{\begin{vmatrix} e_2 & -j\omega M \\ e_1 & Z_1 \end{vmatrix}}{\Delta} = \frac{Z_1 e_2 - j\omega M e_1}{\Delta} \tag{1.16}$$

The voltages E_1 and E_2 are then simplified as:

$$E_1 = \frac{j}{\omega C_1} I_1 \tag{1.17}$$

$$E_2 = \frac{j}{\omega C_2} I_2 \tag{1.18}$$

$$E_1 = j\frac{Z_2 e_1 + j\omega M e_2}{\omega C_1 \Delta} = F e_1 + G e_2 \tag{1.19}$$

$$E_2 = j\frac{Z_1 e_2 - j\omega M e_1}{\omega C_2 \Delta} = A e_1 + B e_2 \tag{1.20}$$

where

$$A = \frac{M}{\left(Z_1 Z_2 + \omega^2 M^2\right) C_2} \tag{1.21}$$

$$B = \frac{j Z_1}{\left(Z_1 Z_2 + \omega^2 M^2\right) \omega C_2} \tag{1.22}$$

$$|F| = |B| \frac{Z_2 C_2}{Z_1 C_1} \tag{1.23}$$

$$|G| = |A| \frac{C_2}{C_1} \tag{1.24}$$

For each circuit i,

$$\omega_i = \frac{1}{\sqrt{L_i C_i}} \tag{1.25}$$

where $\omega_{1,2}$ are resonant frequencies of primary and secondary circuits. Further in the calculations, also the central frequency $\omega_0 = \frac{\omega_1+\omega_2}{2}$ will be used. Or alternatively, $\omega_1 = \omega_0 \left(1 - d\right)$ and $\omega_2 = \omega_0 \left(1 + d\right)$. Parameters A,B,F and G define the corresponding relative responses for this circuit. For instance, parameter A actually is the relative response $|E_2/e_1|$ that appears in the secondary circuit (and is proportional to its resonant response if there is no signal picked up by the secondary coil), F is the relative response of e.m.f. $|E_1/e_1|$ that appears in the primary circuit. The quality factor Q_i of an ideal simple circuit is related to its impedance parameters and resonance frequency ω_i:

$$R_i = \frac{L_i \omega_i}{Q_i} \tag{1.26}$$

Then, an i-th circuit impedance Z_i at a frequency ω

$$Z_i = \frac{L_i \omega_i}{Q_i} + j\left(\omega L_i - \frac{1}{\omega C_i}\right) = \tag{1.27}$$

$$= \frac{L_i \omega_i}{Q_i} + j L_i \omega \left(1 - \left(\frac{\omega_i}{\omega}\right)^2\right) = \tag{1.28}$$

$$L_i \omega \left(\frac{\omega_0}{\omega}\frac{1 \mp d}{Q_i} + j\left(1 - \left(\frac{\omega_0}{\omega}\right)^2 \left(1 \mp d\right)^2\right)\right) \tag{1.29}$$

After a few combinations using equations 1.1 and 1.25,

$$A = \frac{M}{\left(Z_1Z_2 + \omega^2 M^2\right) C_2} = \frac{k\sqrt{L_1L_2}L_2\omega_2^2}{Z_1Z_2 + \omega^2 k^2 L_1 L_2} = \frac{k\sqrt{L_2/L_1}\left(\frac{\omega_0}{\omega}\right)^2 (1+d)^2}{H_1 + jH_2} \tag{1.30}$$

$$B = \frac{jZ_1}{\left(Z_1Z_2 + \omega^2 M^2\right)\omega C_2} = j\frac{L_1\omega\left(\frac{\omega_0}{\omega}\frac{1-d}{Q_1} + j\left(1 - \left(\frac{\omega_0}{\omega}\right)^2 (1-d)^2\right)\right) L_2\omega_2^2}{\omega\left(Z_1Z_2 + \omega^2 k^2 L_1 L_2\right)} \tag{1.31}$$

or

$$A = \frac{k\sqrt{L_2/L_1}\left(\frac{\omega_0}{\omega}\right)^2 (1+d)^2}{H_1 + jH_2} \tag{1.32}$$

$$B = j\frac{\left(\frac{\omega_0}{\omega}\frac{1-d}{Q_1} + j\left(1 - \left(\frac{\omega_0}{\omega}\right)^2 (1-d)^2\right)\right)\frac{\omega_0}{\omega}(1+d)^2}{H_1 + jH_2} \tag{1.33}$$

$$G = -\frac{k\sqrt{L_1/L_2}\left(\frac{\omega_0}{\omega}\right)^2 (1-d)^2}{H_1 + jH_2} \tag{1.34}$$

$$F = j\frac{\left(\frac{\omega_0}{\omega}\frac{1+d}{Q_1} + j\left(1 - \left(\frac{\omega_0}{\omega}\right)^2 (1+d)^2\right)\right)\frac{\omega_0}{\omega}(1+d)^2}{H_1 + jH_2} \tag{1.35}$$

where

$$H_1\left(\frac{\omega_0}{\omega}\right) = k^2 + \left(\frac{\omega_0}{\omega}\right)^2 \frac{(1-d)^2}{Q_1Q_2} - \left(1 - \left(\frac{\omega_0}{\omega}\right)^2 (1-d)^2\right)\left(1 - \left(\frac{\omega_0}{\omega}\right)^2 (1+d)^2\right) \tag{1.36}$$

$$H_2\left(\frac{\omega_0}{\omega}\right) = \frac{\omega_0}{\omega}\left(\left[1 - \left(\frac{\omega_0}{\omega}\right)^2 (1-d)^2\right]\frac{1+d}{Q_2} + \left[1 - \left(\frac{\omega_0}{\omega}\right)^2 (1+d)^2\right]\frac{1-d}{Q_1}\right) \tag{1.37}$$

So, for relative responses, we can have:

$$\left|\frac{E_2}{e_1}\right| = |A| = \frac{k\sqrt{L_2/L_1}\left(\frac{\omega_0}{\omega}\right)^2 (1+d)^2}{\sqrt{H_1^2 + H_2^2}} \tag{1.38}$$

$$\left|\frac{E_2}{e_2}\right| = |B| \tag{1.39}$$

$$\left|\frac{E_1}{e_1}\right| = |F| \tag{1.40}$$

$$\left|\frac{E_1}{e_2}\right| = |G| \tag{1.41}$$

The SNR factor similar to one for a tank circuit (1.6) can be used here for a proper characterization:

$$f_{\mathrm{SNR}} = \frac{E/e}{N} \tag{1.42}$$

where N is the noise spectral density on the output of the system and includes Johnson (thermal) noises of the circuits with spectral densities N_1 and N_2, picked up with coils parasitic signal with spectral density N_{pu}, noise of amplifier system with spectral density N_A:

$$N = \sqrt{(AN_1)^2 + (BN_2)^2 + N_A^2 + N_{pu}^2} \tag{1.43}$$

In the calculations, we will consider the situation where the picked up noise from external sources does not count $N_{pu} = 0$ and only the thermal noise of the both circuits N_1, N_2 and the noise of preamplifier N_A exist. The current noise term in equation 1.8 for the preamplifier noise will be neglected and the preamplifier in terms of noise will be considered as a voltage generator. For both circuits the Johnson noise spectral density is defined by the following equation:

$$N_{1,2} = \sqrt{4K_b R_{1,2} T} \tag{1.44}$$

1.4.1.1 Critical coupling

For coupled circuits with the same resonance frequency $\omega_0 = \omega_1 = \omega_2$, the voltage across the second capacitor E_2 has its maximum value when the coupling coefficient k is:

$$k_c = \frac{1}{\sqrt{Q_1 Q_2}}$$

This k_c value is called the critical coupling coefficient. If quality factors of both circuits are equal $Q_1 = Q_2$, then two peaks appear on the resonance curve for $k \leq k_c$ (see Section 1.4.4). With further increase of coupling between the coils, distance between this peaks increases. Distance between peaks on the resonance curve $\Delta\omega_{p-p}$ can be roughly found as [21]:

- for $k < k_c$:
$$\frac{\Delta\omega_{p-p}}{\omega_0} = 2\left(1 \pm \frac{k}{2}\right)$$
- for $k \gg k_c$:
$$\frac{\Delta\omega_{p-p}}{\omega_0} = 2\left(\frac{1}{\sqrt{1 \pm k}}\right)$$

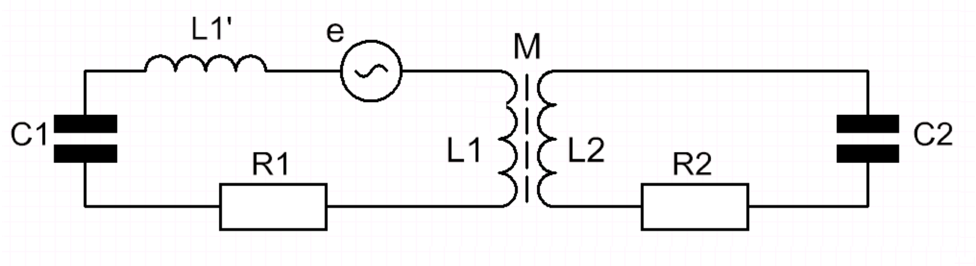

Figure 1.6: Typical scheme of weakly inductively coupled circuits

For detuned circuits with frequency difference δ and identical Q, the equivalent coupling coefficient is

$$k_{eq} = \sqrt{k^2 + \left(\frac{\delta}{f_0}\right)^2} \tag{1.45}$$

In other words, frequency detuning of the circuits leads to an increased coupling coefficient k for $Q_1 = Q_2$. For the case of distinct Q-factors some asymmetrical effects on resonant response appear besides of k increase.

1.4.1.2 Weak coupling mode (coupling of order of k_c)

In this mode of considered circuits, weak magnetic coupling between both coils with parameter k of order of k_c will be considered. It will be assumed that no e.m.f. appears in the second coil L_2 due to a MR signal, or, what is equivalent, in first circuit we have 2 coils L_1 and L', and L' is connected to spins, while L_1 is connected magnetically with L_2. The illustration of this scheme is shown in Figure 1.6.

Here, the relative reponse can be defined through parameter A from equation 1.38:

$$E/e = A \tag{1.46}$$

1.4.1.3 Strong coupling mode

The strong coupling mode concerns the case where the coils of both circuits are inductively coupled with an extremely high coupling factor $k \approx 1$, which leads to a separation of the peaks on the resonance curve to be of order of the resonance frequency ω_0. That also means that both coils are coupled to the sample and in both coils *e.m.f.*s appear due to

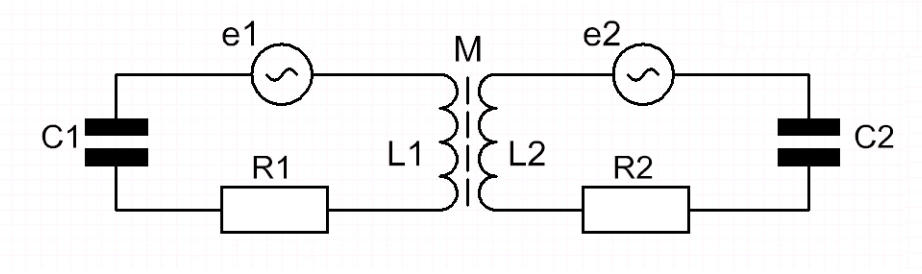

Figure 1.7: Typical scheme of strongly inductively coupled circuits

the coupling to nuclear spins. The equivalent scheme for the strong coupling regime is presented in Figure 1.7. The total voltage value E_2 is the sum of the relative response of the circuit on the corresponding e.m.f. values e_1 and e_2 multiplied by parameters A and B from equations 1.38 and 1.39:

$$E_2 = Ae_1 + Be_2. \tag{1.47}$$

The e.m.f. magnitudes of detected NMR signal in both coils e_1 and e_2 depend on the numbers of coils turns and their geometry. A proper comparison of the SNR for both circuits requires corrections for the number of turns (i.e. coil inductance) and their geometry. For simplicity in our calculations we assume both coils to be the same shape and inductance $L_1 = L_2$.

Values of f_{SNR} can be defined for both circuits as:

$$f^{A}_{\mathrm{SNR}} = A/N, f^{B}_{\mathrm{SNR}} = B/N \tag{1.48}$$

Where N is the total noise density on the output that can be found similarly to equation 1.43.

1.4.2 Approximate values of the detection bandwidth

The bandwidth and the value of output voltage are important properties of the detection circuit. Following equations can be useful for fast characterization of circuits. Approximate values of the SNR bandwidth for 3dB and 1dB SNR degradation can be calculated using following equations ([22]):

$$\Delta\omega_{3dB} \cong k\sqrt{Q_2/Q_1}\omega_1 \tag{1.49}$$

$$\Delta\omega_{1dB} \cong 0.46k\sqrt{Q_2/Q_1}\omega_1 \tag{1.50}$$

Taking into account equation 1.38, the output signal peak value E_2 across the second capacitor at frequency ω can be written as ([21]):

$$\frac{E_2}{e_1} = \frac{\omega_0^2}{\omega^2}\sqrt{\frac{L_2}{L_1}}\frac{\sqrt{Q_1 Q_2}}{\left[\sqrt{\frac{Q_1}{Q_2}} + \sqrt{\frac{Q_2}{Q_1}}\right]\left[1 - \frac{k_c^2}{4k^2}\left(\sqrt{\frac{Q_2}{Q_1}} - \sqrt{\frac{Q_1}{Q_2}}\right)^2\right]^{1/2}} \tag{1.51}$$

1.4.3 Comments on the resistance of the detection circuit

In various published works [21, 22] corresponding final equations for the relative response look simpler than obtained in this work 1.38. But it must be noticed that in all equations these authors use variable Q-factors with frequency dependent values $Q = \frac{\omega L}{R} = f(\omega)$. In this work Q factors are chosen to be as constants for simplicity and it explains the visible differences between equations in this work and mentioned literature sourcers. Hence, only the ratio Q_1/Q_2 between Q-factors of primary and secondary circuits and quality factor at resonance frequency $Q(\omega_0)$ have the values similar to ones used in this work. Frequency-dependent Q must be kept in mind during all calculations: $Q = Q_0\frac{\omega}{\omega_0}$. If

$$R_{1,2} = \frac{L_{1,2}\omega}{Q_{1,2}} \tag{1.52}$$

then

$$Z_{1,2} = R_{1,2} + j\omega L_{1,2} - \frac{j}{\omega C_{1,2}} = \tag{1.53}$$

$$\omega L_{1,2}\left(\frac{1}{Q_{1,2}} + j\left(1 - \left(\frac{\omega_{1,2}}{\omega}\right)^2\right)\right) = \omega L_{1,2}X_{1,2} \tag{1.54}$$

$$X_{1,2} = \frac{1}{Q_{1,2}} + j\left(1 - \left(\frac{\omega_{1,2}}{\omega}\right)^2\right) \tag{1.55}$$

$$A = k\sqrt{\frac{L_2}{L_1}}\left(\frac{\omega_2}{\omega}\right)^2\frac{1}{X_1X_2 + k^2} \tag{1.56}$$

$$B = \frac{X_1}{\omega L_2\left(X_1X_2 + k^2\right)} \tag{1.57}$$

However, simple calculations made for our case show that the difference in the definition of the resistances leads to 2% difference in total *e.m.f.* gain $|E_2/e_1|$ near resonance. This means that equations (1.56 and 1.57) also can be used for rough and fast computations.

1.4.4 Computed results for the weak coupling mode

According to this theoretical description, different bandwidth and SNR values could be achieved from an interplay between a set of circuit parameters: Q-factors Q_1, Q_2, inductances L_1, L_2, coupling coefficient k, difference $\delta = 2d$ between the resonance frequencies of the coupled circuits ω_1 and ω_2. The influence of these parameters on the typical behavior of $E_{1,2}/e$ relative responses, the bandwidth and the f_{SNR} values will now be considered. In this section, default circuits parameters were chosen close to the existing coils parameters used in our setup: quality factor $Q = 180$, inductance $L = 1.25$ mH, circuit tuned to a frequency $f_0 = 85$ kHz at room temperature $T = 300$ K and with an amplifier voltage noise density $N_A = 4\ nV/\sqrt{Hz}$.

1.4.4.1 Impact of coupling coefficient k on typical E_2/e and E_1/e behavior

At a very small coupling coefficient k, the influence of the existence of the secondary circuit on the primary one is also very small. The behavior of the primary circuit does not differ much from the single circuit behavior. When increasing the coupling towards order of k_c, the effective bandwidth of relative response curves A, B, F and G become broader. Two peaks with a small caving in appears on the relative response curve $F = E_1/e_1$, and the output voltage magnitude decreases. At the same time, the value of the current in the secondary circuit I_2 arises and the relative response curve $A = E_2/e_1$ becomes flatter and broader. The latter reaches the maximum value at a critical coupling coefficient k_c (Figure 1.8). With further increase of coupling, this curve also splits into two peaks. The distance between peaks of the relative response curves increases and values of the central part decrease when coupling coefficient k is increased further.

Unfortunately, an effective bandwidth of the relative response curve $F = E_1/e_1$ at $k > k_c$ has a deep trench in the center which makes output voltage E_1 useless for imaging experiments. However, the $A = E_2/e_1$ behavior shows us that an increase of coupling k leads to the flatness of the central part and an increase of bandwidth that is chosen as a full-width at $1/\sqrt{2}$ from resonance curve maximum. Two coupling modes can be selected for the further consideration as a possible solutions to increase the circuit's bandwidth. The first mode when $k \approx k_c$ and the bandwidth is broader than of a single tank circuit,

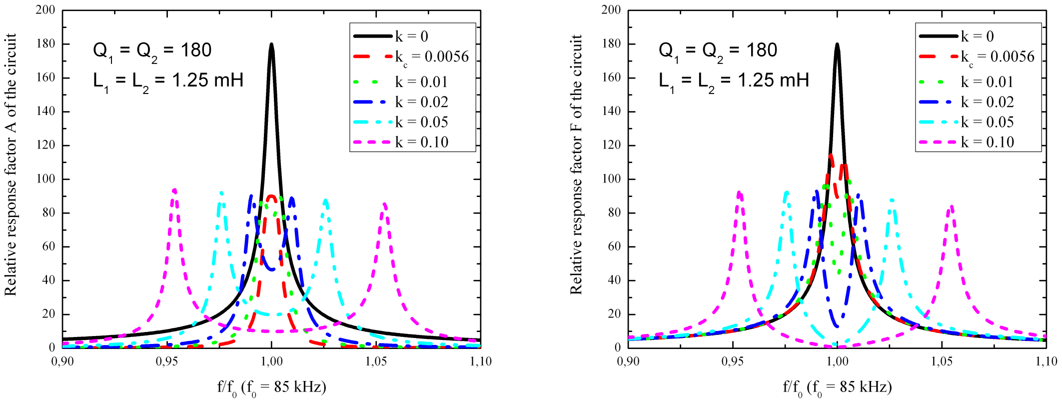

Figure 1.8: Calculated by eq.1.39 and 1.49 relative response factors A (left plot) and F (right plot) for different coupling coefficients k between the circuits with $Q = 180$ and $L = 1.25$ mH tuned to a frequency $f_0 = 85$ kHz, The case of $k = 0$ corresponds to a single tank circuit with $Q = 180$ and $L = 1.25$ mH, tuned to a frequency $f_0 = 85$ kHz.

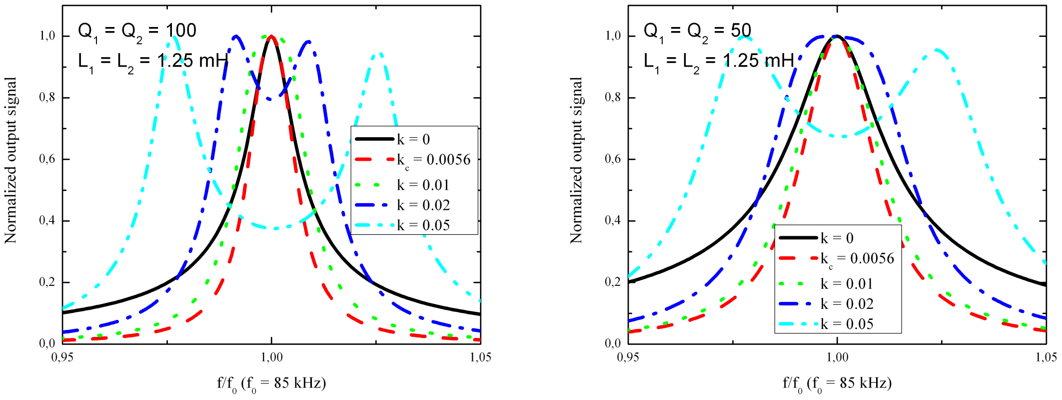

Figure 1.9: Calculated by eq.1.39 relative response parameters A for different coupling coefficients k between the circuits with $Q = 100$ (left plot) or $Q = 50$ (right plot) and $L = 1.25$ mH tuned to a frequency $f_0 = 85$ kHz. All curves are normalized to maximum values to make visible changes of the bandwidths. The case of $k = 0$ corresponds to a single tank circuits with of the same Q, L and tuned to a frequency $f_0 = 85$ kHz.

and the relative response of the circuit is high enough. In this case bandwidth is set as a full-width at $1/\sqrt{2}$ from resonance curve maximum. The second, or overcoupled, mode when resonance curve peaks are separated and easily distinguishable but the central part between them is flat in some frequency range and can be used in imaging. It must be noted that the relative response in this part of resonance curve has much lower values than at peaks. In this case bandwidth is set as a frequency range that allows for a frequency response curve variations of $1/\sqrt{2}$ from the response curve maximum value. Normalized relative response E_2/e curves are one of the main criteria for comparison various broadening solutions and find proper range of frequencies that can be used in imaging and they will be considered in many cases below.

Figures 1.9 displays the effect of quality factors on relative response. At almost two and four times lower Q factors, 50 and 100, corresponding relative response values, of course, are also two and four times lower. The peaks are smoother, the bandwidth increases when Q factor decreases. But the maximum f_{SNR} value is closer to the corresponding f_{SNR} value for the single circuit with the same lower value of Q. Low initial Q factors provide better bandwidth than circuits with high Q, but absolute f_{SNR} values for them are also lower.

Figure 1.10 illustrates the change of the f_{SNR} ratio with the value of coupling coefficient k. On this plots all f_{SNR} values are normalized to the f_{SNR} value of a single tank circuit with $Q = 180$. This figure shows that in overcoupled mode f_{SNR} definitely becomes uniform in the region of interest and its values are close to the maximum ones. It means that for imaging in case of weak coupling, a slightly overcoupled mode is preferable in terms of SNR.

1.4.4.2 Impact of frequency detuning δ on typical E_2/e and E_1/e behavior

The effect of detuning, as it was mentioned in the theoretical section (eq. 1.45), involves increasing the effective coupling coefficient. The influence of the detuning on the bandwidth and relative response curves is presented in Figure 1.11. The frequency dependence of the SNR becomes asymmetrical, its maximum value shifts to a higher frequency for E_2 and to a lower one for E_1. The impact on the primary circuit response is more dramatic: the second peak, that corresponds to the secondary circuit, becomes very small and the

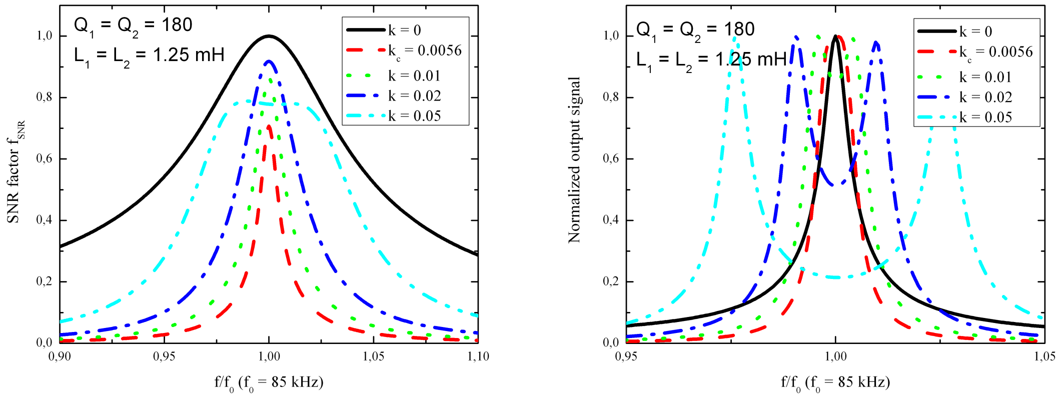

Figure 1.10: Calculated by eq.1.39 and 1.43 f_{SNR} (left plot) and relative response parameter A normalized to 1 (right plot) for different coupling coefficients k between the circuits with $Q = 180$ and $L = 1.25$ mH, tuned to a frequency $f_0 = 85$ kHz. f_{SNR} values are normalized to the maximum f_{SNR} value of the simple tank circuit with $Q = 180$ and $f_0 = 85$ kHz. The case of $k = 0$ corresponds to a single tank circuit with $Q = 180$ and $L = 1.25$ mH tuned to a frequency $f_0 = 85$ kHz.

final line shape tends to that of a single tank circuit.

1.4.4.3 Impact of Q-factor value Q on typical E_2/e and E_1/e behavior

Behavior of the output signal and the f_{SNR} when quality factors of both circuits are not equal have been calculated. Results are presented in Figures 1.13 and 1.14. The higher Q_1 we will use, the higher value of the maximum output voltage can be achieved. But f_{SNR} becomes smooth and broader (Figure 1.14) when Q_2/Q_1 relation increases. In all considered cases, the shape of the frequency response curve changes qualitatively only near the central frequency. To obtain a flatter frequency dependence of E_2/e, Q_1 should not exceed Q_2. Values of Q factors close to each other provide higher SNR values and are preferable.

1.4.4.4 Impact of L' inductance value on typical E_2/e and E_1/e behavior

It is clear that varying of relation between detection L_1' and coupling inductances L_1 of primary circuit is equivalent to changing of the coupling factor between two circuits k.

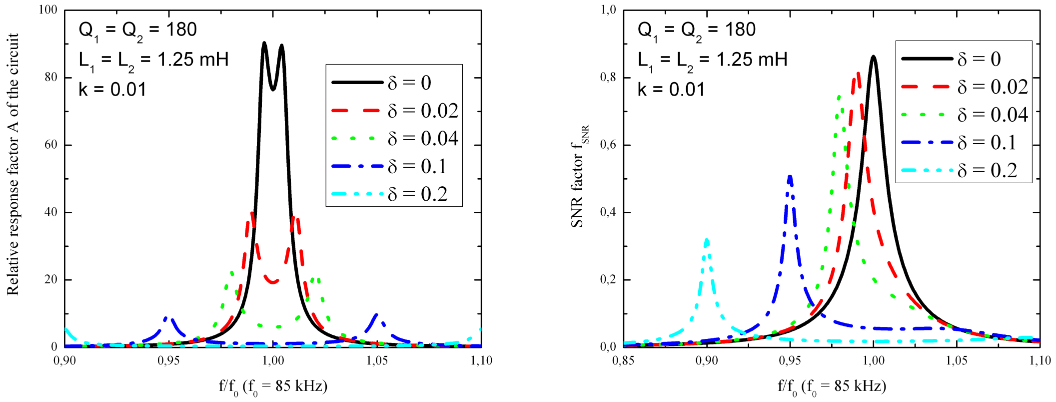

Figure 1.11: Calculated by eq.1.39 relative response parameter A for a coupling coefficient $k = 0.01$ between the circuits with $Q = 180$ and $L = 1.25$ mH tuned to a frequency near $f_0 = 85$ kHz with a different detuning between the circuits δ (left plot), and corresponding calculated $f_{\rm SNR}$ values (right plot). $f_{\rm SNR}$ values are normalized to the maximum $f_{\rm SNR}$ value of the simple tank circuit with $Q = 180$ and $f_0 = 85$ kHz

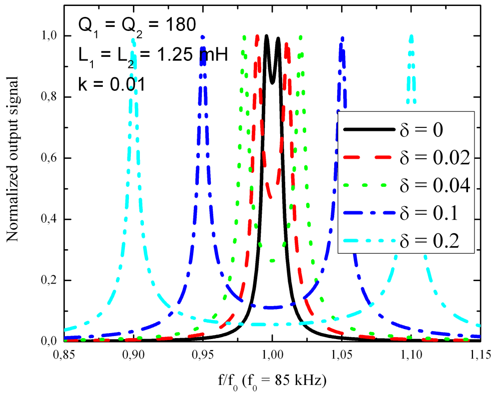

Figure 1.12: Calculated by eq.1.39 and normalized to 1 relative response parameter A for a coupling coefficient $k = 0.01$ between the circuits with $Q = 180$ and $L = 1.25$ mH tuned to a frequency near $f_0 = 85$ kHz with a different detuning between the circuits δ

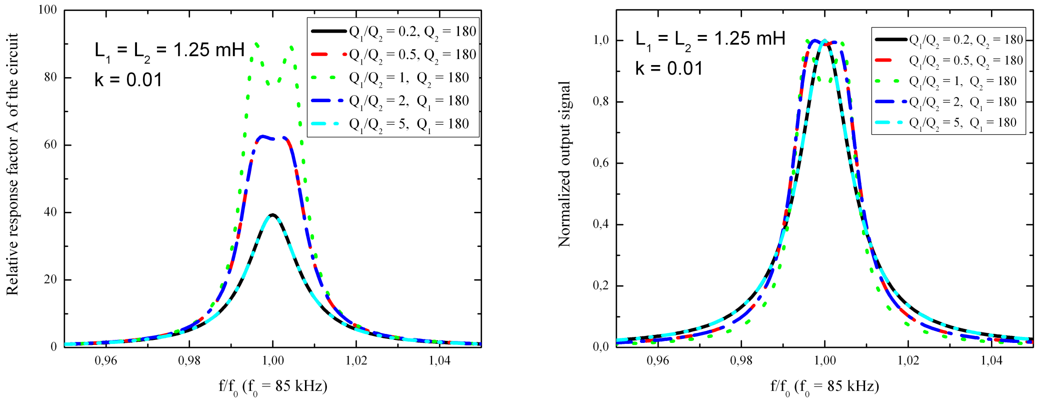

Figure 1.13: Calculated by eq.1.39 relative response parameter A (and normalized to 1 on the right plot) for a coupling coefficient $k = 0.01$ between the circuits with $L = 1.25$ mH tuned to a frequency $f_0 = 85$ kHz for a different Q_1/Q_2 ratios. Curves for the Q_1 and Q_2 ratios of 0.5 and 2 are similar (the same for ratios 0.2 and 5)

.

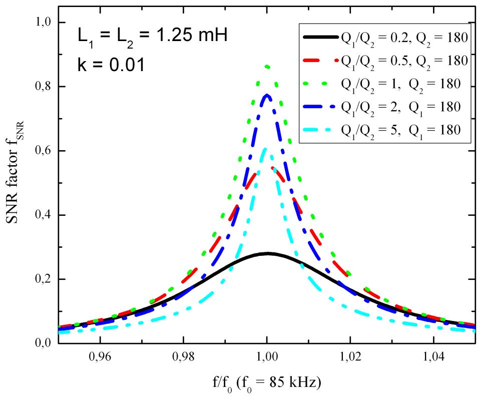

Figure 1.14: Calculated by eq.1.43 f_{SNR} values for a coupling coefficient $k = 0.01$ between the circuits with $L = 1.25$ mH tuned to a frequency $f_0 = 85$ kHz for different Q_1/Q_2 ratios. The maximum $Q = 180$ for all calculations. f_{SNR} values are normalized to the maximum f_{SNR} value of the simple tank circuit with $Q = 180$ and $f_0 = 85$ kHz

1.4.4.5 Impact of amplifier noise N_A on typical E_2/e and E_1/e behavior

A very important and interesting point is the impact of the amplifier noise on the total SNR. In some systems, the amplifier noise spectral density N_A can be of order of the Johnson noise spectral density N_J of the circuits or exceed it. Calculations of the Johnson noise values N_J predict the limit of the voltage noise spectral density of 35 $nV/\sqrt(Hz)$ for given circuit parameters. To show the effect of the high amplifier noise on the f_{SNR}, the latter was calculated for a few different values of amplifier noise spectral densities $N_A = 0, 1, 4, 40, 400$ $nV/\sqrt(Hz)$, and the coupling coefficient $k = 0.01$ slightly higher than the critical coupling coefficient for the given set of coils $k_c = 0.0056$. Results are presented in Figure 1.15. In the cases when the amplifier noise is low and does not exceed the Johnson noise of the circuit ($N_A < N_J$), the noise spectral density on the output $N/\sqrt{\Delta f} = \sqrt{N_A^2 + N_J^2}$ has mostly a thermal noise origin and corresponding flat frequency response of the f_{SNR} curve. But since N_A becomes comparable to, or exceeds, the Johnson noise density N_J, the f_{SNR} curve is affected by a noisy amplifier in the frequency domain. And values of the f_{SNR} decrease significantly (Figure 1.15). For the calculated set of circuit properties the use of a low-noise amplifiers with $N_A \approx 4$ $nV/\sqrt{Hz}$ will not significantly change the output signal within the chosen bandwidth. This fact led to an implementation of the low noise amplifier in our MRI system and is described in Chapter 2.

1.4.5 Computed results for the strong coupling mode

As it was demonstrated above, in overcoupled mode splitting between the peaks becomes rather huge. In the very strong coupling mode with $k \approx 0.8...1$, distance between the peaks becomes of the order of ω_0. In this kind of system, the total voltage on the capacitor in the secondary circuit is equal to $E_2 = Ae_1 + Be_2$ (eq. 1.47). For the weak coupling mode, the bandwidth and range of operational frequencies are considered to be between the peaks of the circuits resonance curve. The general idea of strong coupling is different. The range of operational frequencies is chosen to be within the one of the peaks of the resonance curves. In the calculations made here, the frequency dependence of parameters A and B, and corresponding f_{SNR} values were calculated.

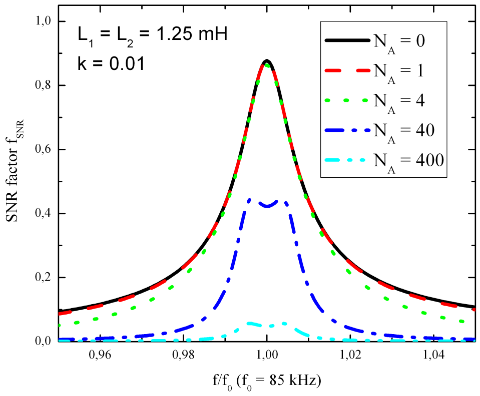

Figure 1.15: Calculated by eq.1.43 f_{SNR} values for a coupling coefficient $k = 0.01$ between the circuits with $Q = 180$ and $L = 1.25$ mH tuned to a frequency $f_0 = 85$ kHz for a different amplifier noise spectral density values N_A (given in $nV/\sqrt{Hz}$). f_{SNR} values are normalized to the maximum f_{SNR} value of a simple tank circuit with $Q = 180$ and $f_0 = 85$ kHz

An example of resonance curve of the parameters A and B is plotted in Figure 1.16 for the coupled coils tuned to the same frequency $f_0 = 85$ kHz with the same inductance $L = 1.25$ mH, quality factor $Q = 180$ and coupling factor $k = 0.9$. It should be noted that values of A and B are close to each other in the very wide range of frequencies, so the difference between plots is not visible on the image. A very high coupling between coils results in a huge distortion of the initial resonant frequencies of both circuits. Difference in the frequency values of the two peaks on the resonance curve is of order of frequency f_0. It is found that the right (higher frequency) peak of the resonance curve provides a quite broad bandwidth, as it can be seen in the figure. For the given parameters the effective Q factor with the resonance frequency in the center of the right peak equals to $Q = 58.5$, which is 3 times lower than the initial Q. This kind of increase of the effective bandwidth of the right peak is potentially interesting for imaging. The left peak (lower frequency) has an increased effective Q factor of 240 and decreased bandwidth which in not interesting and the lower frequency peaks will not be considered further.

Circuits response and f_{SNR} as a function of frequency were recalculated for the same circuits both detuned to a lower frequency in order to shift the center of the right peak at $f = 85$ kHz. Results of the calculations are illustrated in Figure 1.17. All f_{SNR} curves

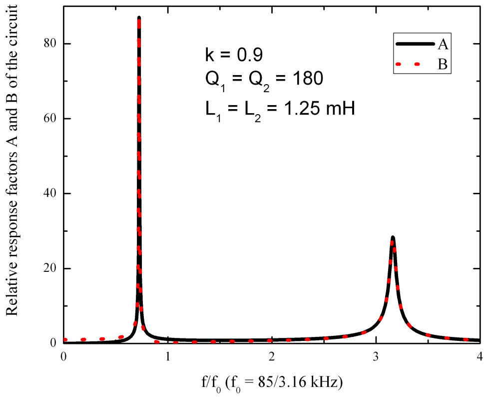

Figure 1.16: Calculated by eq.1.39 and 1.40 relative response parameters A and B for strong inductive coupling $k = 0.9$ between the circuits with $Q = 180$ and $L = 1.25$ mH tuned to a frequency $f_0 = 85$ kHz.

that are presented here, are plotted for parameter A as $f^A_{\text{SNR}} = A/N$. Since the factors A and B have almost the same dependencies in our regions of interest, $f^B_{\text{SNR}} = B/N$ is not plotted on the corresponding figures. The bandwidth of the tank circuits is increased three times. And the maximum value of f_{SNR} preserves the same as for the simple tank circuit with the same parameters but decreases by 30% towards to the edges of considered bandwidth. Such increase of the bandwidth by 3 times while SNR bandwidth narrows is not enough enhancement in terms of imaging at this frequency, but it has a high potential at higher frequencies. One way to achieve the desired effective Q factor of 10 in strong coupling mode is the decrease of the Q factors of both coupled circuits. But such changes will lead to a reduced SNR values, which is very unattractive.

1.4.5.1 Impact of coupling coefficient k on a A and B frequency behavior

Another possible solution to enhance the bandwidth (of the right, i.e. higher frequency peak) is to increase the coupling between the coils. Stronger coupling increases the peaks splitting and reduces the height of the right peak. The magnitude of the lower frequency peak increases at the same time. At $k \approx 1$ higher frequency peak vanishes. A clear example of the resonance curves shift for the coupled coils with coupling factor $k = 0.98$ is shown in Figure 1.18. Bandwidth of the higher frequency peak is increased

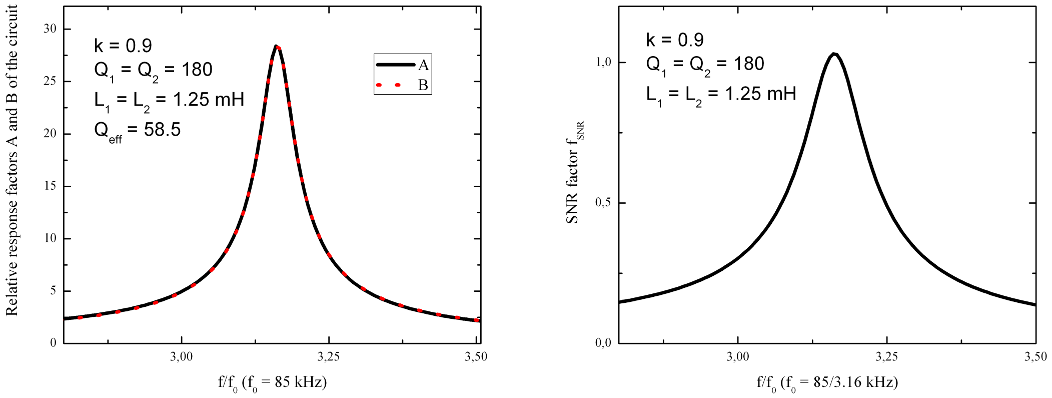

Figure 1.17: Calculated by eq.1.39-1.43 relative response parameters A and B (left plot) and f_{SNR} (right plot) for strong inductive coupling $k = 0.9$ between the circuits with $Q = 180$ and $L = 1.25$ mH tuned to have a center of the peak at frequency $f = 85$ kHz. The bandwidth is three times broader than of tank circuit (Figure 1.2), but the SNR bandwidth is narrower than one for tank circuit (Figure 1.3). Both curves are coincide in a wide frequency range. f_{SNR} values are normalized to the maximum f_{SNR} value of the simple tank circuit with $Q = 180$ and $f_0 = 85$ kHz

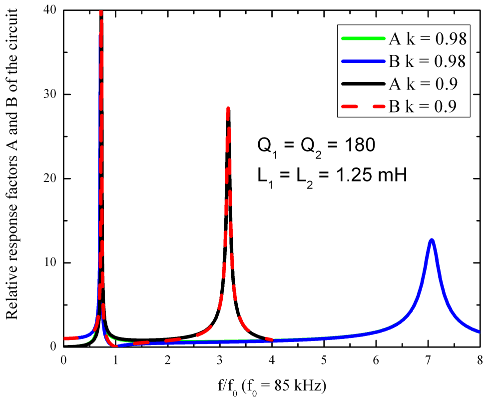

Figure 1.18: Calculated relative response parameters A and B for strong inductive coupling $k = 0.9$ and $k = 0.98$ between the circuits with $Q = 180$ and $L = 1.25$ mH tuned to a frequency $f_0 = 85$ kHz

and $Q_{eff} = 25.9$ decreased 7 times from the initial value. In order to compare these results with the simple tank circuit with $Q = 180$, recalculation of the f_{SNR} was made for a both coupled circuits tuned to a frequency, such that the center of the right peak was at $f = 85$ kHz. Results are presented in Figure 1.19. f_{SNR} values for stronger coupling are decreased while the peak bandwidth is now broader.

It is possible to make a following conclusion based on the calculations. The strong coupling between the detection coils allows to have detection systems with a broader bandwidth than the initial circuits under some limitations. However, computations show that amplitudes of the SNR changes with the desired bandwidth are not sufficient for use at the frequencies used in our experiments. Strong coupling can become a potential solution to increase narrow bandwidths at higher frequencies. It should be noted, that operation at low frequencies in practice is more difficult. tuning the circuits to a lower frequencies with preserved Q can be difficult, because it requires capacitors with higher capacitance or coils with higher inductances which introduce additional losses in the circuits.

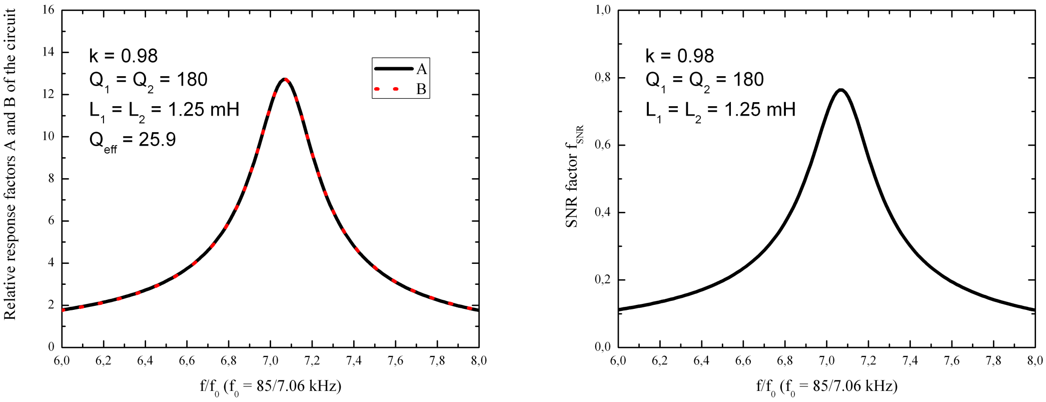

Figure 1.19: Calculated relative response parameters A and B (left plot) and $f_{\rm SNR}$ (right plot) for strong inductive coupling $k = 0.98$ between the circuits with $Q = 180$ and $L = 1.25$ mH tuned to have the peak centered at frequency $f = 85$ kHz. Both curves coincide in a wide frequency range. $f_{\rm SNR}$ values are normalized to the maximum $f_{\rm SNR}$ value of the simple tank circuit with $Q = 180$ and $f_0 = 85$ kHz

1.5 Using active feedback in the detection system

A number of successful implementations and demonstrations of an active feedback in NMR detection systems are known. They all present an active feedback as a solutions to damp the probe coil, reduce radiation damping effects and shorten the rign down noise duration. Hoult described in 1979 [23] an amplifier with capacitive negative feedback to the probe coil that allowed to decrease an effective Q factor of the tank circuit from 170 to 7. Experiments were performed at 5 MHz frequency and significant reduction of the ring down time is demonstrated. Significant reduction of the radiation damping effect at high NMR frequency (400 MHz) is reported in [24]. The authors used the signal and a special electronic network to feed back the signal with an opposite phase to the probe via a directional coupler and preserved the SNR of the system. This scheme looks hard to implement at low NMR frequencies. Demonstration of the radiation damping suppression without significant SNR degradation by a feedback circuit with RF feedback loop also was described by Broekart and Jeener [25]. The latter case of the feedback schemes is chosen as the most appropriate for the case of low NMR frequencies of 85 kHz order and is theoretically considered below in this section. Decrease of an effective quality

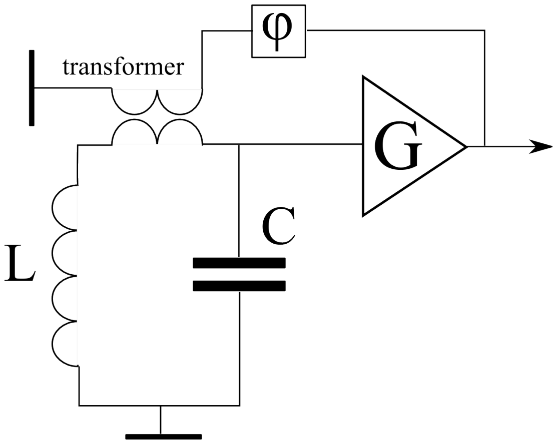

Figure 1.20: Scheme of a detection circuit with an active feedback

factor of tank circuit described by above authors makes it a potentially useful solution to increase the detection bandwidth for the MRI needs. Similar feedback scheme was created and successfully used by Emmanuel Baudin (another PhD student of LKB) in low field 75 kHz NMR experiments on hyperpolarized liquid ^3He samples to suppress the radiation damping effect [26].

1.5.1 Theoretical approach

In this section a more complex circuit will be considered. The schematics of an active feedback implementation in the detection circuits is illustrated in Figure 1.20. A signal from the simple resonance circuit goes to an amplifier with gain $\bar{G}$. The output of the amplifier is connected to the simple circuit via an inductive transformer with a coupling efficiency (i.e., how much of feedback signal is in the internal circuit) $\bar{c}$. The coupling efficiency $\bar{c}$ here is complex, that means it is possible to change the phase ϕ of the signal in the feedback line.

The total impedance Z of the tank circuit presented in Figure 1.20 at an angular frequency ω for a given resistance R, capacitance C and inductance L is given in eq. 1.2.

Several sources contribute to the signal on the output in addition to the e.m.f. e that arises during NMR signal detection in the detection coils. There is an additional voltage $e_{FB} = \bar{c}\bar{G}\left(S + N_A\right)$ arising from the feedback. Also it is not possible to avoid the Johnson (or thermal) noise of the circuit. In further calculations external parasitic noise sources are neglected ($N_{PU} = 0$). The current noise I_n source of the preamplifier will be neglected and preamplifier noise $N_A = V_n$ is retained as it is done for the coupled coils (see Section 1.4.1).

$$E = e + N_J + \bar{c}\bar{G}\left(N_A + S\right) \tag{1.58}$$

If S is the voltage across the capacitor C, and V is the output voltage of the amplifier with the gain G and the voltage noise density N_A, then the current I in the internal circuit

$$I = \frac{E}{Z} \tag{1.59}$$

$$S = -\frac{I}{jC\omega} \tag{1.60}$$

$$S\left(-j\omega CZ\right) = e + N_J + \bar{c}\bar{G}\left(N_A + S\right) \tag{1.61}$$

$$S = \frac{e + N_J + \bar{c}\bar{G}N_A}{-j\omega CZ - \bar{c}\bar{G}} \tag{1.62}$$

$$V = \bar{G}\left|S + N_A\right| \tag{1.63}$$

$$V = \bar{G}\left|\frac{e + N_J + \bar{c}\bar{G}N_A}{-j\omega CZ - \bar{c}\bar{G}} + N_A\right| \tag{1.64}$$

$$\tag{1.65}$$

It is better to use the relative frequency variable $\tilde{\omega}$ for a further analysis of the output voltage frequency dependence.

$$\omega_0 \equiv \frac{1}{\sqrt{LC}} \tag{1.66}$$

$$\tilde{\omega} \equiv \frac{\omega}{\omega_0} \tag{1.67}$$

Then, the output voltage is given by

$$V = G\frac{e + N_J + N_A\left(1 + \bar{c}\bar{G}\right)}{\tilde{\omega}^2 - 1 - \bar{c}\bar{G} - \frac{j\tilde{\omega}}{Q}} \tag{1.68}$$

or

$$V = G\left(\frac{e + N_J}{\tilde{\omega}^2 - 1 - \bar{c}\bar{G} - \frac{j\tilde{\omega}}{Q}} + N_A\frac{\tilde{\omega}^2 - 1 - \frac{j\tilde{\omega}}{Q}}{\tilde{\omega}^2 - 1 - \bar{c}\bar{G} - \frac{j\tilde{\omega}}{Q}}\right) \tag{1.69}$$

The above equation shows a very important feature: the SNR is independent on the feedback coupling efficiency factor $\bar{c}$.

The output voltage V for an ideal noiseless systems is:

$$V = G\left(\frac{e}{\tilde{\omega}^2 - 1 - \bar{c}\bar{G} - \frac{j\tilde{\omega}}{Q}}\right) \tag{1.70}$$

The combination $\bar{c}\bar{G}$ can be written as a combination of a real and an imaginary parts.

$$\bar{c}\bar{G} = X + j\tilde{\omega}Y \tag{1.71}$$

This will lead to a resonance frequency shift

$$\acute{\omega}_0 = \omega_0\sqrt{1 + X} \tag{1.72}$$

And the output voltage V will be written as

$$\acute{\tilde{\omega}} = \frac{\omega}{\acute{\omega}_0} \tag{1.73}$$

$$V = G\left(\frac{e}{(1 + X)\left[\acute{\tilde{\omega}}^2 - 1 - \frac{j\acute{\tilde{\omega}}\left(\frac{1}{Q} + Y\right)}{\sqrt{1+X}}\right]}\right) \tag{1.74}$$

Now a new effective Q-factor of the circuit $\acute{Q}$ could be found as

$$\acute{Q} = \frac{Q\sqrt{1 + X}}{1 + QY} \tag{1.75}$$

If the feedback does not contain any real part, $X = 0$ then

$$\acute{Q} = \frac{Q}{1 + QY} \tag{1.76}$$

These equations show that under some conditions active feedback damps the circuit and allows to increase its bandwidth without affecting of SNR values. The real part of $\bar{c}\bar{G}$ shifts the resonance frequency of the circuit while both real and imaginary parts change the bandwidth of the circuit.

1.5.2 Noise in active feedback systems

As can be seen from equation 1.69, the output voltage terms that correspond to the Johnson and the amplifier noise spectral densities N_J and N_A have different frequency dependencies when active feedback is applied to the detection circuit. The Johnson noise density $V(N_J)$ term of the output voltage V, as well as the *e.m.f.* induced during NMR experiments, is proportional to

$$V(N_J)(\omega) \propto \frac{1}{\tilde{\omega}^2 - 1 - \bar{c}\bar{G} - \frac{j\tilde{\omega}}{Q}} \tag{1.77}$$

While the preamplifier noise density $V(N_A)$ term is proportional to

$$V(N_A)(\omega) \propto \frac{\tilde{\omega}^2 - 1 - \frac{j\tilde{\omega}}{Q}}{\tilde{\omega}^2 - 1 - \bar{c}\bar{G} - \frac{j\tilde{\omega}}{Q}} \tag{1.78}$$

An example of different output behaviors of N_J and N_A is shown in Figure 1.21. The total noise spectral density $N/\sqrt{\Delta f}$ on the output can be found as the root of sum of squares of output voltage terms corresponding to N_J and N_A. It is obvious that the total spectral noise density on the output $N/\sqrt{\Delta f}$ behavior in the frequency domain changes dramatically with the value of the ratio N_A/N_J. These changes of the total noise will lead to changes of a frequency behavior of the SNR on the output.

If the preamplifier noise is a property of the preamplifier schematics and model, the Johnson noise can be changed in different ways: by changing of the coil geometry, of material of the coil wires, of resistance of the circuit, by replacing the capacitors with different losses. Some examples of such changes used in our experiments are illustrated in Section 2.1.5.

1.5.3 Calculations of the signal to noise ratio and the bandwidth

Computations of the relative response and the SNR are made for a circuit with the original $Q = 180$ and the coil inductance $L = 1.25$ mH. Figure 1.22 shows results of the mentioned computations. As it can be seen, an application of an active feedback results in a significant change of the frequency bandwidth. Thus, the one exceeds the bandwidth for a resistively damped tank circuit of $Q = 18$. Such broad frequency response of the

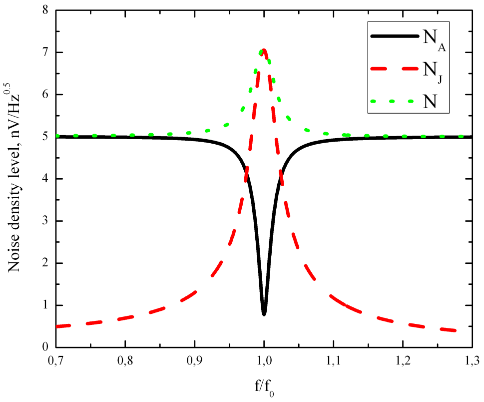

Figure 1.21: Different frequency behaviors of output terms corresponding to the noise spectral densities of different origins. Johnson noise term is calculated for the circuit with $Q = 180$ and $L = 1.25$ mH with an applied feedback. Spectral voltage noise density of the preamplifier $N_A = 5\ nV/\sqrt{Hz}$.

circuit with an active feedback makes it preferable for low-field MRI experiments. One of the most important advantages of using an active feedback scheme is the preservation of the high SNR level corresponding of the tank circuit. Figure 1.23 shows calculations of the SNR in the case of a low-noise preamplifier with the spectral noise density $N_A = 4\ nV/\sqrt{Hz}$.

In the particular case of the considered circuits, the preamplifier noise spectral density N_A and the Johnson noise density N_J are of the same level of magnitude. In order to generalize our results, different levels of the amplifier noise are considered. Three situations are compared for the same circuit with no changes of the Johnson noise density N_J in it: $N_A = 4\ nV/\sqrt{Hz}$, $N_A = 0.4\ nV/\sqrt{Hz}$ and $N_A = 40\ nV/\sqrt{Hz}$. Changes of the SNR frequency dependence for the different levels of N_A are calculated and results are shown in Figure 1.24. It should be noticed that lower N_A values allows for much more homogeneous SNR in a wide frequency range. As can be seen from the Figure 1.24, the amplifier noise density N_A, that is relatively higher than the Johnson noise density N_J of the circuit, leads to the narrow SNR bandwidth. The higher the amplifier noise, the narrower range of frequencies with the suitable SNR values is. The amplifier noise values lower than the circuit's Johnson noise correspond to small SNR changes within a wide

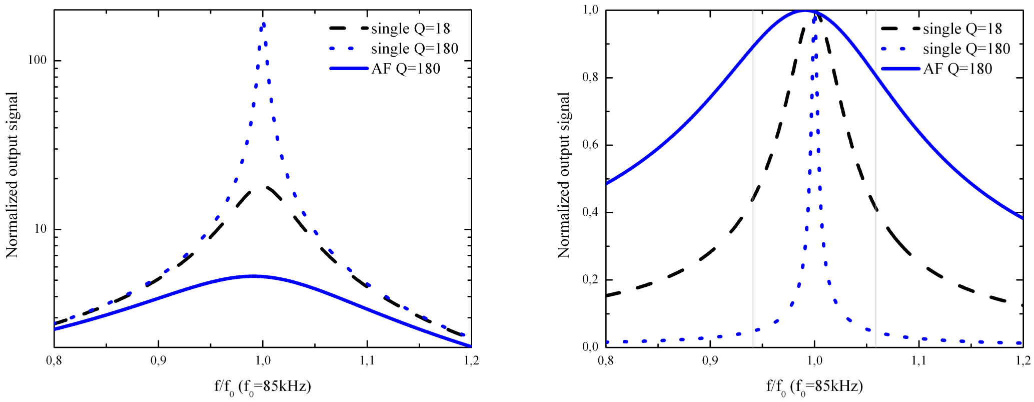

Figure 1.22: Frequency response (left plot) and bandwidth (relative response normalized to one, right plot) of the detection system with an active feedback. Calculated for the circuit with $Q = 180$ and $L = 1.25$ mH tuned to have a center of the peak at frequency $f = 85$ kHz.

range of frequencies. In other words, for certain situations and the amplifier noise values, an active feedback is not an efficient solution and ratio of the N_J and N_A sets the limit on the active feedback application.

1.6 Comparison of an active feedback scheme and coupled coils detection systems

Two methods for increasing the bandwidth have been considered in Sections 1.4 and 1.5. We discuss the difference and advantages in this section. The main criteria that can be used for discussion and comparison of both methods are the frequency relative response of the circuits and the SNR. Frequency response of the circuit must be reasonably flat so that frequency response corrections on image can be accurately made. This flat region sets the imaging bandwidth. In this work, bandwidths allowing for circuit response changes up to $\sqrt{2}$ were considered. Relative changes of the SNR within the set bandwidth is an another important criterion for comparison of broadening solutions.

Both, the SNR and the relative response calculations are shown in Figure 1.25 for the particular case of the amplifier noise spectral density $N_A = 4\ nV/\sqrt{Hz}$ and the

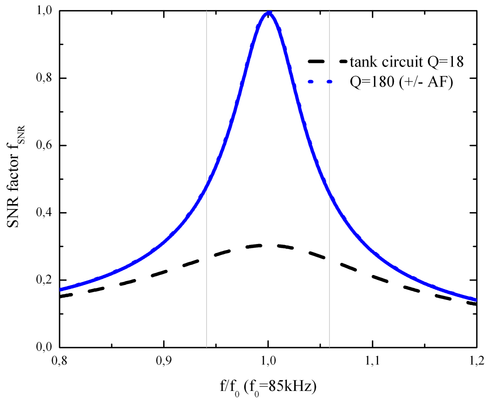

Figure 1.23: Calculated SNR of the detection system with an active feedback. Calculated for the circuit with $Q = 180$ and $L = 1.25$ mH tuned to have a center of the peak at frequency $f = 85$ kHz.

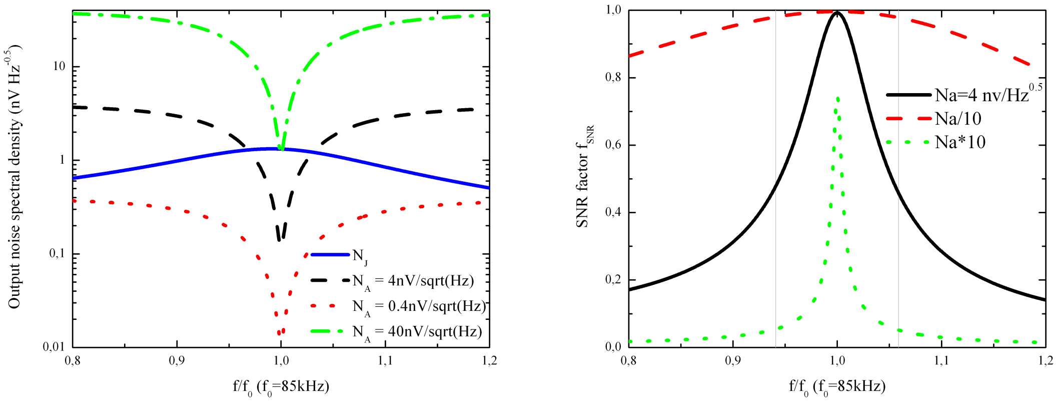

Figure 1.24: Interplay of output noise terms of different origins (left plot). Influence of the preamplifier noise spectral density values on the SNR factor bandwidth for the particular circuit (right plot). Calculated for the circuit with $Q = 180$ and $L = 1.25$ mH tuned to have a center of the peak at frequency $f = 85$ kHz.

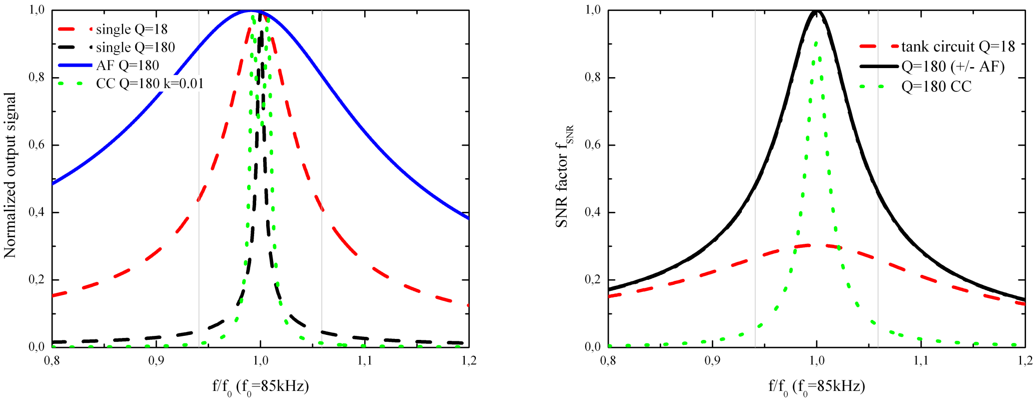

Figure 1.25: Comparison of an active feedback and coupled coils (Figures 1.8,1.10, k=0.01) detection systems: bandwidth (left plot) and SNR (right plot) calculated for the circuit with $Q = 180$ and $L = 1.25$ mH tuned to have a center of the peak at frequency $f = 85$ kHz.

circuits with $Q = 180$ and the inductance $L = 1.25$ mH. For the coupled coils, a coupling factor of $k = 0.015$ was used in the calculations. Also, similar calculations for the simple tank circuits with $Q = 180$ and $Q = 180$ are presented as a reference systems. Coupled coils provide a broadening of the detection bandwidth within the order of the FWHM value. This is not suitable for the low frequency NMR and MRI experiments using high Q circuits: the SNR has a suitable values in a narrow range of frequencies, as well as the frequency response of the circuits. Only limited bandwidth broadening is available at low fields. But, it can become to a solution for the high-frequency experiments where $\Delta f \ll f_L$ [22]. For coupled coils system various possibilities were explored in literature. Inductive coupling between coils provides a certain improvement upon a single high-Q tank circuit. A demonstration of the coupled coils system in imaging at hight field 9.4 T can be found in [27].

A proper active feedback scheme applied to the tank circuits with high Q values can be used in a wide range of f_0 and seems like an optimal solution for the low field MRI experiments. It can provide the desired bandwidth with suitable SNR values within a certain range of amplifier noise level. For $Q \leq 15$ at low fields, the active feedback scheme is clearly better in terms of bandwidth and SNR. A successful demonstration of an active feedback scheme in our experiments and illustrations of its advantages is given in the setup characterization Section 2.2.6.

1.7 Summary

Two detection bandwidth broadening techniques have been considered. An active feedback scheme was chosen as an appropriate solution to solve the bandwidth problems in our low field setup. Implementation of an active feedback scheme and its properties will be discussed in the Chapter 2. Using coupled coils remain as a possible suitable solution at higher magnetic fields. Combination of an active feedback and coupled coils in the detection system is a subject of the future studies.

Chapter 2

Experimental Setup

This chapter consists of two parts. In the first one the used experimental setup is described. Basic properties of the magnetic system, gradients, detection and control units are given. Important details on the experimental samples and the gas management are given. The second part is focused on the characterization of the setup units which are important during setup operation and further interpretation of experimental results. Information on the magnetic field inhomogeneity, rf and gradient pulse units functionality, tuning of the detection system is placed here.

2.1 Description

The B_0, B_1, and gradient coils have been designed, constructed, and coarsely characterised before the beginning of this PhD work [13]. This set of coils was made as a 1:4 reduced scale test prototype system of a whole-body system for humans, and has 15 cm bore. Its description and main characteristics are provided here for convenience.

2.1.1 B_0 coils

The constant B_0 field is produced by a resistive electromagnet. Direction of the B_0 field will coincide with the Z axis for simplicity. It consists of 5 coaxial ring copper wire coils wound on round polyvinyl chloride (PVC) frames with 29 cm outer diameter. The total length of the five coils set is 26 cm. The set of coils is shown on the left hand side part of Figure 2.1, with detailed dimensions given in the caption. It was designed to have a uniform field over a 10 cm diameter sphere, with a computed standard deviation of 15 ppm over this volume. Computations were made by a downhill simplex method using an in-house software. The B_0 field produced by the coils in the center is 2.6 mT/A, and can reach 5 mT with 7 W/mT^2 of power dissipation. The magnet is driven by a standard laboratory power supply. Current instability of this power supply is 1 mA for changes in ±10% of the 220 V and is 5 mA for 10% change in load according to manufacturer's specifications. A possibility of air cooling of the copper wires is included through the coil frames to limit the temperature increase at high current values (higher than 1.2 A); it is not needed below 3 mT.

2.1.2 B_1 coils

NMR is performed using crossed coils. The tipping rf field is generated by a pair of coils producing a B_1 field along the Y axis (horizontal). The orientation of the coils is shown in Figure 2.1. They are an exact reduced-scale (1:4) copy of the whole-body B_1 coils described in ref. [7]. They are wound with 0.4 mm diameter enamelled copper wire on PMMA (poly(methyl methacrylate)) frames. The coils are connected in series, and tuned to resonance by a low-loss capacitor connected in series to reduce their impedance and match it to the output impedance of the in-house RF amplifier (based on a L165 power operational amplifier, that has a slew rate of 8V/μs and a maximum current of 3A on a 4Ω load).

2.1.3 Gradient coils

The gradient coil system consists of three sets of coils that can create linear gradients in three orthogonal directions. A schematic drawing of the gradient coils is shown in Figure 2.2. The transverse gradients are produced by two sets of 8 planar coils for each direction, wound on PMMA frames. The dimensions and positions of the coils were designed by in-house software to produce linear X and Y gradients of 1.1 mT/m/A with a computed inhomogeneity of 2.5% s.d. within a 10 cm diameter sphere. The impedance of each coil set is R=8 Ω, L=1.2 mH. The gradient field along the Z axis is produced by 4 coaxial ring copper wire coils wound on round PMMA frames (see Figure 2.1). The set creates a linear Z gradient of 3.2 mT/m/A with a computed inhomogeneity of 0.3% s.d. within the range of interest; the coil impedance is R=7.8 Ω, L=1.4 mH, close to that of the X and Y gradient coils.

2.1.4 Gradient control

Standard gradient amplifiers (based on a switched technology) are too noisy at our NMR frequency to be used in the gradient lines. Instead, gradient coils are driven by linear KEPCO bipolar power supplies BOP 36-6M and BOP 50-8M[1] commanded by a home-made gradient controller. The initial work on the gradient controller was made by Ileana Jelescu during her 3-month internship. The final design is displayed in Figure 2.3. Filters are used reduce rf interference entering the Faraday cage (see Sec. 2.1.12).

2.1.5 Detection coils

The detection coils consist of a pair of rectangular coils. Detection coils are placed perpendicular to the B_1 field produced by B_1 coils as it shown in Figure 2.2. One of the important problems in detection coil design is a search for a low loss solution. In this work coils made from Litz wire were used and tested along with the single copper wire coils (A). A Litz wire is a multicore wire and is supposed to have less resistance that a single wire. Copper Litz wire with cotton isolation was used to build two detection coil pairs (B and C). Because acquired MR signal depends on a coil filling factor, a smaller pair of coils (B) was built in order to increase the SNR in experiments on smaller samples. Thereby three different detection coils pairs were used in our experiments. All coils consisted of pair of rectangular coils wound on parallel plastic frames with a certain distance between them. Their geometrical properties and important characteristics are presented in Tables 2.1 and 2.2. Photographs of the disassembled detection coils A and C are shown in Figure 2.4. Simple measurements of coil pair resistance approve that Litz wire coils have smaller values of resistance R than a single wire coils (A), i.e., allow for lower losses. Detection coil sensitivity was also computed for a given geometry and is presented in Table 2.2.

---

[1] www.kepcopower.com/bop.htm

Table 2.1: Detection coils geometry and basic properties

Coils	**Wire type**	**Length x Width, mm**	**Distance, mm**	**wire ⊘, mm**	**# of turns**
A	single copper	87.5 x 102.5	73	0.4	47
B	Litz copper	40 x 150	46	0.75 ± 0.08	36
C	Litz copper	77.5 x 102.5	65	0.75 ± 0.08	72

Table 2.2: Detection coils parameters

Coils	**Inductance L, μH**	**Resistance, Ω**	**Sensitivity, G/A**
A	588	5.42	6.07
B	599	1.62	6.61
C	929	2.71	10.52

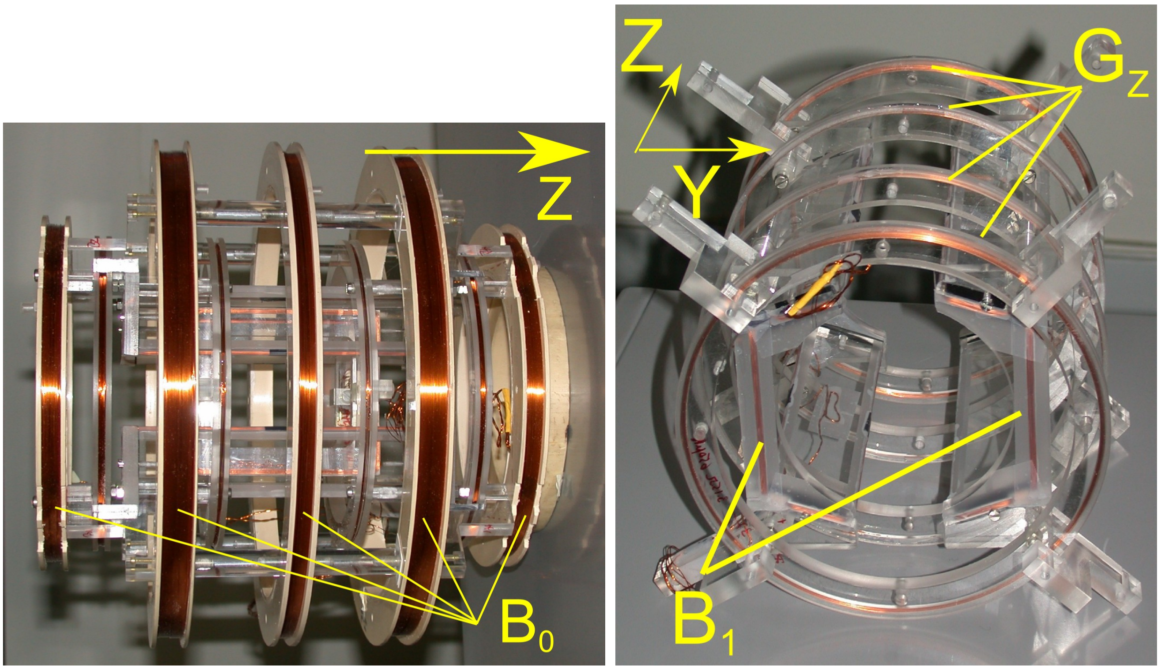

Figure 2.1: Left: Set of B_0, B_1 and G_Z coils, with the five B_0 coils marked by yellow lines. For the three larger coil frames the supporting diameter is d=270 mm; for the two smaller coils d=182 mm. Central coil: w=9 mm-wide winding of N=143 turns. Middle coils: w=15.5 mm, N=223, with their planes of symmetry separated by s=130 mm. Outer coils: w=10 mm, N=166, s=257 mm. All coils are made using 0.5 mm diameter enamelled copper wire. Right: The B_1 and G_Z coils are better seen when extracted from the main magnet bore. Each B_1 half-coil consists of 11 turns of the larger, saddle-shaped winding and 9 turns of the smaller rectangular winding (see [7]). The total coil impedance is R=3.6 Ω, L=0.3 mH. The G_Z coil consist of two outer coils (N=37, d=171 mm, w=3.5 mm, s=204 mm) and two inner coils (N=5, d=174 mm, w=3.5 mm, s=77 mm) connected in series in a Maxwell configuration.

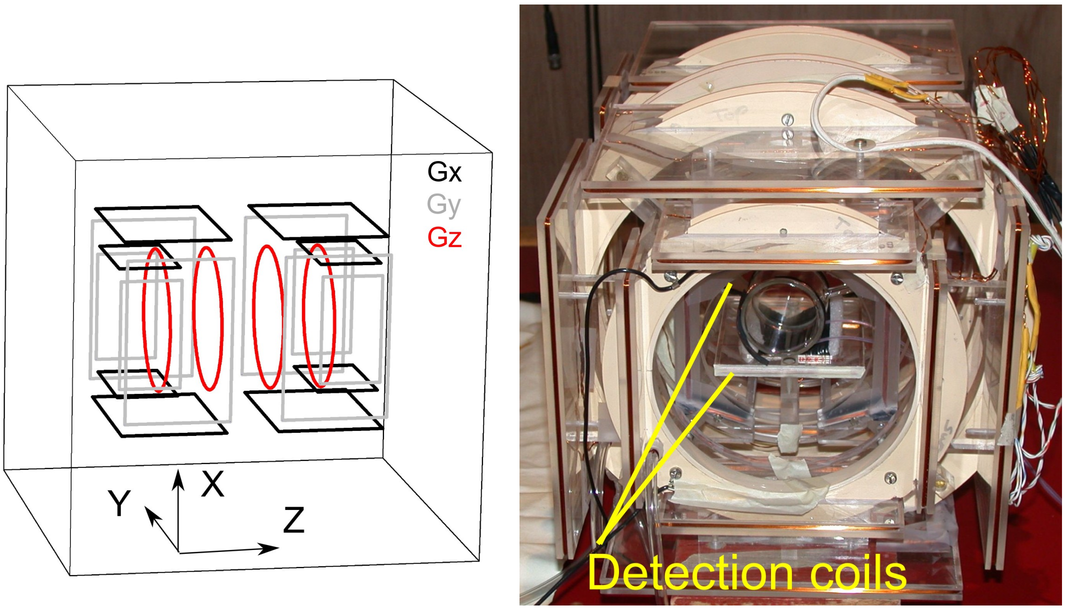

Figure 2.2: Left: Gradient coils schematics; G_Z coils are drawn in red color (dimensions in the caption of Figure 2.1, G_X coils are black, G_Y coils are grey. Small planar coils: 75×135 mm^2, N=12, s=150 mm; large planar coils: 130×203 mm^2, N=20, s=225 mm. Total length of the planar coil set: 325 mm. Right: Photograph of the set of B_0, B_1, all gradient and detection coils assembled together. The position of the detection coils is marked.

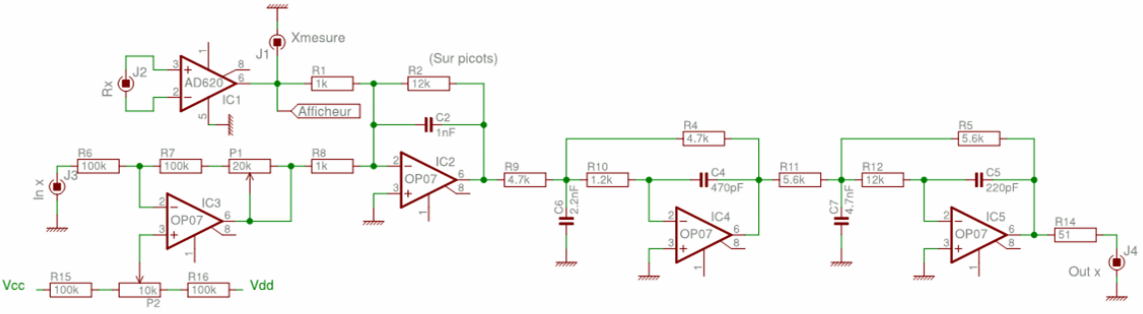

Figure 2.3: Schematics of the system used to control gradient currents (one of the 3 channels is shown). On the left-hand side, InX is the input voltage control from the MRI sequencer; Rx is the voltage across a 1 Ω monitoring resistor connected in series with the gradient coil; P1 is used to adjust the voltage-to-current conversion ratio (usually 1 A/V); P2 is used for shimming. On the right-hand side, the output Outx is connected to the input of a linear bipolar power supply (see text), that feeds current into the monitoring resistor and the coil. The 4th-order Butterworth filter stage provides efficient noise suppression at the NMR frequency with an acceptable limitation of the current ramp time.

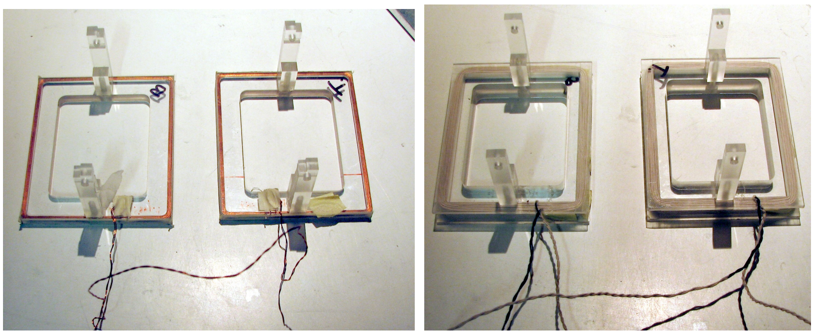

Figure 2.4: Disassembled pairs of detection coils: A made with copper wire (left photo) and C made with copper Litz wire (right photo)

In most of the experiments a low-noise SR-560 preamplifier was used (voltage noise $N_A = 4\ nV/\sqrt{Hz}$). It was used with a gain $G = 10^3$ and internal bandpass filters (30 kHz to 300 kHz).

2.1.6 Q-switch

The Q switch is a home-made active device connected in parallel to the tank circuit, that damps the circuit when an external 5V voltage signal is applied to its TTL control input (see Figure 2.5). It is based on an ADG636 chip. This switch offers ultra low charge injection of 1 pC into the circuit during switching, hence triggers much less ring down than usual CMOS switches when it is switched to the high impedance state to return to the high-Q state.

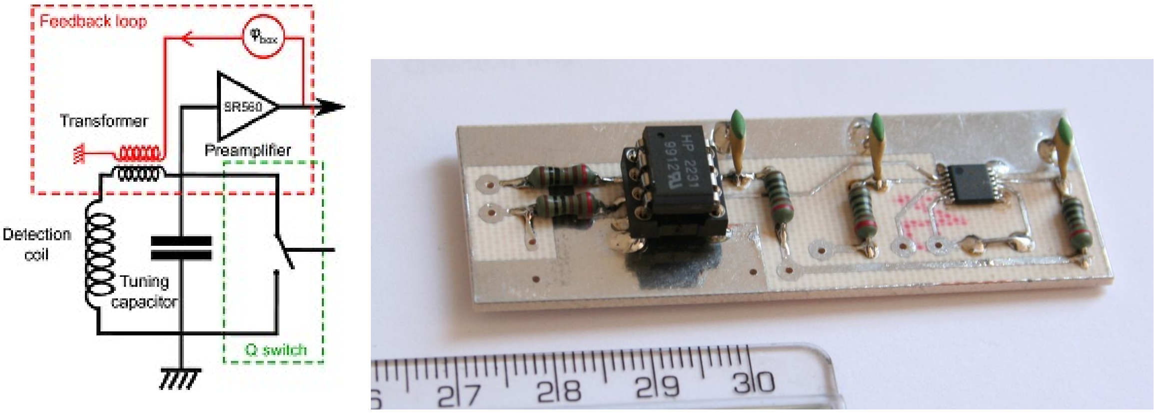

Figure 2.5: Q switch implementation and photo

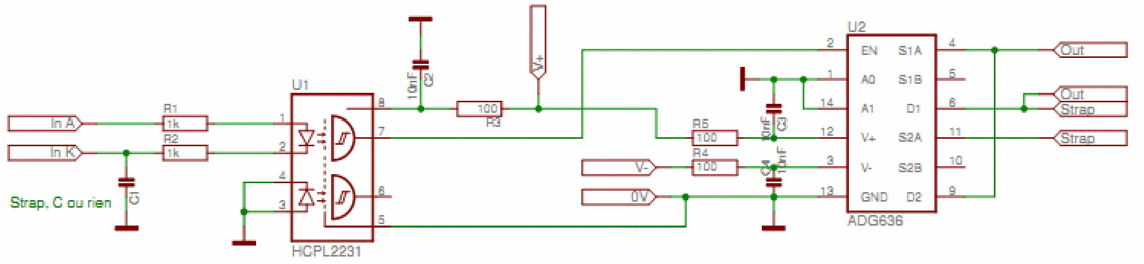

Figure 2.6: Q switch schematics. An optical isolator (HCPL 2231) avoids interference of the digital noise with NMR signals. The two CMOS switches of the ADG636 circuit are connected in parallel to reduce the 'ON' resistance (to 85 Ω ÷2), in an anti-symmetrical way to contribute to reduce total charge injection

2.1.7 Experiment control and data acquisition

Two different schemes were used in our experiments.

2.1.7.1 ADC / DAC. Sequencer

A homebuilt RF gate and DAC controlled by desktop computer with homebuilt software together with continuous RF signal from external RF generator or lock-in were used to control and apply RF pulses. For gradient pulses application homebuilt DAC or homebuilt sequencer were used to control the gradient control box. Standard Ametek 7265 and 7270 lock-ins and following homebuilt ADC were used for data acquisition. Data was stored in a desktop computer with in-house software. This system is based on hardware previously used in the group [7, 26, 28, 29].

2.1.7.2 Apollo Tecmag console

An Apollo Tecmag console was used to apply RF, Gradient and preamplifier blanking pulses and for data acquisition. RF output of 1V pk-pk max. values was connected to the homebuilt RF amplifier that provides a proper pulse power. Outputs of the gradients were connected with the input of the homebuilt gradient control box described earlier in gradient control section 2.1.3. The output of the preamplifier is connected to the Apollo console signal input through a 20dB attenuator to match the voltage levels and avoid damage.

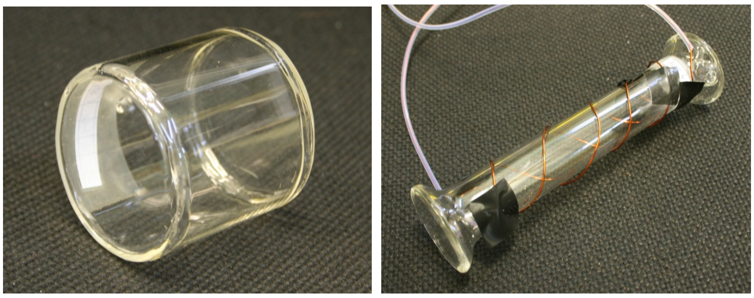

Figure 2.7: Sealed ^{3}He glass cells used in the experiments: 67 mbar with 5 cm inner diameter and 5 cm long (left) and 400 mbar with 1.6 cm inner diameter and 12 cm long (right). Electrodes used for on-site gas polarisation are attached to the longer tube.

2.1.8 Samples

Glass ^{3}He cells and preserved lungs of a small mammalian animal were used in experiments.

Glass cells were of two different types:

- Sealed glass cells contain ^{3}He at various pressures. These cells were prepared by P.J. Nacher and G. Tastevin in LKB laboratory.
  - 400 mbar cylindrical cell with 1.6 cm inner diameter and 12 cm long
  - 67 mbar cylindrical cell with 5 cm inner diameter and 5 cm long

- Open sets of connected glass tubes. Gas pressure inside open cells was controlled by a pressure gauge located in the gas filling line.
  - 2 cylindrical tubes with 1.1 cm inner diameter and 5 cm long
  - 5 cylindrical tubes with 0.7 cm inner diameter and 5 cm long

Photographs of the cells are shown in Figures 2.7, 2.8 and 2.9.

Preserved lungs of a small mammalian have been ordered from *Nasco*[1] company. Lungs were stored in a special preserving liquid (75% of water, 24% of propyleneglycol, 1% of toluol). Set of lungs that was used allowed for 4 cm^3 max. inhaled gas volume. Lungs were placed inside the special box with hermetical cover. Photograph of the lungs

---

[1] 901 Janesville Avenue, P.O. Box 901, Fort Atkinson, WI 53538-0901, USA, www.enasco.com

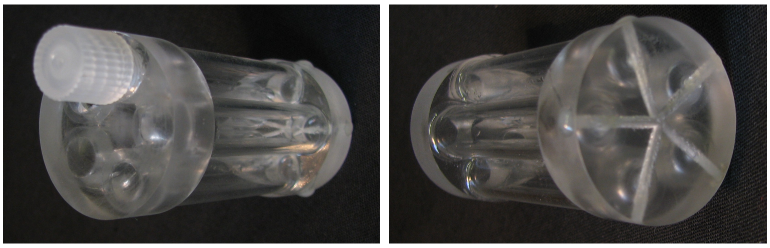

Figure 2.8: An open set of 5 connected glass cells (made from tubes) used in the experiments. Connection lines are visible on the right photograph

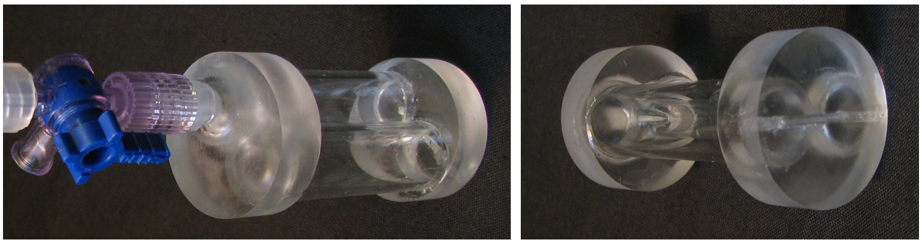

Figure 2.9: An open set of 2 connected glass cells (made from tubes) used in the experiments. Connection lines are visible on the right photograph

inside this box is shown in Figure 2.10. Trachea is connected to the tube connector and can be connected to the outer gas line tubes. The box is filled with the preserving liquid, pressure of the liquid is controlled from outside. In our experiments, liquid volume was connected to the body of a syringe (piston removed) via a flexible tube. Thus, it was possible to make a simple measurement of the volume of the gas inside the lung by changes of the liquid level in the syringe.

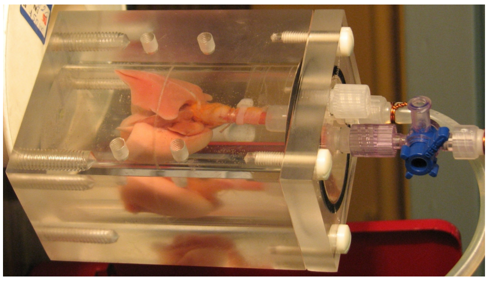

Figure 2.10: Photograph of the preserved lungs used in the experiments

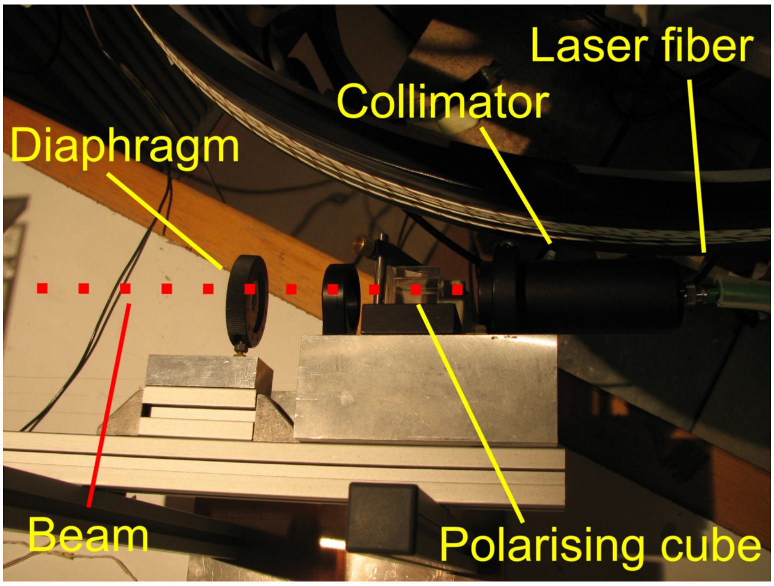

Figure 2.11: Part of the on-site gas polarization system. Collimator, polarising cube, diaphragm and photo-diode were attached to the non magnetic frame.

2.1.9 Polarizing the gas

For the experiments with sealed gas cells, ^{3}He gas was polarized on-site with 2W 1083 nm Keopsys laser by MEOP method [30]. Laser output fiber is passed through the Faraday cage and the beam is collimated. After that it passes a polarising cube and a $\lambda/4$ plate. Diaphragm is used to adapt the beam size. Figure 2.11 shows the collimator, polarising cube, diaphragm and photo-diode attached to the non magnetic frame. After a double pass through the cell, the beam is deflected by the polarising cube at the angle of 90^o and its power is measured by a photo diode [31]. Signal from the photo diode allows to tune the laser on proper pumping line. In our experiments C9 atomic line was used during optical pumping [32]. Sealed cells are covered with electrodes for creating electric discharge. The rf generator and the rf power amplifier are located outside of the Faraday cage. Nuclear polarization was measured by NMR methods. Typical values of the nuclear polarization of the ^{3}He gas are $P = 4\%$ for 67 mbar 5 cm long cell and $P \approx 1\%$ for 400 mbar 12 cm long cell. The rf discharde is turned off after 1-3 minutes of polarisation for NMR acquistion.

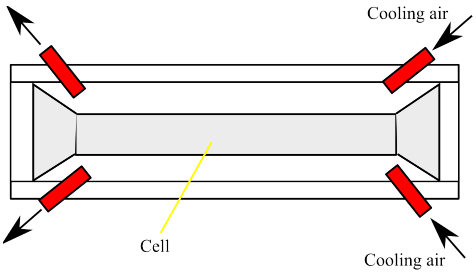

Figure 2.12: Schematics of an air cooling inside the cell holder. Tube is fixed in a leakproof box. Cooling air is injected and goes out through the special holes. Horizontal section is shown.

2.1.10 Temperature control and air cooling

The stability of the gas temperature is very important for correct analysis of diffusion experiments data. High power RF discharges applied to the sealed cells heat the gas. A special PTFE holder with a possibility of air cooling was constructed. Figure 2.12 shows schematics of used air cooling. Temperature shifts of the cell were measured by a thermopair during of the rf discharge application (on the 1st, 2nd and the 5th minutes) and after it (on the 1st, 2nd and the 5th minutes). During measurements cell was free, or inside a plastic foam holder, or inside an air-cooled holder. Measured values are presented in Table 2.3. Typically for the sealed cells temperature was changing over a wide range of 20°. Using air cooling allows to stabilize the temperature of the cell within the range of ±1°.

Table 2.3: Time dependence of the cell temperature shift during and after an application of rf discharge for various cell holders. Differences of a cell and a room temperature are given.

.	**rf discharge is on**			**rf discharge is off**			
Time, min	**1**	**2**	**5**	**1**	**2**	**5**	**10**
Cell without holder	8.2	8.4	—	6.8	5.2	2.5	0
Cell in a foam plastic holder	19.6	24.5	28.7	24.1	20.0	11.7	5.6
Cell in a teflon air-cooled holder	0	1.5	0	0	0	0	0

2.1.11 Gas management

In all experiments with open ^{3}He cells and preserved lungs the samples were filled with gas using two methods:

1. Filling the cells and lungs with hyperpolarized gas next to the polarizer located in the room next door [31], and then transport the cells into the MRI setup. Losses of the nuclear polarization during switching the field in polarizer and transporting the cells through the field gradients are empirically found to be less than 20% of the total polarization.
2. Filling the cells and lungs with hyperpolarized gas inside the magnet using ^{3}He storage cell and a homemade compressor. Schematics of the gas system is shown in Figure 2.13. Glass storage cell (volume about 500 cm^3) with gas is located in the Faraday cage. In our experiments, longitudinal relaxation time T_1 of the gas magnetization was T_1 $\approx$40 min. Gas is transfered from the storage cell via compressor to the cells to be imaged. After experiments, gas is transfered via compressor to a storage bag for recycling.

2.1.12 Faraday cage and line filters

The MRI system was placed inside a simple home-made Faraday cage consisting of soldered 0.5 mm thick copper sheets that provides a 100-fold reduction of the picked-up interference noise around 100 kHz [7]. Line filters were used to reduce interference noise entering the Faraday cage. They were inserted in the gradient coils lines, B_0 field power line and light power supply (12V DC) lines. All the filters are located on the wall of the Faraday cage (see Figure 2.14). The filters on the gradient lines have been chosen so as to make little effect on the gradient pulses rise/fall times or amplitudes.

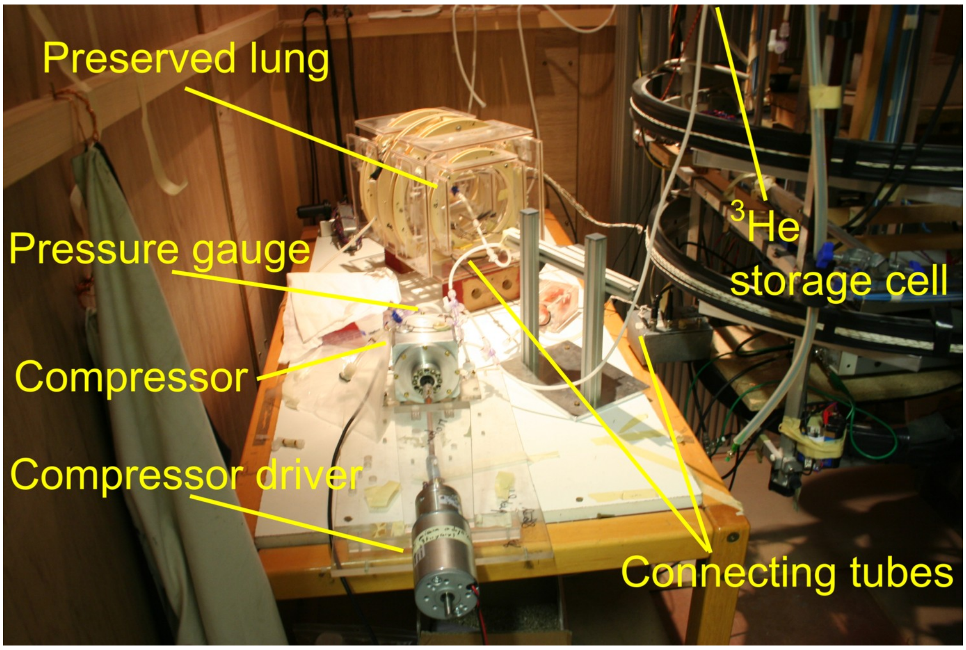

Figure 2.13: Gas management: disposition of the storage cell, compressor and the samples. Before a NMR experiment, gas from the storage cell transfers via compressor to the sample. Gas pressure is controlled by pressure gauge. After an experiment, gas recycles to the recycling bag via compressor.

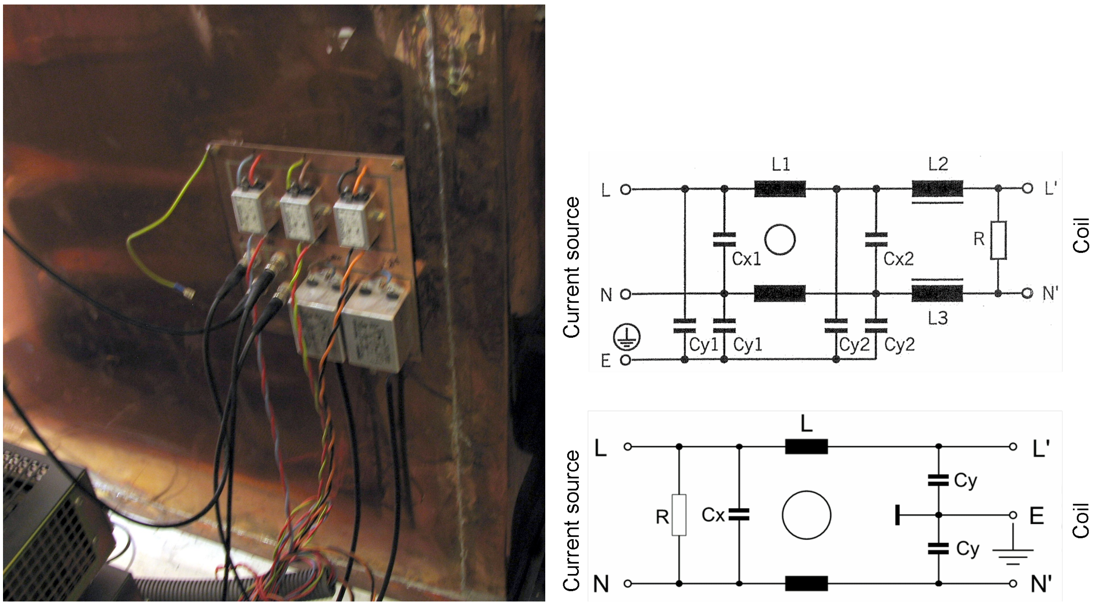

Figure 2.14: Left: Photograph of the filters used on the lines entering the Faraday cage (see text). Right: Schematics of the commercial EMC-RFI suppression filters. Upper filter: Timonta FSS2-65-6/3 2-stage filter used for B_0 and light currents (L1=6, L2=0.5, L3=0 (mH), Cx1=100, Cx2=680, Cy1=10, Cy2=4.7 (nF), R=1MΩ). Lower filter: Schurter 5500.2040 1-stage filter used for the Z gradient line (L=2 mH, Cx=15, Cy=2.2 (nF), R=1MΩ), max. current 3A, or Schurter 5500.2041 filters used for the X and Y gradient lines (same except L=0.8mH and max. current 6A)

2.2 Setup characterization

2.2.1 Field inhomogeneity

Static magnet field inhomogeneity is a very important parameter that sets the limits on the reliability of the experimental data and the acquisition time. The main reason of the field inhomogeneity is an imperfect construction and assembly of the magnet. An application of the small DC currents i_x, i_y and i_z into the gradient coils G_X, G_Y and G_Z allows to partially compensate the static field inhomogeneity created by B_0 coils in the center of the magnet (corrections of the 1st order). Characterization of the field inhomogeneity and adjustment of the DC currents was made by a FID signal decay rate. Sealed cylindrical glass cell with ^{3}He gas under 1.38 mbar pressure was used as a sample. The computed field map inhomogeneity should lead to a decay of the FID with the

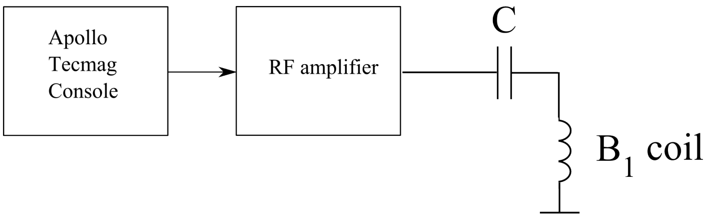

Figure 2.15: Schematics of the RF line. A RF pulse generated by the Tecmag console after amplification by RF amplifier goes into the RF circuit which contains B_1 coils and is tuned in a series with a capacitor. The diodes block the noise from the amplifier when no pulse is applied.

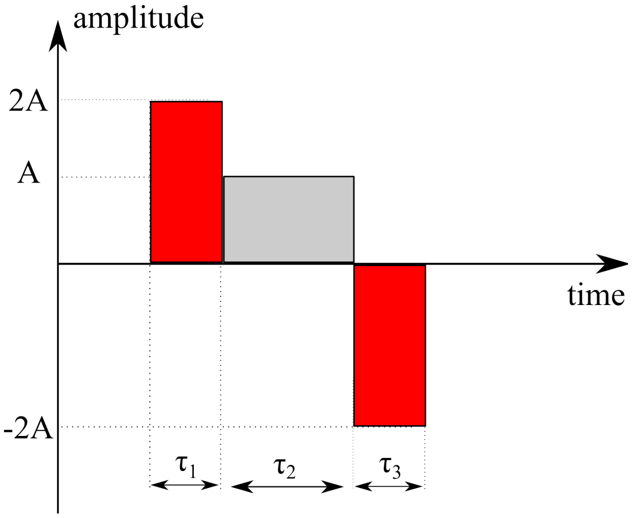

Figure 2.16: Schematics of a special RF sequence that allows to reduce distortions of the B_1 field pulse shape

time $T_2^* = 780$ s, while the actual time is $T_2^* = 2.8$ s after first order of shimming by linear gradients. Residual field inhomogeneities over a cell size are 17 times higher than expected due to imperfect magnet assembly [13].

2.2.2 RF pulses

RF output of the Apollo Tecmag console is connected to the RF amplifier. The output of the amplifier is connected with the RF circuit that includes B_1 coil that was used to generate the tipping B_1 field.

The RF circuit is tuned in a series capacitors to a frequency close to a frequency

85.4 kHz. This allows to have a low circuit impedance matched to one of the RF amplifier, and a high current. The quality factor Q of the circuit is 10. This leads to changes in the current amplitude slower than specified by the initial pulse of the Apollo Tecmag console. In other words, the current pulse shape in the RF line is significantly distorted. Example of such RF pulse distortion for the rectangular pulse is shown in Figure 2.17. On this figure the output of the Apollo Tecmag console and the voltage across capacitor of the rf circuit are plotted. In order to have a better pulse shape a special RF sequence was used for the experiments controlled by the Tecmag console. To obtain a shape of the B_1 pulse as close to rectangular shape as possible, the pulse of the Apollo Tecmag console should consist of 3 parts:

1. pulse with duration τ_1 with twice the amplitude of the desired level to provide a fast rise time
2. pulse with duration τ_2 with normal amplitude level
3. pulse with duration τ_3 with doubled amplitude of the desired level and opposite phase in order to suppress the pulse ringdown as fast as possible.

Schematics of the sequence is shown in Figure 2.16. This sequence is similar to the one suggested by Hoult [23] with an additional constraint. At the frequency of 85 kHz, the RF pulse duration is the order of the RF oscillation period. The situation when magnetization precess only few times during the pulse duration is discussed in [26] and it can lead to an additional parasite changes of the magnetization. An application of RF pulses with durations equal to integer number of the half-periods of the RF oscillations is described as a solution to decrease undesired magnetization changes and following errors when NMR sequences are applied. Thus, additional conditions on the durations τ_1, τ_2 and τ_3 was set in this work: they were chosen as an in integer number of the half-periods of the RF oscillations. And a slight change of the RF frequency required a proper revision of the τ_1, τ_2 and τ_3 durations. Thereby all timings and amplitudes of these 3 parts were matched together to avoid any unexpected oscillations. An example of this sequence application is shown in Figure 2.17. In other experiments, for very low tip angle pulses, the 2nd part was suppressed. However, the sequences for the rf pulses with more complicated shape are

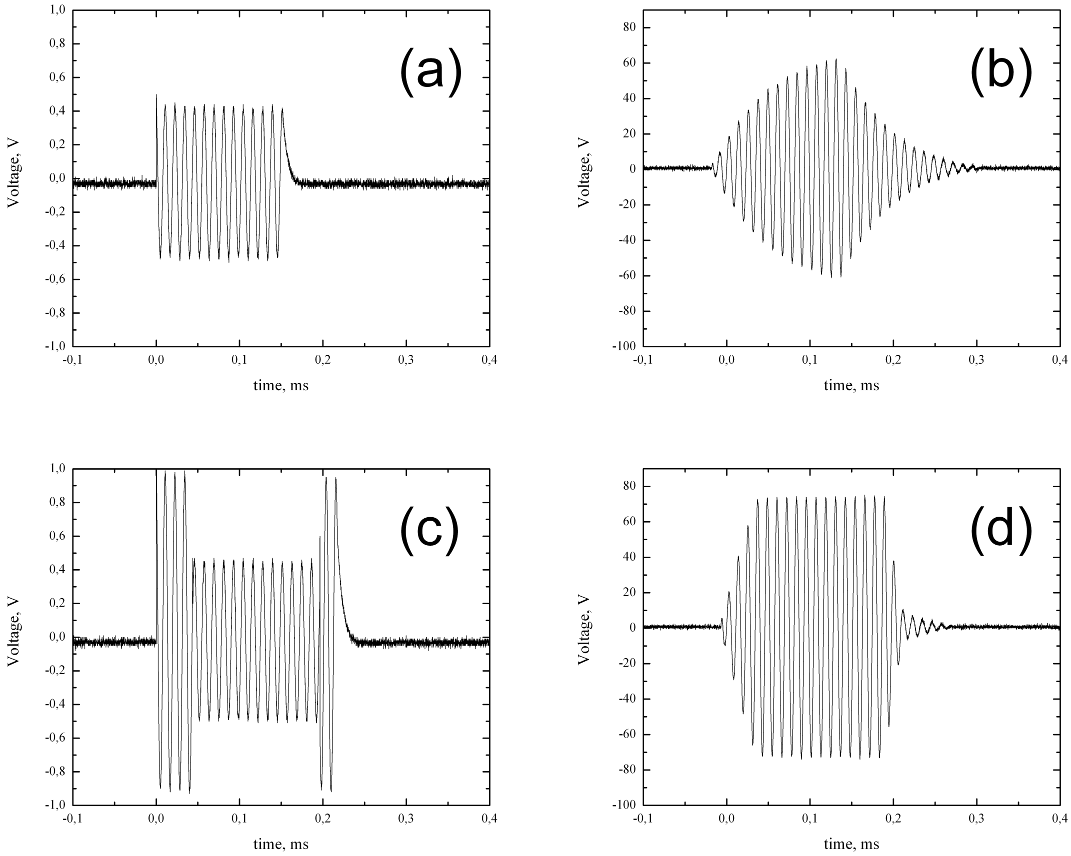

Figure 2.17: Outputs of the RF channel of the Tecmag console (a) and (c), and corresponding to them voltages across the capacitor in the RF circuit (b) and (d). Distortions of the rectangular RF pulse require an application of the more complicated RF sequences

much harder to develop. The typical values of the produced B_1 field during experiments on ^3He are easy to calculate using the fundamental relation $\omega = \gamma B$. Typical $\pi/2$ pulse durations of 300 μs to 4 ms lead to the maximum achieved field value $B_1 = 0.16$ mT.

2.2.3 Gradient pulses

Information on the shape of the gradient pulses is important for the diffusion experimental data analysis. Examples of gradient pulses (to be more precise, currents in the gradient lines) for all three directions X, Y and Z obtained for our coils are presented in Figure 2.18. Gradients were driven by KEPCO BOP-36 and BOP-50 power supplies and rectangular shape of the pulses was expected. The typical rise and fall time of the gradient pulses lies

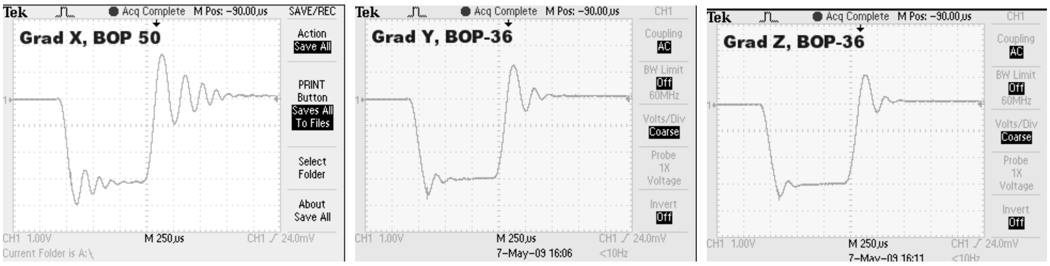

Figure 2.18: Examples of gradient currents in various gradient coils (from left to right: G_X, G_Y, G_Z) and power supplies (KEPCO BOP-36 and BOP-50).

om the 70-150 μs range for the gradients amplitudes used in our experiments. Durations of the oscillations induced by current switching are shorter than 250 μs. Test experiments using a gradient meter have been made to verify that the gradient pulses created by set of coils are consistent with the applied current.

The gradient meter made by the Orsay group consists of 2 coils. The raw signal from the gradient meter is the time derivative of the actual gradient pulse. After corrections of the baseline, integrated acquired data were compared with the recorded current changes in the coils. Illustration of the measured actual gradient pulse and the current in gradient line for the X gradient coils is shown in Figure 2.19. Gradient pulses completely match with the current. This fact proves that the filters introduced in the gradient lines are adequate.

2.2.4 Using an active feedback and Q-switch system in the NMR signal detection circuit

2.2.5 Active feedback in the detection system

The principle of operation and performance of the system have been discussed in [26, 33]. Signal from the tank circuit goes to the preamplifier SR-560 with gain factor $G = 10^3$. One of the outputs of the preamplifier is connected with homemade device ("phase box"), that can adjust feedback signal by change in the phase and in the amplitude. Examples of the adjusted sinusoidal signal by "phase box" are illustrated in Figure 2.20. The output of this device is connected with the tank circuit by inductively coupled coils to provide a feedback. Schematics of the "phase box" can be found in [26]. Coupling coils

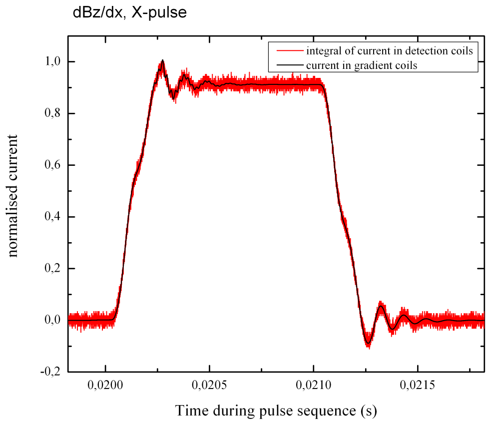

Figure 2.19: An example of the measured current in the gradient line (black line) and actual gradient pulse (red line) matching. Actual gradient pulse evolution was obtained by the proper acquired by gradient meter data integration. Gradient coils X were used to create a pulse.

(photo is shown in Figure 2.21) were wound on the same frame with diameter 0.5 cm, number of turns 10 by copper wire with 0.5 mm diameter. Measured mutual inductance is $L_M = 3.4\ \mu$ H. Stability of the "phase box" and the active feedback operation have been very well described in [26].

2.2.5.1 Active feedback in the detection system. Detection bandwidth and SNR

From the theoretical considerations made in Chapter 1 it comes that change in the phase and the gain of the feedback loop leads to the change of an effective Q factor of the detection circuit. In our experiments, the tank circuit was tuned to 86.5 kHz and had the quality factor $Q = 180$. An example of significant bandwidth broadening by an active feedback is illustrated in Figure 2.22. Active feedback significantly damped the effective Q factor of the circuit (10 times) according to the expectations. Detection bandwidth increases at the same time from 0.48 kHz to 4.8 kHz. Further increase of the bandwidth to the desired value by adjusting the feedback settings makes active feedback a very convinient broadening solution.

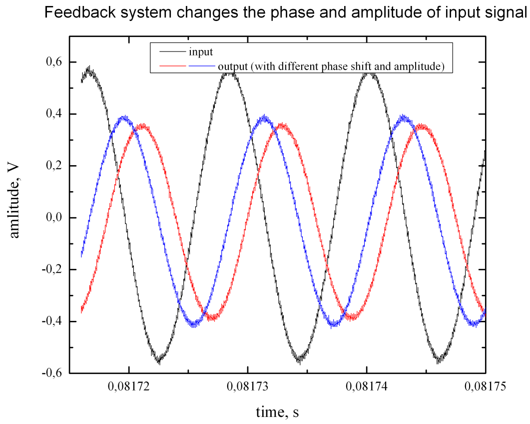

Figure 2.20: Examples of the adjusted sinusoidal signal by “phase box”. Input signal (black) and output signals for various tuning settings of the “phase box” (blue and red) have different phase and amplitudes.

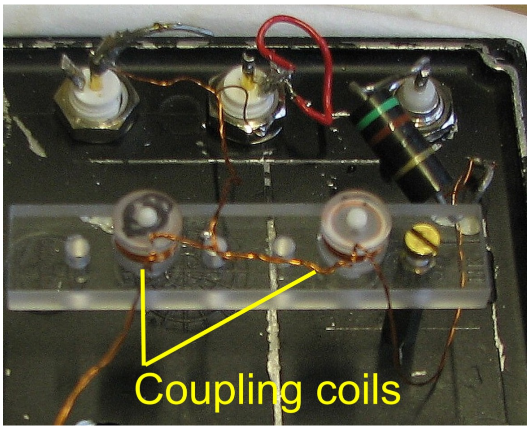

Figure 2.21: Inner part of the box with coupling coils. Tank circuit and feedback loop are connected to the coupling coils. Measured mutual inductance of the coils is $L_M = 3.4$ μ H

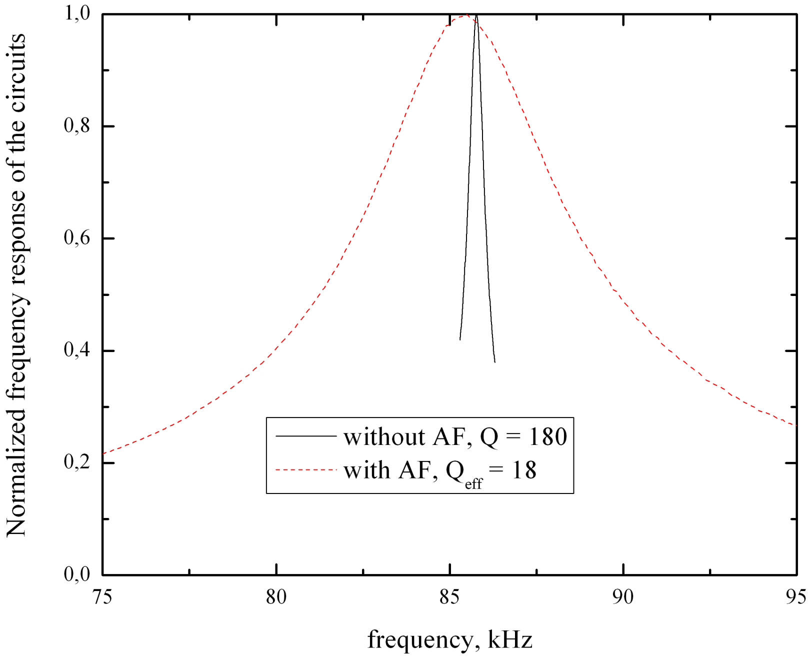

Figure 2.22: An example of significant bandwidth broadening by an active feedback. Measured frequency responses of the tank circuit (black solid line) and the circuit with an active feedback (red dashed line) are presented. Relative change of an effective quality factor of the detection system equals to 10 (Q = 180 for the tank circuit and $Q_{eff} = 18$ for the circuit with an active feedback).

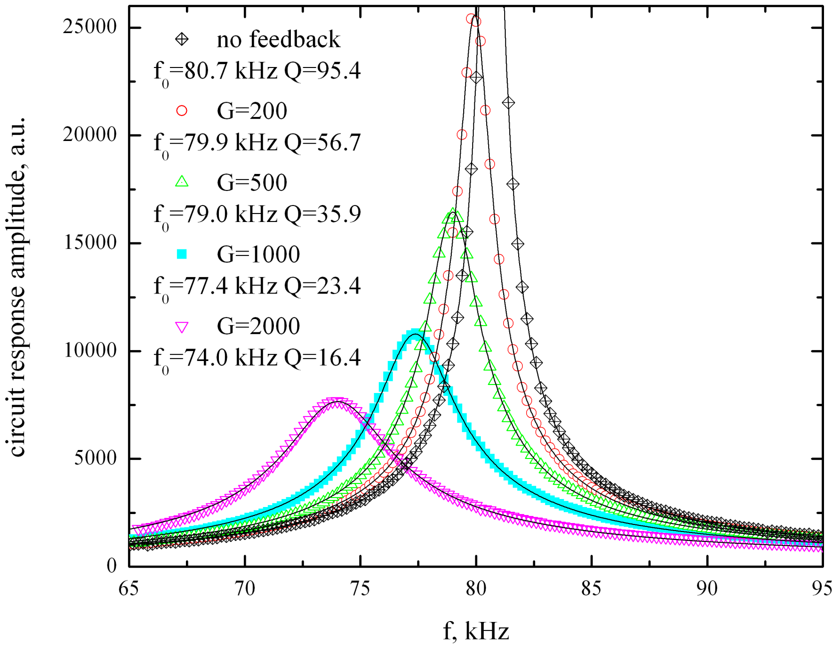

Figure 2.23: Examples of resonance shifts while an active feedback is used. Measured frequency responses of the circuits for a given preamplifier gain factors G are presented.

2.2.5.2 Active feedback: Resonance shifts

From equation 1.72 it comes that feedback loop can shift the resonance frequency of the detection circuit, depending on the feedback loop phase. Examples of the resonance shifts were detected for few sets of feedback parameters (preamplifier gain factor varied from 200 to 2000). Measured frequency responses of the tank circuit with $Q = 95.4$ tuned to 80.7 kHz with applied feedback are shown in Figure 2.23. Significant change of the resonance frequency from 80.7 kHz up to 74.0 kHz, as well as changes of the effective Q_{eff} from 95.4 to 16.4, are observed. In particular case of our experiments, the detection circuit with an active feedback has a resonance frequency of 85.4 kHz, while the resonance frequency for the same circuit without any feedback applied is 86.1 kHz. The feedback phase must be carefully checked to avoid undesired changes of the resonance frequency.

2.2.5.3 Fast acquisition

Detection system saturates after the rf-pulse due to imperfect crossing of the B_1 and detections coils. The recovery time from the saturation could be a few ms. This makes fast sequences with a large number of rf pulses impossible to use. However, several methods allow us to reduce the saturation effects:

1. to damp a Q-factor of the detection circuit by Q switch during rf pulse.

2. to use active feedback.

The effect of all these methods was observed in our system for CPMG pulse sequence (see section 3.2.1 for more information) and is illustrated in Figure 2.24. In addition, the preamplifier was blanked during the rf pulse to avoid additional saturation of the feedback loop. The same pulse is used to control the Q-switch in our experiments. It can be clearly seen that, simultaneous use of the feedback, Q switch and preamplifier blanking allows to implement faster sequences. Both methods, an active feedback and a Q-switch, efficiently reduce the ringdown time from 2.5 ms to 0.7 ms each and up to 0.3 ms together. Possibility of fast sequence application increases the range of sequence parameters and allowed us to perform our studies in a wide range of sequence timings (Chapter 3 and 4).

2.2.6 Noise in the system

In this section actual noise in the system will be characterized.

The noise voltage on the output of the detection coils was measured using lock-in in the frequency ranges of experimental interest 75 - 98 kHz and 105 - 120 kHz with a 500 Hz step. During experiments, the detection circuit with the pair of coils “A”, Q $=$ 18 was tuned to 88 kHz or to 110 kHz, depending on the chosen frequency range. The time constant parameter of the lock-in (640 μs) limits the bandwidth of the recorded noise signal. In our case it limited the bandwidth to 390 Hz. Used lock-in model does not allow us to record directly the noise level. In-house software was used for quick analysis of the acquired data. After FFT of the initial data, the signal was divided on the root of the frequency bandwidth of each step. The final noise values against the frequency

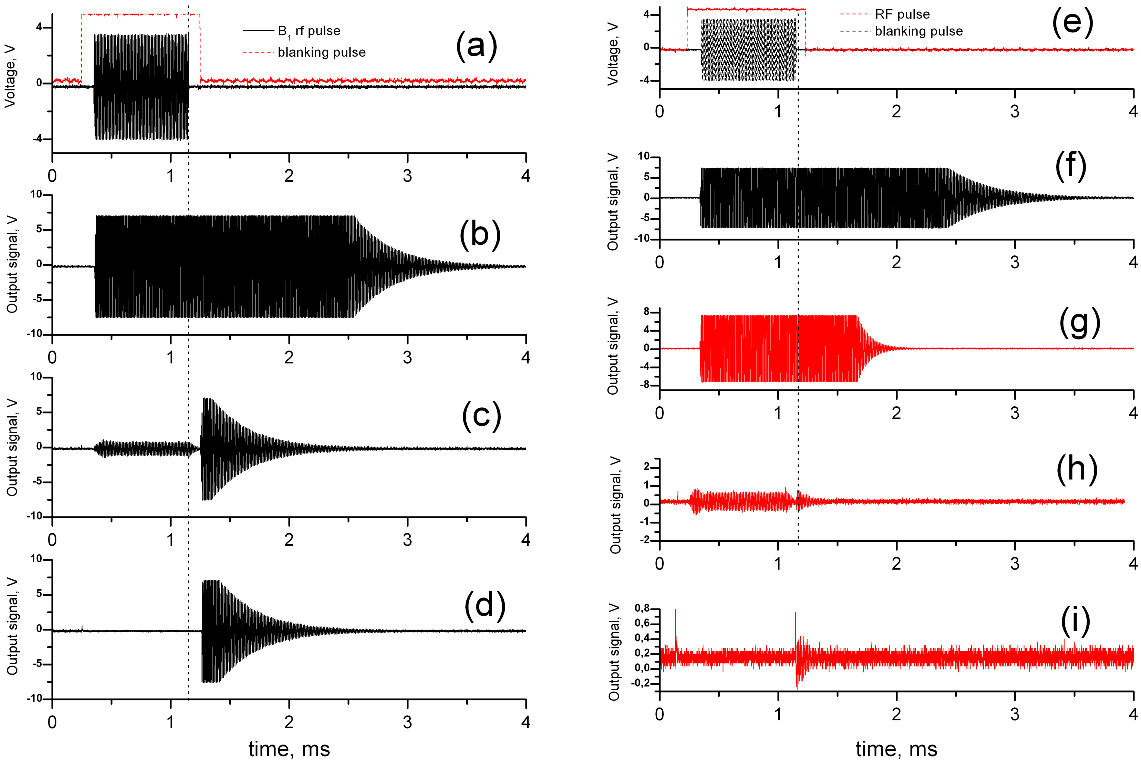

Figure 2.24: Implementation of the Q-switch and the active feedback allows for a fast data acquisition: (a) and (e) applied rf and blanking pulse, (b) and (f) voltage on the output of the preamplifier for tank circuit, (c) voltage on the output of the preamplifier for circuit with a Q-switch, (d) voltage on the output of the preamplifier for circuit with a Q-switch and preamplifier blanking, (g) voltage on the output of the preamplifier for circuit with an active feedback, (h) voltage on the output of the preamplifier for circuit with a Q-switch and an active feedback, (i) voltage on the output of the preamplifier for circuit with a Q-switch, an active feedback and the preamplifier blanking.

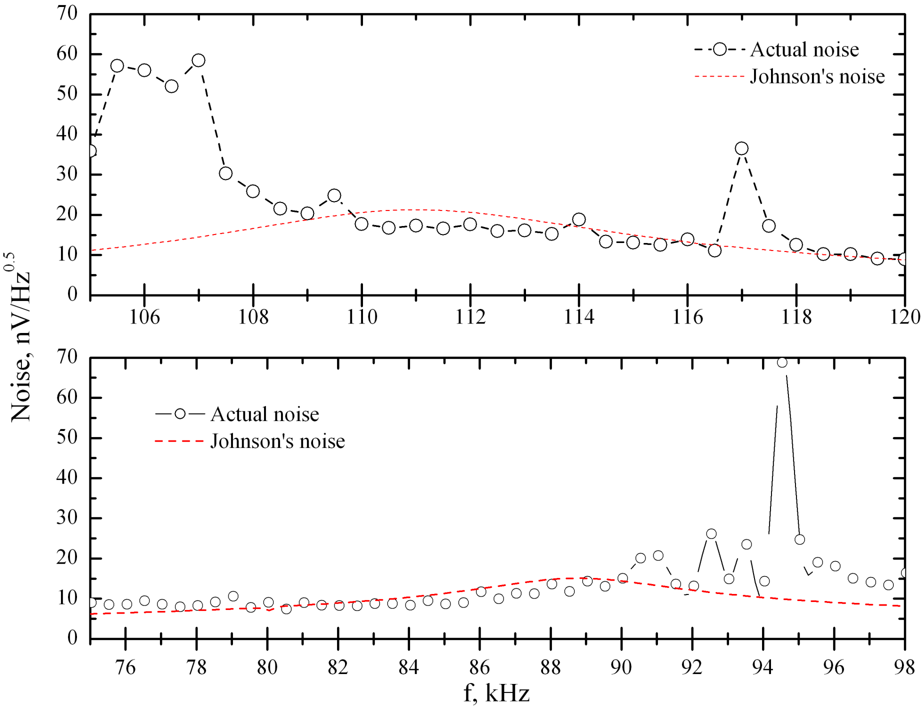

Figure 2.25: Measured noise spectrum (open circles) in 2 frequency ranges of 105 - 120 kHz (top) and 75 - 98 kHz (bottom), and the estimated Johnsons noise values (red dashed line). Parasitic noise from external sources and the Johnsons noise are the dominating sources in our experiments.

are plotted in Figure 2.25. Parasitic noise from the external sources limits the range of the suitable frequencies of MRI experiments, operation on 85 ± 5 kHz is the optimal choice for this system. Frequency of 85 kHz was chosen as a resonance frequency in our experiments. Frequency dependence of the tank circuit impedance was measured and then the Johnsons noise calculated. Thermal noise was found as a dominating source of noise in the range of 80 - 89 kHz.

2.2.7 Concomitant gradients

Acquisition of MRI at low fields involves unavoidable concomitant gradients that can result in severe image distortions. Concomitant gradients issues at low and ultra low field MRI are considered and widely studied in many articles [34–38]. This effect is a straight consequence of the Maxwell's equations on the magnetic field $\vec{B}$:

$$\nabla \cdot \vec{B} = \frac{\partial B_x}{\partial x} + \frac{\partial B_y}{\partial y} + \frac{\partial B_z}{\partial z} = 0 \tag{2.1}$$

$$\nabla \times \vec{B} = \left(\frac{\partial B_z}{\partial y} - \frac{\partial B_y}{\partial z}\right)\vec{i} + \left(\frac{\partial B_x}{\partial z} - \frac{\partial B_z}{\partial x}\right)\vec{j} + \left(\frac{\partial B_y}{\partial x} - \frac{\partial B_x}{\partial y}\right)\vec{k} = 0 \tag{2.2}$$

From the equations it comes that if you create the gradient $\frac{\partial B_z}{\partial y}$, then the gradient $\frac{\partial B_y}{\partial z}$ has also non-zero value. It is impossible to create field gradient in one direction without introducing a concomitant gradient in an orthogonal direction to it.

At low fields, a strength of the concomitant gradient can achieve the same level as the applied gradients. High concomitant gradients comparably to the magnetic field can significantly distort magnetic field lines that will yield a MRI image distortion. Magnetic field strength and direction become inhomogeneous over a sample. Angle of the spin precession β (between spin magnetization and the z axis) under the applied gradients and the field strength depends on the position from the center and the direction of the applied gradients. For an applied gradients G_x and $-G_x$ along x axis, changes of the angle and the resonance frequency ω can be written as [38]:

$$\tan \beta_{\pm} = \pm \frac{G_x z}{B_0 \pm G_x x} \tag{2.3}$$

$$\omega_{\pm} = \gamma \left[(B_0 \pm G_x x)^2 + (G_x z)^2\right]^{1/2} \tag{2.4}$$

This effect depends on the position from the center. The minimal magnetic field distortions are in the center of the magnet and grow from the center to the edges. For the cylindrical 12 cm length cell with 1.8 cm inner diameter, the maximum variations of the Larmor frequency for the 5 mT/m gradient are $\omega_+ \approx 92.54$ kHz for positive gradient and $\omega_- \approx 86.85$ kHz for the negative gradient and the angle of the precession axis will vary from $\beta_+ \approx 12.14^0$ to $\beta_- \approx 12.95^0$ for the local magnetization .

Besides an image distortion, the difference in the effect of positive and negative gradient pulse application is a potential source of imperfect echoes in the gradient echo sequences. This can lead to a large cumulative errors in a echo trains (see Section 3.5).

Generally, for the set image distortion ϵ along the sample with the length L at the magnetic field B_0, the gradient strength G should satisfy a following relation [38]:

$$G < \epsilon \frac{4}{B_0 L} \tag{2.5}$$

For 5 mT/m that is the maximum limit of our setup and 2.7 mT magnetic field, the image distortions over our sample (up to 12 cm long) should not exceed 0.4%.

Also it must be noticed that fast switching of the gradients at low fields can make an effect on the sample similar to a rf tipping pulse [38] due to arised concomitant gradients.

Chapter 3

^{3}He Gas Diffusion

In this Chapter ^{3}He gas diffusion issues are discussed. Chapter 3 is divided into few sections. After a brief theoretical introduction, multiple echo diffusion pulse sequences and methods of extraction of information about gas diffusion are described. Then information on various diffusion regimes and crossovers of them are given. Series of CPMG and GE experiments on the sealed ^{3}He cells have been made. Diffusion conditions similar to ones met in lung airways were reproduced in these experiments. Obtained results of these experiments are reported and then discussed, as well as a potential of multiple echo sequences at ultra low fields. Experimental results are compared with existing information from the literature.

3.1 Transverse magnetization decay rate

For describing the signal in HP gas imaging we will consider the local magnetization $\vec{M}$ of some volume of gas. This volume is small enough to consider the magnetic field across its volume as a constant, but big enough to represent a large number of spins. In the general case, the magnetic field applied to a small volume of spins is the sum of the applied B_0 field, the field B_1 created by rf pulse and the effect of the applied gradients $\vec{G}$.

$$\vec{B}_{ext} = \vec{B}_0 + \vec{B}_1 + \vec{r}\vec{G} \tag{3.1}$$

The Bloch differential equations describing evolution of the magnetization $\vec{M}$ in the external magnetic field $\vec{B}_{ext}$ can be written as ([39]):

$$\frac{d\vec{M}}{dt} = \gamma\vec{M} \times \vec{B}_{ext} + \frac{1}{T_1}\left(M_0 - M_z\right)\vec{z} - \frac{M_{xy}}{T_2} - D \cdot \Delta\vec{M} \tag{3.2}$$

where T_1 and T_2 are the relaxation times, M_0 is the equilibrium magnetization, M_{xy} and M_z are transverse and longitudinal components of the magnetization, D - diffusion coefficient. For ^{3}He, the gyromagnetic ratio is $\gamma = (2\pi \times 32.2434)$ MHz/T. The first term of the Bloch equation corresponds to the precession of the magnetization in the magnetic field, the second and the third terms - to relaxation processes and the last one to the magnetization evolution due to the diffusion of the spins.

The general solution the case of $\vec{B}_{ext} = \vec{B}_0$ and absence of diffusion ($D = 0$) can be written as ([40]):

$$M_x(t) = M_x(0)\cos\omega_0 t \tag{3.3}$$

$$M_y(t) = M_y(0)\sin\omega_0 t \tag{3.4}$$

$$M_z(t) = M_z(0)e^{-t/T_1} + M_z(\infty)(1 - e^{-t/T_1}) \tag{3.5}$$

Or, after switching to a complex magnetization $M_+ = M_x + iM_y$ and $M_- = M_x - iM_y$ and taking into account that for HP gases $M_z(0) \gg M_z(\infty)$, solutions can be written as:

$$M_+(t) = M_+(0)e^{-i\omega_0 t - t/T_2} \tag{3.6}$$

$$M_-(t) = M_-(0)e^{i\omega_0 t - t/T_2} \tag{3.7}$$

$$M_z(t) = M_z(0)e^{-t/T_1} \tag{3.8}$$

For the particular case, when the relaxation terms ($T_1, T_2 \to \infty$) are neglected, the Bloch equations will become as

$$\frac{d\vec{M}}{dt} = \gamma\vec{M} \times \vec{B} - D \cdot \Delta\vec{M} \tag{3.9}$$

General solution of this particular case in the presence of the field gradient $\vec{G}$ will be a following one ([40]):

$$M_+(t) = Ae^{-i\gamma\vec{r}\int_0^t \vec{G}(t')dt'} \tag{3.10}$$

where the parameter A is a function of time $A = A(t)$ and is defined by the following equation:

$$\frac{\partial A(t)}{\partial t} = e^{i\gamma\vec{r}\int_0^t \vec{G}(t')dt'} D\Delta M_+(\vec{r}, t) \tag{3.11}$$

$$A(t) = \exp\left[-D\gamma^2\vec{r}\int_0^t \vec{G}(t')dt'\right] \tag{3.12}$$

$$M_+(t) = \exp\left[-D\gamma^2\vec{r}\int_0^t \vec{G}(t')dt'\right]\exp\left[-i\gamma\vec{r}\int_0^t \vec{G}(t')dt'\right] \tag{3.13}$$

The parameter A can be simplified for constant gradients ([40]):

$$A(t) = \exp\left[-\frac{1}{3}\gamma^2 DG^2t^3\right] \tag{3.14}$$

If there is no diffusive motion, then the parameter A is a constant A=const.

Dephasing of local magnetizations with time due to an inconstancy of the magnetic field along the sample volume leads to a local Larmor frequency change, and the transverse component of global magnetization M_+ decays with time. Because of the fast spin motions in gases spin-spin interactions are much weaker than ones in a rigid lattice of solid state compounds. Low density of the spins in gases means long distances between them, this also decreases the force of the spin-spin interactions. In pure ^{3}He gas at 1 bar pressure and at room temperature, the diffusion coefficient $D \approx 1.8\ cm^2/s$ and the $T_2 \approx 10$ hours [41]. This T_2 time value is much longer than the one can be obtained using our experimental setup. The main sources of the global field inhomogeneity in our experiments that dephase the spins are a presence of the imperfect static magnetic field and application of constant gradients of magnetic field. Thus, in most of experiments a relaxation channel due to spin-spin interactions can be neglected in a first order of approximation. A transverse magnetization relaxation rate determines the total acquisition time of MR experiments available after each applied rf pulse. This fact makes its studies important for MR imaging experiments. Different gradient pulse sequences techniques will be considered below as potential tools for diffusion measurements.

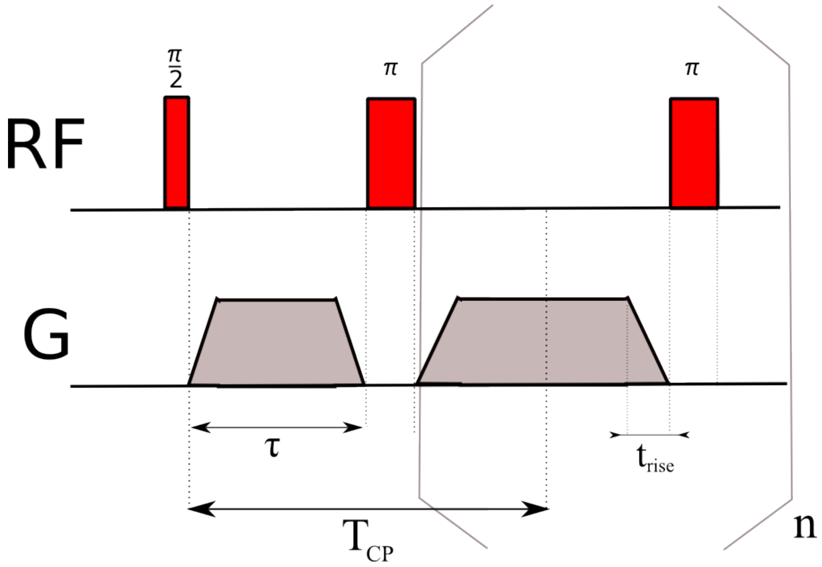

Figure 3.1: Scheme of CP sequences

3.2 Diffusion pulse sequences

3.2.1 Carr-Purcell (CP) sequences

Family of Carr-Purcell sequences is a repetitive rf pulse train with following timing:

$$\frac{\pi}{2} - \tau - \pi - 2\tau - \pi - 2\tau - ... \tag{3.15}$$

Constant gradient pulses with amplitude G are applied during the periods of time τ and 2τ between rf pulses. Spin echoes are created in the center of each time period between each π pulse. All π pulses repeat every $T_{CP} = 2\tau$.

The transverse magnetization relaxation rate $T_{2,diff}^{-1}$ for spin echo experiments can be written as [7]:

$$\frac{1}{T_{2,diff}} = \frac{1}{12}\kappa^2\gamma^2 D G^2 T_{CP}^2 \tag{3.16}$$

Where κ is the correction parameter for a difference between the echo time T_{CP} and the duration of an applied gradient τ_r, caused by a finite duration of the π pulses and non-rectangular shape of the gradient pulses. For “instant” switching rf pulses and perfect rectangular gradient pulses, correction parameter $\kappa = 1$. For rectangular gradient pulses with duration τ_r correction parameter κ can be found from the following equation [42]:

$$\kappa^2 = \tau_r^2 \frac{3T_{CP} - 2\tau_r}{T_{CP}^3} \tag{3.17}$$

For a symmetrical trapezoidal gradient pulses with the both rise and fall time equal to t_{rise} [42]:

$$\kappa^2 = \frac{\tau_r^2}{T_{CP}^2} \left[3 - 2\frac{\tau_r}{T_{CP}} + 6\frac{t_{rise}}{\tau_r}\left(1 - \frac{\tau_r}{T_{CP}}\right) + 3\left(\frac{t_{rise}}{\tau_r}\right)^2 \left(1 - \frac{7}{3}\frac{\tau_r}{T_{CP}}\right) - \frac{14}{15}\left(\frac{t_{rise}}{\tau_r}\right)^3 \frac{\tau_r}{T_{CP}} \right] \tag{3.18}$$

The original CP sequence implies all rf pulses to have the same phase. This is the reason why it is very sensitive to imperfections of rf pulses and is very unstable with time due to a cumulative error effect. Especially this is a big problem at low fields, because the typical duration values of the applied $\frac{\pi}{2}$ and π rf pulses have order of a period of the rf oscillation. Sequences with multiple rf excitations are very sensitive to a rf pulse accuracy, which can become very challenging when the duration of the pulse is a fraction of the rf oscillation period.

The most famous modified CP sequence is a Curr-Purcell-Meiboom-Gill (CPMG) sequence. In this sequence, initial $\frac{\pi}{2}_x$ pulse has a 90^0 (x) shifted phase against all π_y pulses which have phase y. This technique allows to preserve at least transverse components of magnetization, but at the same time to significantly improve stability and independence from π pulse imperfectness. Therefore CPMG sequence was widely used in our diffusion experiments. The main advantages and disadvantages of CPMG sequence are:

1. It reverses magnetization and preserves it for a long time.
2. It is free from $T_{2,inh}$ and allows to measure T_2 instead of T_2^*
3. It allows to neglect the effect of imperfect shimming.
4. As for any spin-echo sequence, both duration of the π pulses and following them dead time of a receiver can significantly reduce number of acquired data points for each echo. Especially it is important for sequences with short echo time T_{CP} time.

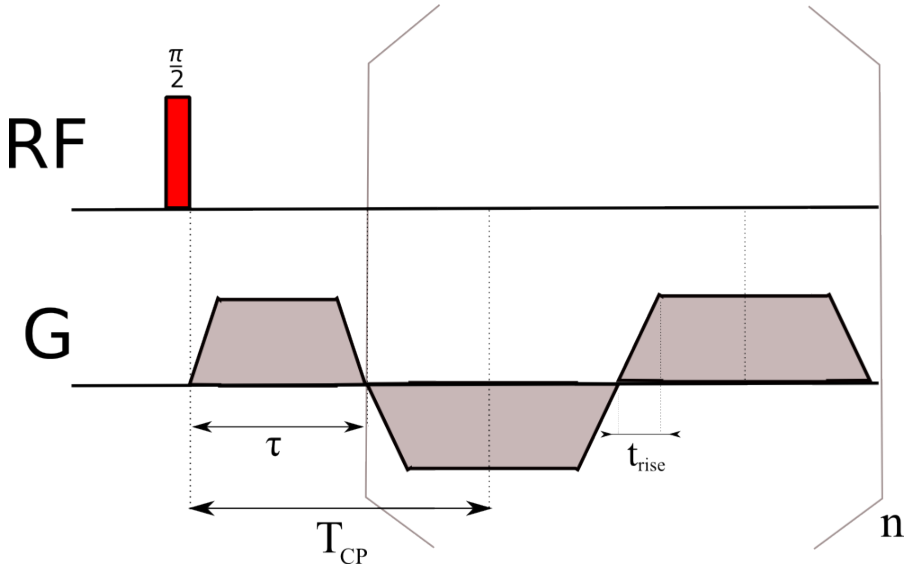

Figure 3.2: Gradient echo sequences

Family of CP sequences consists of many ones with a difference in rf pulse phase alternation algorithms which allow to preserves all three components of magnetization [43, 44]. One of them, XY-4 sequence also was used in tests of our setup. In XY-4 sequence, the phase of rf pulses are similar to CPMG sequence, except the fact, that every second π pulse as a $-x$ phase:

$$\frac{\pi}{2}_x - \tau - \pi_y - 2\tau - \pi_x - 2\tau - \pi_y - 2\tau - \pi_x - 2\tau - ... \tag{3.19}$$

It was shown previously by Gullion [43] that XY-4 sequence is an improved CP sequence.

It should be noticed, that another solution for making CP sequences more stable is using composite rf pulses [45] which compensate for non-uniform B_1 field over the sample. For low fields and our setup these composite pulses are hard to implement, especially when a fast sequence is needed.

3.2.2 Gradient Echo (GE) sequence

A gradient echo sequence with bipolar gradients consist of an initial rf pulse that tips the magnetization to a transverse plane and following series of bipolar gradients. A schematic drawing of the sequence is shown in Figure 3.2. The first gradient pulse dephases the local transverse magnetization components and other gradient pulses refocuse them back and forth in order to have a gradient echo centered in the middle of each gradient pulse. The area of following gradient pulses is twice as the area of initial gradient pulse. The echo time T_{CP} is the same for every gradient pulses. The absence of rf pulses with each repetition makes this sequence a very attractive to use at high repetition rates.

For a bipolar rectangular G_x pulse with durations τ of the positive part and τ_r of the negative part, the signal evolution $S(t)$ can be written as [46]:

$$S(t) = S_0(t)e^{-DG_x^2\left[\frac{t^3}{3\tau_r^2}-\frac{t^2}{2\tau_r}+\frac{t+\tau+\tau_r}{4}\right]}\int_x e^{-i2\pi k_x(t)x}dx \tag{3.20}$$

where k_x is the x component of the $\vec{k}$ vector

$$\vec{k}(t') \equiv \frac{\gamma}{2\pi}\int_0^{t'} \vec{G}(\tau)d\tau \tag{3.21}$$

Presence of a diffusion motion yields an exponential attenuation of gradient echo amplitudes. Attenuation rate depends on the gradient strength and echo time T_{CP}. Attenuation rate $T_{2,diff}^{-1}$ measured by GE sequence can be written as:

$$\frac{1}{T_{2,diff}} = \frac{1}{12}\kappa^2\gamma^2DG^2T_{CP}^3 \tag{3.22}$$

However, a total magnetization is not preserved during the sequence time as in CP sequences. If initial rf pulse is an exact $\pi/2$ pulse, the magnetization is tipped to a transverse plane and decays rapidly with a characteristic time T_2^* due to a static field inhomogeneity. Also, GE sequence is sensitive to imperfect shimming currents. Any drift of shimming currents distorts the balance between set of positive and negative gradient pulses, gradient echoes become non-centered. Necessity of using high gradient pulses limits the range of applied gradient pulses values at ultra low magnetic field due to the effect of concomitant gradients discussed in Section 2.2.8.

3.2.3 Advantages of multiple echo experiments

An application of multiple echo experiments allows to obtain information in the most rational way in HP gas experiments. Since the magnetization in HP gas experiments is not renewable, multiple echo sequences increase accuracy of the measurements, which is important in the cases of limited SNR. Echo train allows 1D mapping of diffusion-induced attenuation along the direction of the applied gradient. In one single experiment it is possible to estimate whether uniform diffusion prevails or heterogeneous diffusion conditions play significant role in the sample. Uniform diffusion yield uniform local magnetization decay, then a global exponential decay of the echo amplitudes describes by equations 3.25. Heterogeneous diffusion can occur, for instance, due to a variety of pore sizes if the gas is inside the porous media, or reduced effective diffusion near the sample walls. Both situations can potentially lead to non-exponential decays of echo amplitude. Standard methods can be used to analyze observed decays and create distributions of an apparent diffusion coefficient in the samples with heterogeneous structure. In this work, results of feasibility experiments performed to explore the potential of these methods at ultra low field, in particular in preserved lungs (Section 4.3.5), are reported.

3.3 Data analysis

Experimental data obtained by any used pulse sequence (CPMG, GE) represents a train of acquired echoes. This data was processed by in-house software according to the following algorithm:

1. Cut out the data points in the beginning of the echo that corresponds to a saturation effect (if they are present).

2. Application of a window function to each echo in time domain. This step is important for low gradient experiments and experiments with no applied gradients due to a fact that echoes are very long in time domain, much longer than an echo time of the sequence T_{CP}, and therefore are significantly clipped (only the central part with a time shorter than T_{CP} is present). Such data clipping is identical to a data multiplication on a step function that leads to a convolution with sinc function after the FFT. To reduce an effect of echo FFT distortion, a proper window function is applied to a data in time domain. In this work, alternative window function to a Hanning window suggested by [47] was used. The used function contains cosine

function of higher order and is given below:

$$w(\frac{k}{M/2}) = 2\cos\left(\frac{k\pi}{M+1}\right) - \cos^2\left(\frac{k\pi}{M+1}\right) \tag{3.23}$$

3. FFT of each echo. Fourier transform provides a 1D projection image of the sample along the axis of applied gradient pulses for each echo in the train.

4. Attenuation rate T_2^{-1} extract.

   The solution of the Bloch equation for transverse magnetization 3.2 can be written as

   $$M_{xy}(t) = M_{xy}(0)\exp(-\frac{t}{T_2}) \tag{3.24}$$

   Diffusion attenuation rate can be obtained by fit a mono exponential function fit [7] of the echo amplitudes decay:

   $$S(t) = Y_0 + A\exp(-\frac{t}{T_2}) \tag{3.25}$$

   where Y_0 corresponds to an observed noise level.

   Point by point analysis of amplitude decays in frequency domain leaves a possibility to obtain regional values of ADC, for the cases when SNR is high enough. For not optimal SNR values global ADC values can be computed.

5. However, instead of a standard approximation of echo amplitudes using equation 3.25, fitting of the amplitude squares were made by equation 3.26.

   $$S^2(t) = A_0 + A^2\exp(-\frac{t}{\frac{T_2}{2}}) \tag{3.26}$$

   where A_0 corresponds to an observed noise level.

   The T_2 relaxation time were obtained from the equation 3.26. In all fits parameter A_0 was chosen as free. Potential advantages of this method were described in [48].

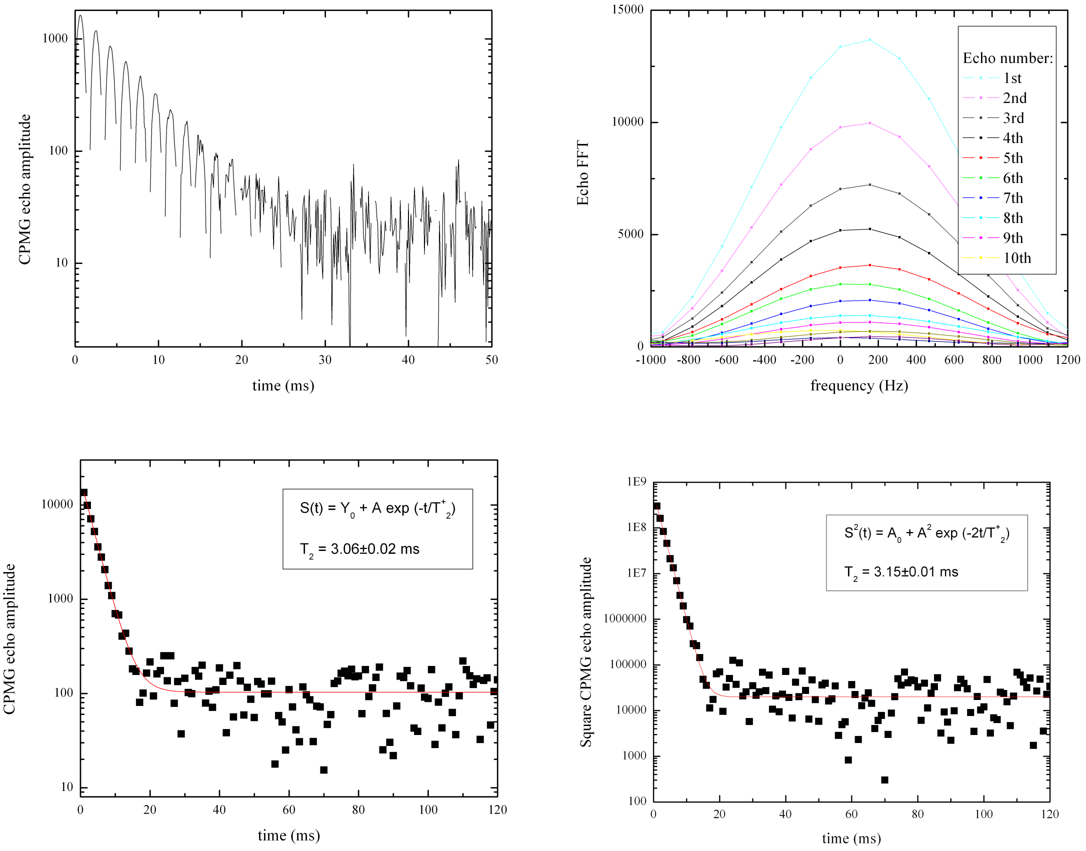

Figure 3.3: Analysis of CPMG or GE data step by step. (a) echo train in time domain (raw data) , (b) FT of each echo, (c) echo amplitudes decay fitted by 3.25, (d) square echo amplitudes decay fitted by 3.26

This method provides more weight during approximation to data points with high signal values than to data points with low signal values or a noise. This increases its precision for a low SNR case (of order 5÷100 [48]). In our diffusion experiments SNR varies from 10 to 1000, that makes fitting the amplitude squares very reasonable.

3.4 Three diffusion regimes

The unrestricted diffusion attenuation of the echo amplitude in a uniform constant gradient G of a magnetic field can be described by a Hahn equation [49]:

$$\frac{M(G,\tau)}{M(0,\tau)} = \exp(-\frac{2}{3}D_0\gamma^2G^2\tau^3) \tag{3.27}$$

if spin echo appears at time 2τ.

This equation corresponds to a so called 'free diffusion' regime. When nuclei are in the condition of a restricted geometry the diffusion can depart from it. One usually defines two main regimes that are isolated from the free diffusion regime: 'motional averaging' and 'localization' regimes [50–52]. These three diffusion regimes can be simply distinguished by comparison of 3 length parameters:

1. The characteristic size l_S for a given geometry, which is usually taken for convenience as the radius R of a spherical pore or tube, or the half-length L of a cylinder tube, depending on an applied field gradient direction.

$$l_S = R \tag{3.28}$$

$$l_S = L/2 \tag{3.29}$$

2. The diffusion length l_D, or the average distance that a spin diffuses during the time τ of an applied gradient along its direction. It is well known that for one-dimensional case, a spin diffuses during the time τ on a distance $\sqrt{2D_0\tau}$. For simplicity, usually diffusion length is set as a $l_D = \sqrt{D\tau}$ [50, 51] where $\tau = T_{CP}/2$ of the CP or GE experimental sequences. But in some works initial original diffusion length $\sqrt{2D_0\tau}$

is used [52]. It is not important for a definition of a concrete diffusion regime, however, correction of diffusion length on $\sqrt{2}$ should be considered for a careful comparison of the results obtained by different groups.

3. The dephasing length l_δ, or a measure of typical length over which spin dephases on 2π [50]. Usually it is taken as

$$l_G = \left(\frac{D_0}{\gamma G}\right)^{\frac{1}{3}} \tag{3.30}$$

An easy way to determine or predict the diffusion regime in the given system approximately is to compare corresponding characteristical lengths in asymptotic case.

3.4.1 Free diffusion regime

1. Free diffusion regime. $l_G \gg l_D, l_s \gg l_D$

Diffusion length is shorter than a structural length and a dephasing length. The spins do not 'feel' the borders of a structure as they diffuse on a much shorter distance during the gradient pulse time. In this regime, spin echo amplitude decays by Hahn's expression [50].

$$\frac{M(G,\tau)}{M(0,\tau)} = \exp\left\{-\frac{2}{3}D_0\gamma^2G^2\tau^3\right\} = \exp\left\{-\frac{2}{3}\left(\frac{l_D}{l_G}\right)^6\right\} \tag{3.31}$$

3.4.2 Localization regime

2. Localization regime. $l_D \gg l_G, l_S \gg l_G$

Dephasing length is shorter than a distance, over which spin diffuses. That leads to a total dephasing of the spins across a volume of the sample. In other words, signal is not uniform within a pore anymore and a total signal from all the spins of a pore is quickly decaying as spins become refocusing. Only near the walls, where diffusion is restricted, an effect of dephasing is reduced and signal from these spins becomes a dominating part of a total signal from a whole sample volume.

It was shown by De Swiet et al. [53], that in this regime echo amplitude decays as

$$\frac{M(G,\tau)}{M(0,\tau)} = c\frac{D_0^{1/3}}{\gamma^{1/3}G^{1/3}l_s}\exp\left\{-a_1 D_0^{1/3}\gamma^{2/3}G^{2/3}\tau\right\} = c\frac{l_G}{l_s}\exp\left\{-a_1\left(\frac{l_D}{l_G}\right)^2\right\} \tag{3.32}$$

, where a_1 is the first zero of the derivative of the Airy function and c is the prefactor that depends on the exact geometry of the sample [50].

It is logical, that in MRI experiments under 'localization' regime strong effect of the edge enhancement should be observed as soon as the majority of signal comes from spins near the walls. Demonstration of the edge enhancement effect is reported in [54, 55].

3.4.3 Motional averaging

3. Motional averaging. $l_D \gg l_S, l_G \gg l_S$

Diffusion and dephasing lengths are much longer than a structural length, the spins during the gradient pulse time have a lot of collision with a pore walls and the diffusion of each spin is restricted in a small volume. In this regime all the inhomogeneities of magnetic field are averaged. Decay of an echo amplitude depends on the type of pores geometry, and for simple cases follows an expression found out by Robertson [56]:

$$\frac{M(G,\tau)}{M(0,\tau)} = \exp\left\{-\frac{1}{120}\frac{\gamma^2G^2l_S^4 2\tau}{D_0}\right\} = \exp\left\{-\frac{1}{60}\left(\frac{l_D}{l_G}\right)^2\left(\frac{l_S}{l_G}\right)^4\right\} \tag{3.33}$$

3.4.4 Diffusion diagrams

All above mentioned diffusion regimes are illustrated on a diffusion diagram shown in Figure 3.4.

The 'borders' or crossovers between these regimes are not very well defined. Exploration of the crossover regions of the diffusion diagram is very challenging from the theoretical point of view. Diffusion condition that can be met in lung airways are lying between free diffusion (trachea) and motional averaging regime (alveoli): the sizes of pores vary from centimeters to hundreds of micrometers. Figure 3.5 shows the typical regimes of lung HP gas MRI experiments. Points are computed for the ^{3}He gas at 1 bar and ^{3}He-N$_2$ mixtures for human lung airways dimensions [57] and typical values of gradients and timings used in MRI [6, 58].

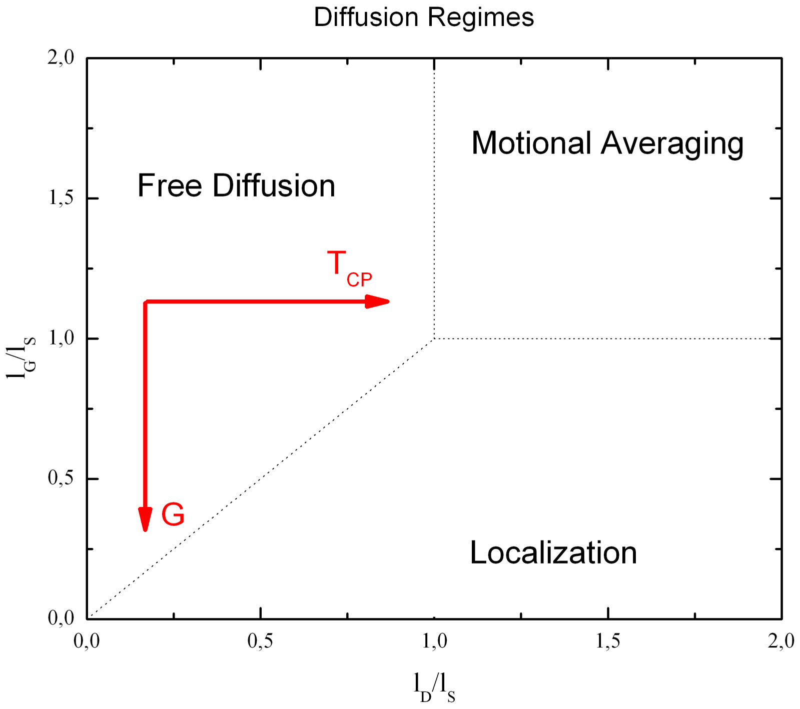

Figure 3.4: Diagram of the diffusion regimes in relative units of l_G/l_S and l_D/l_S. Arrows show direction of the diffusion condition changes with increasing of gradient strength G and echo time T_{CP} of the sequences

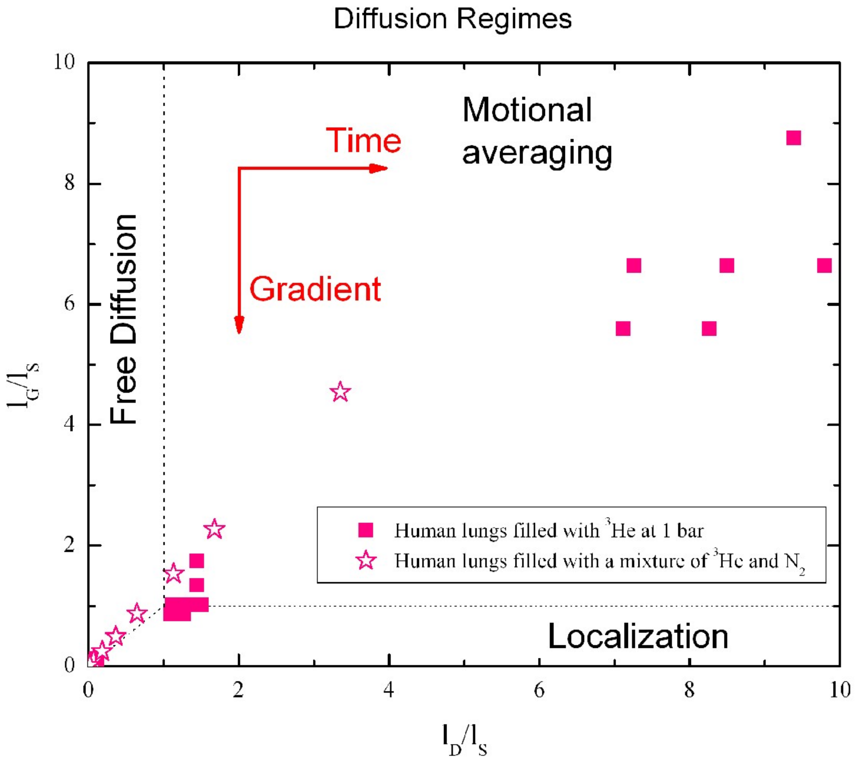

Figure 3.5: Diagram of the diffusion regimes typical for human lungs HP gas MRI. Solid square points correspond to the ^{3}He gas at 1 bar and open stars for the ^{3}He-N$_2$ mixtures. Diagram is plotted in relative units of l_G/l_S and l_D/l_S. Arrows show direction of the diffusion condition changes with increasing of gradient strength G and echo time T_{CP} of the sequences

It must be noticed that from the definition of the diffusion length l_D it is clearly seen: there is a significant dependence on a duration and on an amplitude of the gradient pulse. By changing the gradient value and timing it is possible to explore the diffusion diagram along vertical or horizontal axis. It is especially important for the crossover regimes, when you can browse the diffusion diagram, for example from free diffusion to a localization regime, just by increasing the gradient strength. That means, in the same lung airways but under different experimental conditions the gas diffusion regimes can vary significantly. And in general case, in lung MRI experiments spins are under a crossover of different diffusion regimes. This makes them a very important subject to study experimentally, as soon as there is no valuable diffusion theory for crossover regimes.

Another potentially useful approach of the diffusion diagrams can be achieved by plotting it using an imaging resolution δ instead of dephasing length l_G. Resolution of the 1D image can be found as [40]:

$$\delta = \frac{\pi}{\gamma G T_{acq}} \tag{3.34}$$

In multiple echo experiments the acquisition time T_{acq} can not exceed the echo time $T_{acq} \leq T_{CP}$, which is $T_{CP} = 2\tau$ when spins refocus at the time of 2τ. Using the above written definitions of the diffusion and dephasing length, resolution can be found as

$$\delta = \pi \frac{l_G^3}{l_D^2} \tag{3.35}$$

Digram of diffusion regimes in a new relative units δ/l_s and l_D/l_s is shown in Figure 3.6. This figure demonstrates that the better resolution you will try to achieve in the imaging experiments, the deeply you will deviate to a localization regime.

3.4.5 Free diffusion coefficient

Free diffusion coefficient D in a pure ^{3}He gas or mixtures with N_2 gas can be found from the relation given in [7]:

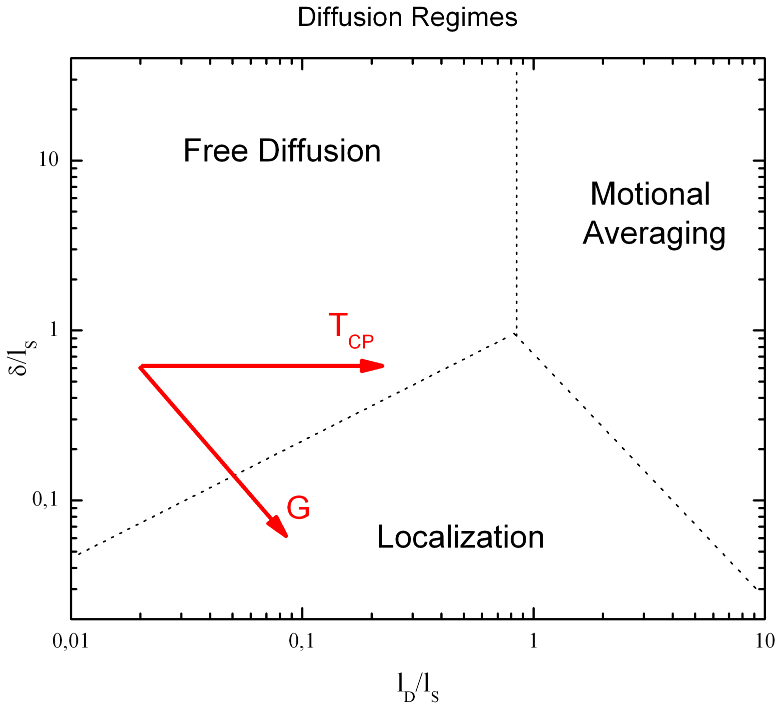

Figure 3.6: Diagram of the diffusion regimes in relative units of δ/l_S and l_D/l_S. Arrows show direction of the diffusion condition changes with increasing of gradient strength G and echo time T_{CP} of the sequences

$$\frac{1}{D} = \frac{P_{He3}}{D_{He3}} + \frac{P_{N2}}{D_{N2}} \tag{3.36}$$

Here P_{He3} and P_{N2} are partial pressures of the ^{3}He and the N_2 gases, and D_{He3}, D_{N2} are reduced diffusion coefficients based on [59] that can be found from simplified equations in $atm\ cm^2/s$ units if the temperature T is in K:

$$D_{He3} = 1.967\left(\frac{T}{300}\right)^{1.71} \tag{3.37}$$

$$D_{N2} = 0.811\left(\frac{T}{300}\right)^{1.65} \tag{3.38}$$

For pure ^{3}He gas free diffusion coefficient is simply

$$D = D_{He3}/P_{He3} \tag{3.39}$$

Free diffusion coefficient was computed using equations 3.36-3.38 for all samples used in this work. The computed results are presented in Table 3.1.

Table 3.1: Calculated free diffusion coefficients D_0 using eq.3.37

Pressure, mbar	**Temperature, K**	D_0, **cm^2/s**
67	298	36.6
70	298	28.2
400	313	5.84
470	298	4.2

3.5 Results and Discussion

3.5.1 Free induction decay

FID experiments were performed for all available ^{3}He cells. Examples of typical NMR signal decays for ^{3}He refillable cells are presented in Figure 3.7. All observed FID signals

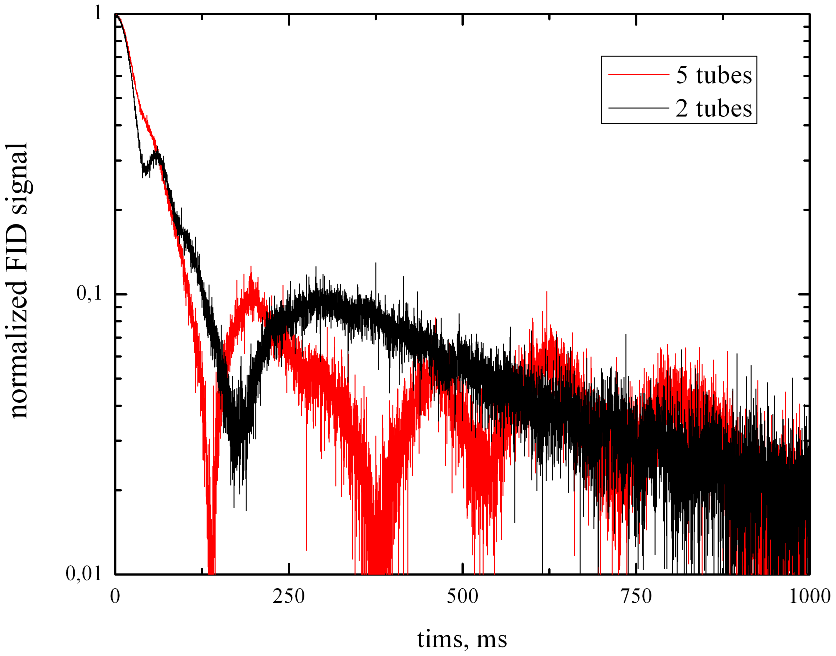

Figure 3.7: Typical FID signals for 470 mbar of ^{3}He gas in sets of 2 and 5 tubes

decay non exponentially. Signal amplitude half-life times are within the range of 30-50 ms, depending on cell dimensions. These time values strictly limit the maximum possible echo time T_{CP} of the gradient echo sequence. Inhomogeneous magnetic field yields in FID signal oscillations with time.

3.5.2 Diffusion in the presence of residual gradients

In CPMG experiments on HP gases without gradient pulses in the perfectly homogeneous magnetic field B_0 echo amplitudes decay exponentially with typical T_2 of order of many hours [41]. But on practice, the static magnetic field B_0 is inhomogeneous. The decay rate increases because of the spins diffusion in a residual gradients and depends on the echo time T_{CP}. For $T_{CP} \to 0$, the relaxation rate should tend to an inherent spin-spin relaxation rate and $T_2 \to T_{2,inh}$. Of course, it is only true for a CPMG sequences with perfect rf pulses. Imperfect rf pulses at fast repetition rates will lead to a an increase of echo decay rate at $T_{CP} \to 0$ when effect of diffusion in residual gradients become negligible.

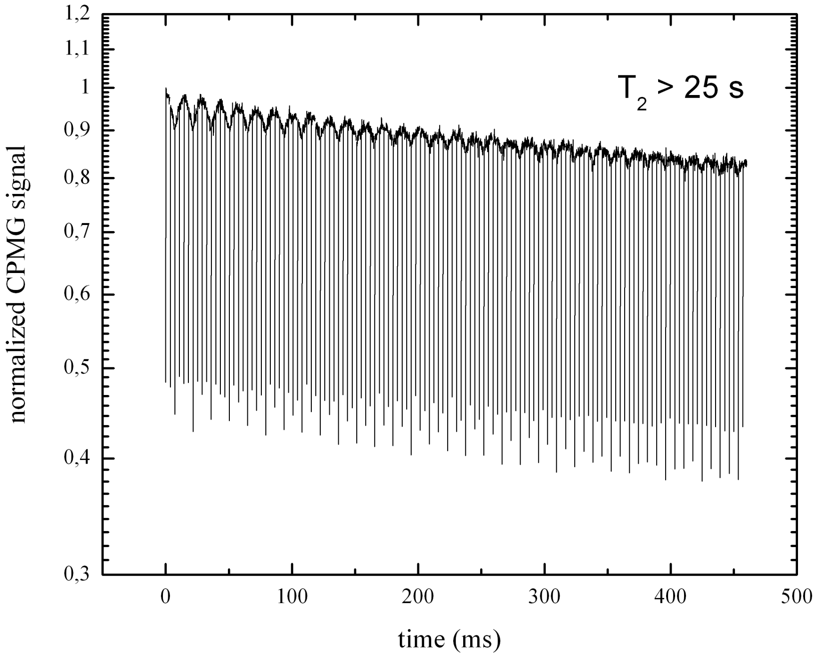

Figure 3.8: CPMG signal for sealed 400 mbar ^{3}He cell. No gradients applied

Example of the CPMG echo trains for 2 different T_{CP} values are shown in Figure 3.8. Experiments were done on the 400 mbar cylindrical cell (12 cm x 1.8 cm). Some instability and oscillations of echo amplitudes are present due to imperfect π pulses. As it can be seen, the decay is mono exponential and is slower than the free induction decay. Obtained data was analyzed by the algorithm described in Section 3.3. Measured T_2 values were at least 25 s for $T_{CP} = 3.4$ ms and 41 s for $T_{CP} = 8.5$ ms. Faster signal decay for sequence with shorter repetition time also can be explained by more frequent application of imperfect π pulses.

Relaxation of the global transverse magnetization due to an external field inhomogeneity is a dominating relaxation mechanism in these experiments. A comparably slow decay rate ($T_2 = 25\ s \gg ms$) in residual gradients can be neglected in the further analysis of the diffusion in measured data.

3.5.3 Diffusion rates $T_{2,diff}^{-1}$

3.5.3.1 CPMG experiments

Variations of the echo time T_{CP} of the CPMG sequence in a high range of values allows to explore regimes with long T_{CP} and low gradients G, i.e., to use a potential advantage of low field NMR - long observation times. Observation times in CPMG experiments are longer than in GE experiments. Used CPMG sequence parameters are given in Table 3.2. All available (four) cell types were used in the experiments. Gradient pulses were varied within a wide range of values and limits of our setup. Gradient pulses were applied in two directions: G_Z - along the cell symmetry axis and B_0 field, G_X - perpendicular to the cell symmetry axis. Experiments were performed at $B_0 \approx 2.7$ mT and the Larmor frequency $f_0 \approx 85.4$ kHz. Duration of the hard π pulse was $\tau_\pi = 0.4$ ms. Experimental datasets were acquired by different hardware units and detection coils. For cylindrical 67 mbar cell standard Ametek 7270 lock-in and homemade hardware, and the set of detection coils **A** were used. The same hardware, but detection coils **B** were used for experiments with 400 mbar cylindrical cell. In experiments with 400 mbar cylindrical cell the temperature controlled holder was used to prevent temperature nonreproductivity during experiment (strong rf discharge heating during polarization process change the cell temperature). Gas in the sealed cells was polarized on site using MEOP technique and polarization reached 4% for 67 mbar cell and 1% for 400 mbar cell. NMR signal from set of 2 and 5 tubes was obtained by detection coils **C** with an active feedback circuit and Apollo console. Cells were refilled after each pulse sequence with polarized gas from the storage cell (MEOP polarizer outside of the setup was used) in these experiments. The initial gas polarization was up to 40%. Gas pressure was controlled by pressuremeter and varied by ±5 mbar from acquisition to acquisition.

In our diffusion experiments we used a variety of cylindrical glass cells with different diameters and lengths and gas pressures. Variation of the gradient direction and of the HP gas pressure allows to explore a huge range of the diffusion conditions that can be met in a different part of the lungs starting from the bronchi and finishing up to an acinar level (Figure 4.30). Gradient timings and amplitudes were chosen to use a maximum potential of the ultra low-field setup by exploring the crossover regimes and be able to

Table 3.2: GPMG sequences parameters used for various ^{3}He cells

Cell type		**^{3}He gas pressure, mbar**	**Gradients, mT/m**		**T_{CP}, ms**
			G_X	G_Z	
sealed	cylinder, 5cm x 5cm	67	0.33; 0.44; 0.66; 1.44	0.85; 1.13; 1.42	2 - 8
	cylinder, 12cm x 1.8cm	400	0.825; 0.99; 1.34; 1.65; 1.98; 2.31; 2.64		2 - 10
refillable	5 tubes, 5cm x 0.7 cm each	70	0.33; 0.66; 0.99; 1.98; 2.97; 3.96	—	2 - 39
		470	0.33; 0.99; 1.98; 2.97; 3.96; 4.95	1.42; 4.25	2 - 17
	2 tubes, 5cm x 1.1 cm each	70	0.22; 1.98	—	3 - 27
		470	0.33; 3.96	—	2.5 - 25

compare our results with a high field results. Region of explored regimes in these CPMG experiments are presented in Figure 3.9.

It must be noticed that majority of the measurements with all type of used cells correspond to a crossover area between free diffusion and localization regimes. However, series of experiments with sets of 2 and 5 tubes filled with ^{3}He at pressure of 70 mbar scan the regions near the so called 'triple point', where all three diffusion regimes can be mixed up, and crossover regime between motional averaging and localization regimes. In such experimental conditions echo amplitude decay rates are expected to deviate from the one for free diffusion.

Typical diffusion attenuated echo trains are shown in Figures 3.10-3.13. All the data were processed by described in Section 3.3 algorithm and equation 3.26. It is very well seen, that echo decays are significantly affected by the diffusion in the field gradients: relaxation time $T_{2,diff} \approx 0.5 \div 250$ ms due to a diffusive motion is much shorter than the inherent time T_2. Deviations from mono exponential decay were not observed in the discussed echo amplitude decay trains in the overwhelming majority of these experiments.

Typical examples of local diffusion rates for all cells are shown in Figures 3.14, 3.15. Relaxation rates have homogeneous values along the major part of the cells. But very close to the cell walls the relaxation rate is lower. Taking a sum of local echo amplitudes or their square values allows to measure a global diffusion coefficient for each cell.

According to the analyzed data values of the signal to noise ratio were within the range of $10 \div 10^3$, depending on a ^{3}He gas pressure. Obtained diffusion decay rates $T_{2,diff}^{-1}$ are plotted against a function of $\kappa^2\gamma^2G^2T_{CP}^2$ in Figures 3.16-3.18 for all the samples. Any straight line with this abscissa axis corresponds to the free diffusion regime. Correspond-

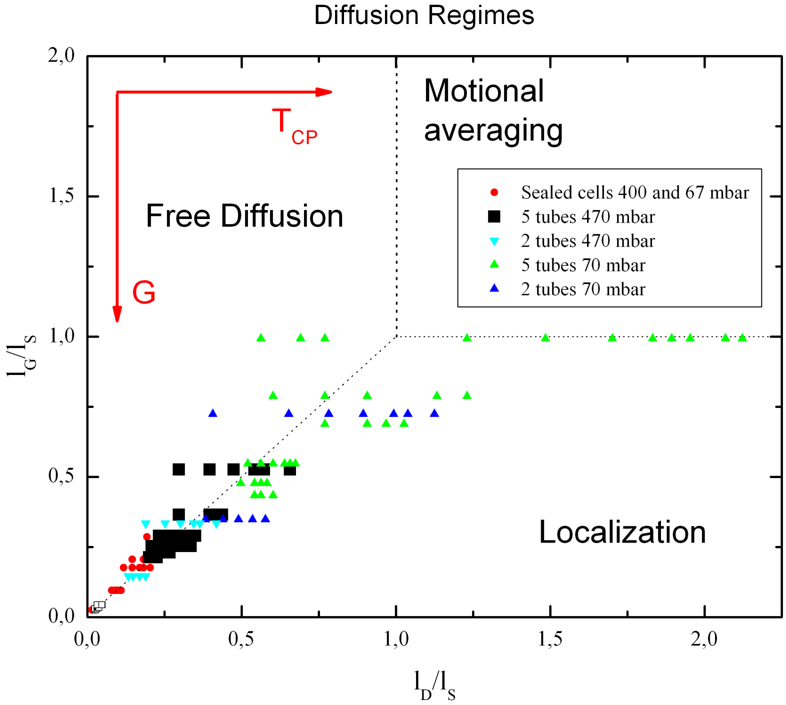

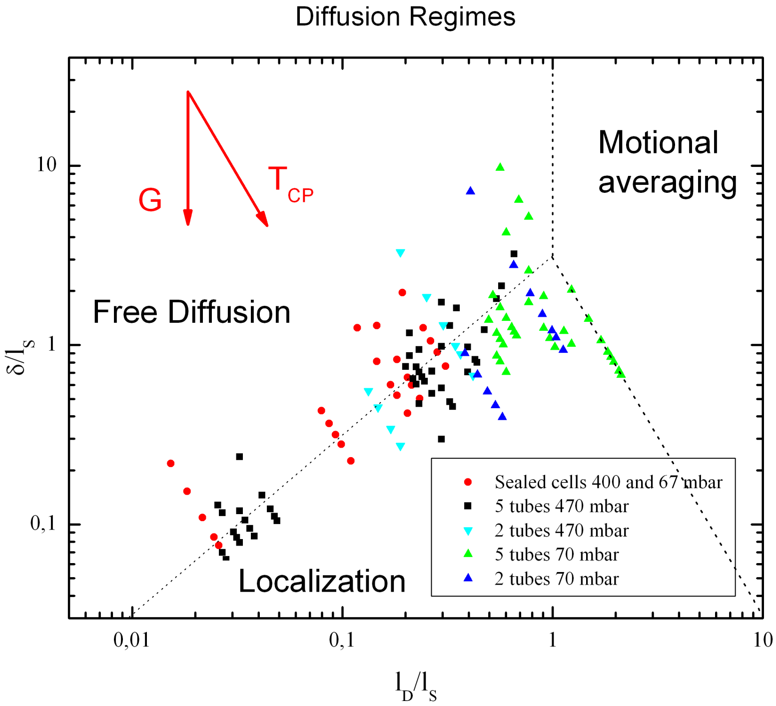

Figure 3.9: Diagram of the diffusion regimes in our diffusion CPMG experiments in relative units of l_G/l_S and l_D/l_S (top plot), δ/l_S and l_D/l_S (bottom plot)

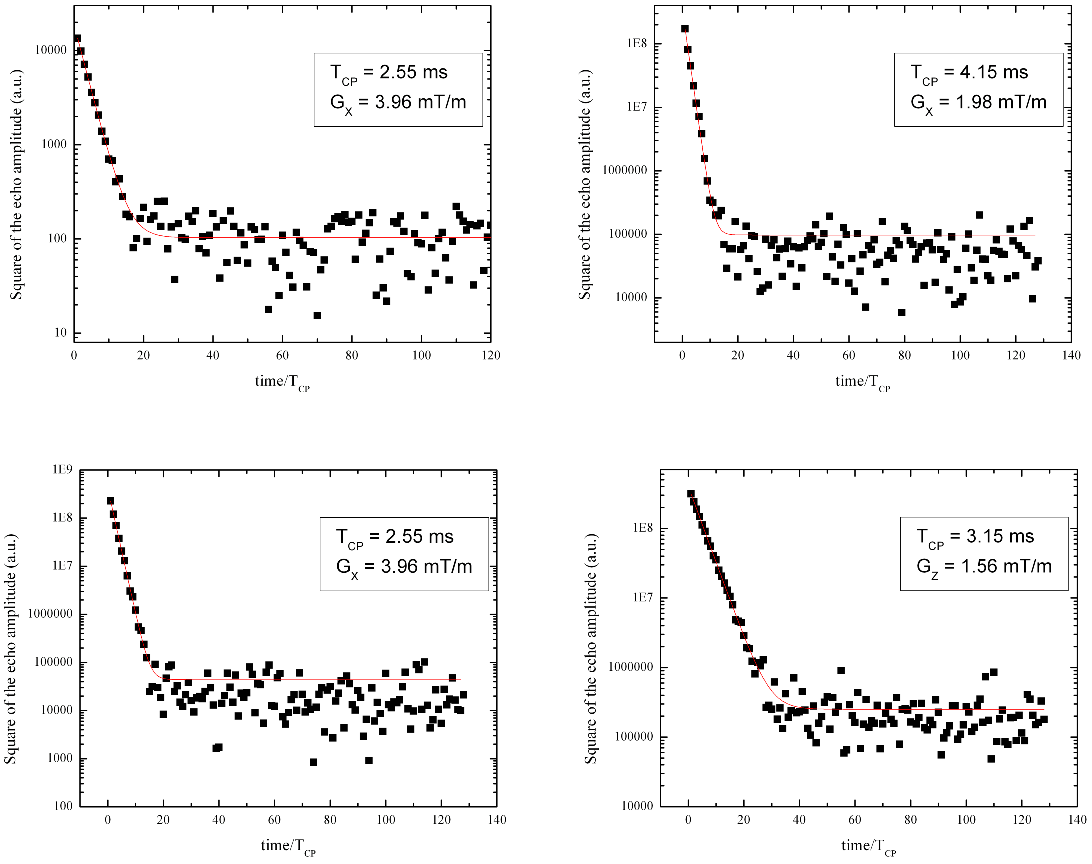

Figure 3.10: Typical echo amplitude decay trains in our CPMG experiments for 2 tubes (top plots) and 5 tubes (bottom plots) filled with ^{3}He gas at 470 mbar. Gradients are given in mT/m. Echo decay train is fitted by eq.3.26

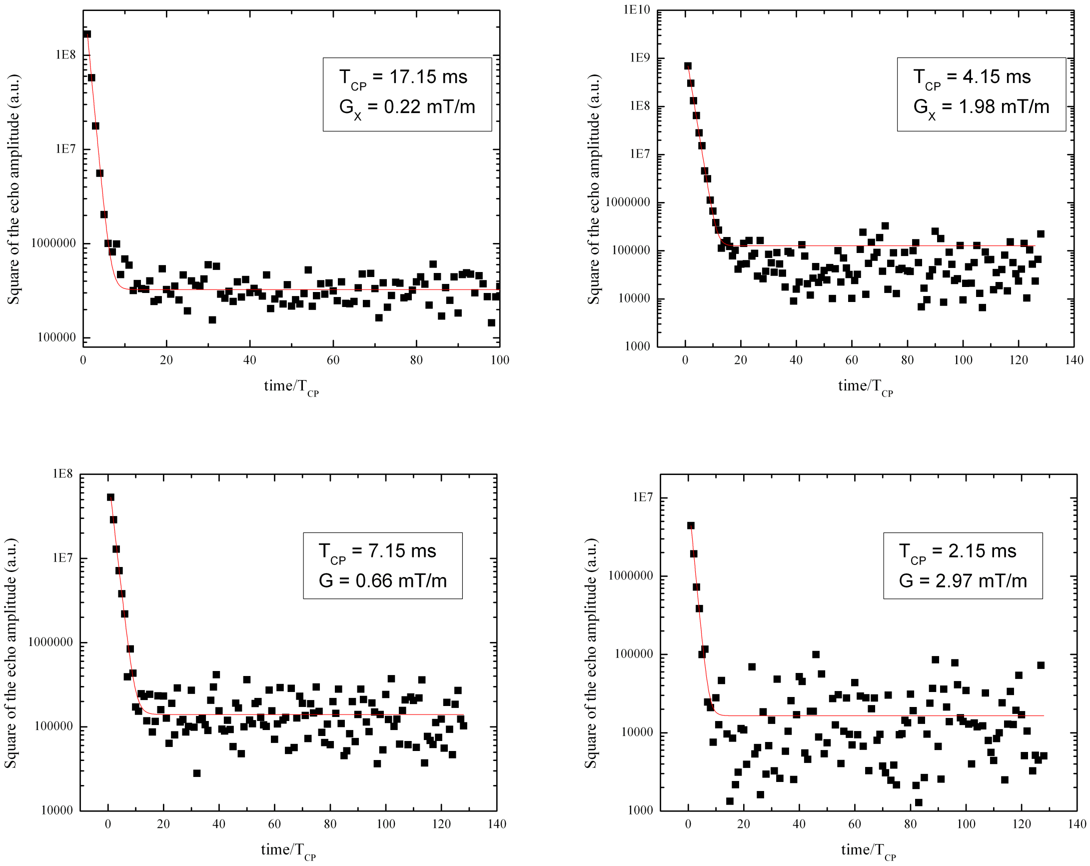

Figure 3.11: Typical echo amplitude decay trains in our CPMG experiments for 2 tubes (top plots) and 5 tubes (bottom plots) filled with ^{3}He gas at 70 mbar. Gradients are given in mT/m. Echo decay train is fitted by eq.3.26

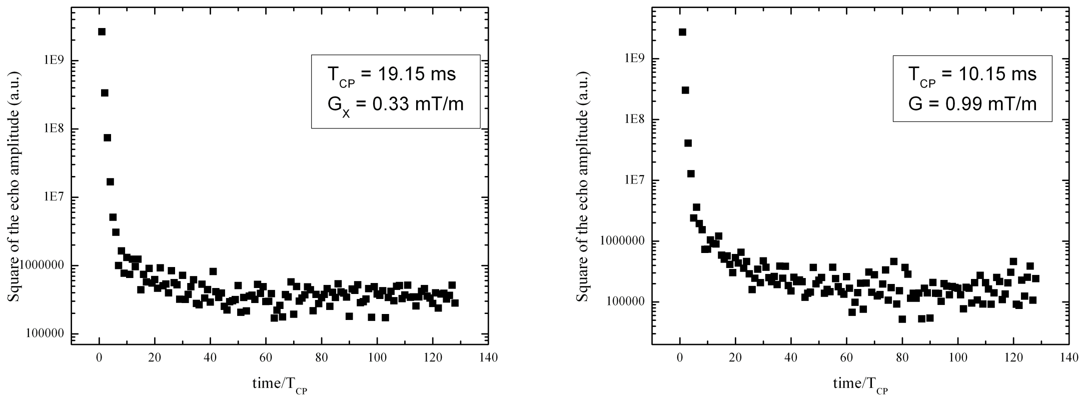

Figure 3.12: Echo amplitude decay trains that cannot be described by a single exponential fit in our CPMG experiments for 2 tubes (left plot) and 5 tubes (right plot) filled with ^{3}He gas at 470 mbar. Gradients are given in mT/m.

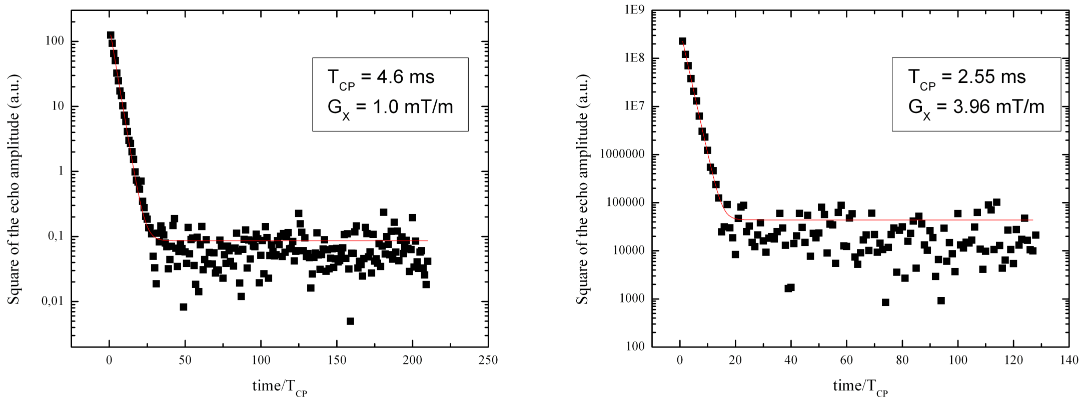

Figure 3.13: Typical echo amplitude decay trains in our CPMG experiments for sealed ^{3}He cells: 67 mbar cell (left plot) and 400 mbar cell (right plot). Gradients are given in mT/m. Echo decay train is fitted by eq.3.26

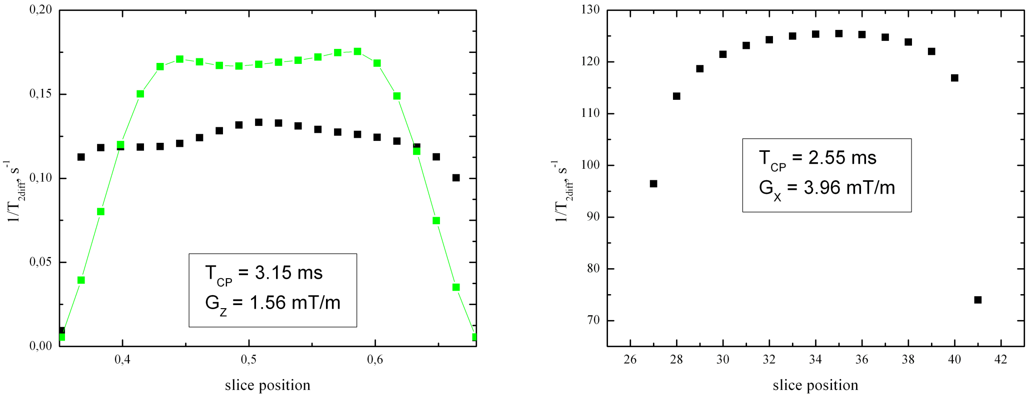

Figure 3.14: Examples of the local distribution of the diffusion rate in the cell along the direction of applied gradient of CPMG sequence for 2 tubes (left plot) and 5 tubes (right plot) filled with ^{3}He gas at 470 mbar. Gradients are given in mT/m. Green line shows 1D image of the sample.

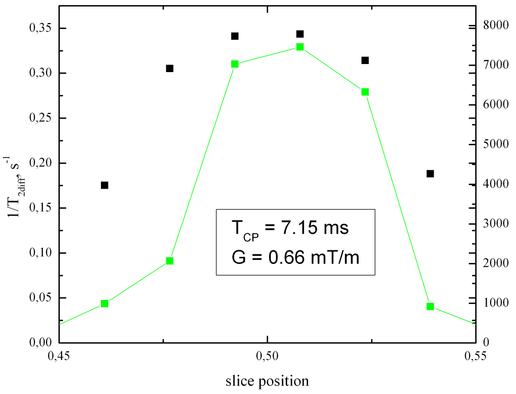

Figure 3.15: Examples of the local distribution of the diffusion rate in the cell along the direction of applied gradient of CPMG sequence for 5 tubes filled with ^{3}He gas at 70 mbar. Gradients are given in mT/m. Green line shows 1D image of the sample.

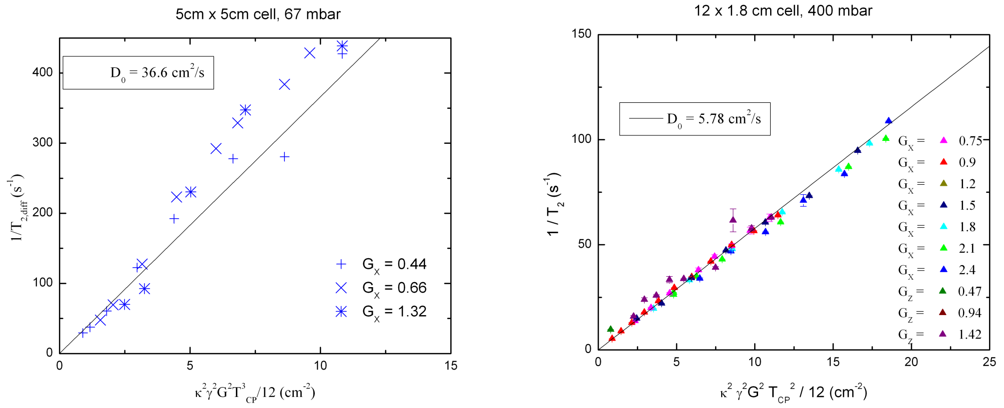

Figure 3.16: Diffusion rates (points) for sealed cylindrical cells 5 cm x 5 cm (left plot) and 12 cm x 1.8 cm (right plot) filled with ^{3}He gas at 67 and 400 mbar respectively. Black solid line corresponds to a diffusion rates of a calculated free diffusion coefficient D_0. Gradients are given in mT/m

ing solid lines for a calculated free diffusion coefficients (Section 3.4.6) are plotted on the same graphs.

All the values of the diffusion rates of gas in 67 and 400 mbar sealed cells are close to expectations for free diffusion and follow the free diffusion line, especially at shorter pulse durations or weaker gradients. Measured diffusion rates from sets of 2 and 5 tubes with high pressure gas are also consistent with ones calculated assuming free diffusion regime. For high T_{CP} values the measured diffusion rates fluctuate around the free diffusion rate but does not show any specific direction. But it can be explained by lower SNR and poor measurement accuracy of these rates. For this experimental parameters any significant departure from the free diffusion regimes is not detected.

The situation is completely different for the gas diffusion rates with both sets of 2 and 5 tubes with 70 mbar ^{3}He pressure. All these rates are plotted in Figure 3.18. Diffusion rates are linear with $\kappa^2\gamma^2G^2T_{CP}^2$ and follow the straight line of the calculated rates only for a very short echo times T_{CP}. In all other cases diffusion rates strongly deviate from the predicted ones of a free diffusion regime. The most interesting point is, that for a given table of experimental parameters, the strongest deviation from the free diffusion is observed for the lowest gradient value $G_X = 0.33$ mT/m. According to the corresponding

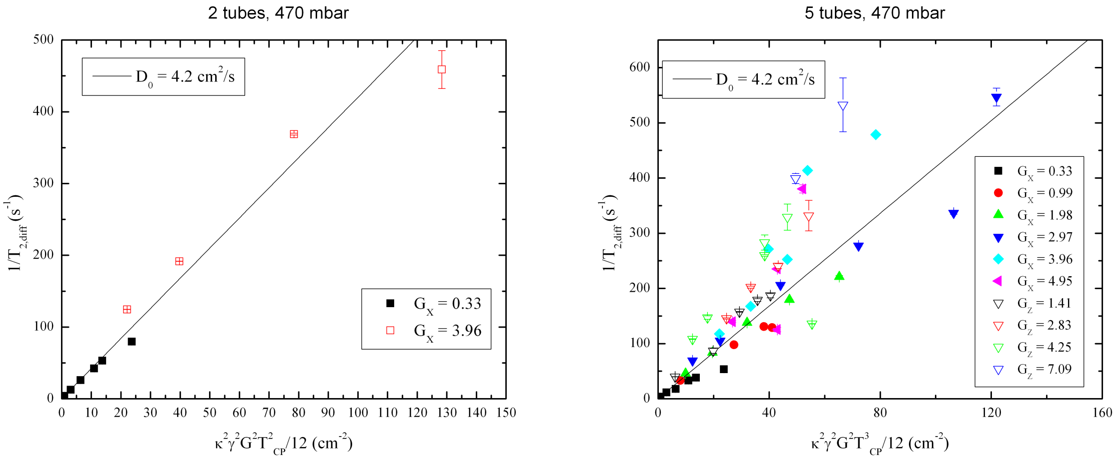

Figure 3.17: Diffusion rates (points) for 2 tubes (left plot) and 5 tubes (right plot) filled with ^{3}He gas at 470 mbar and line of diffusion rates corresponding to a calculated free diffusion coefficient $D_0 = 4.2\ cm^2/s$. Gradients are given in mT/m

points on a diffusion diagram shown in Figure 3.9, the diffusion regime lies in the area between motional averaging and localization.

This results can be interpreted from a point of view using diffusion diagram based on the experimental spatial resolution δ. For the diffusion conditions near 'triple point' an increase of the resolution will result in a strong departure from the expectation of the free diffusion. This fact sets one more reason why experimental parameters must be very carefully checked for a low echo numbered sequences. Results of ADC experiments in assumption of free diffusion regime can become totally incorrect.

Results of CPMG measurements demonstrate that for a certain range of CPMG sequence parameters one is a good instrument for diffusion coefficient measurements.

3.5.3.2 GE experiments

Gradient echo experiments were performed for all cells as well. It was mentioned before, the maximum duration of the echo time T_{CP} for GE sequence was limited to 30 ms by field inhomogeneity. The range of used GE sequence parameters is given in Table 3.3.

Typical trains of gradient echo decays are shown in Figures 3.19 and 3.20. Similar to CPMG experiments, strong attenuation due to a diffusive motion under the field gradients

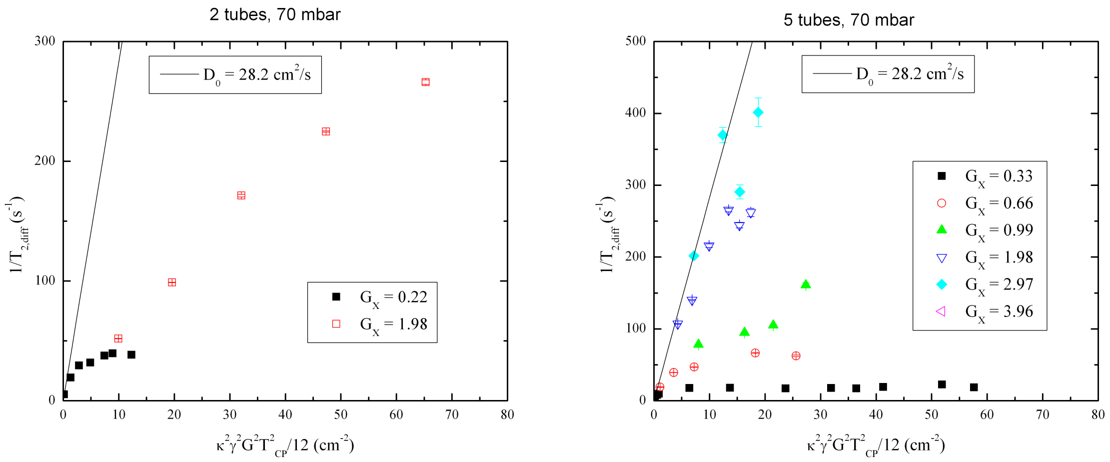

Figure 3.18: Diffusion rates (points) for 2 tubes (left plot) and 5 tubes (right plot) filled with ^{3}He gas at 70 mbar and line of diffusion rates corresponding to a calculated free diffusion coefficient $D_0 = 28.2\ cm^2/s$. Gradients are given in mT/m

Table 3.3: Parameters of used GE sequences

Cell type		**^{3}He gas pressure, mbar**	**Gradients, mT/m**		**T_{CP}, ms**
			G_X	G_Z	
sealed	cylinder, 5cm x 5cm	67	0.96; 1.27; 1.6	0.85; 1.13; 1.42	2 - 9
	cylinder, 12cm x 1.8cm	400	0.99; 1.34; 1.65; 1.98; 2.31; 2.64; 2.97		2 - 9
refillable	5 tubes, 5cm x 0.7 cm each	470	1.98; 2.97; 3.96	—	2.6

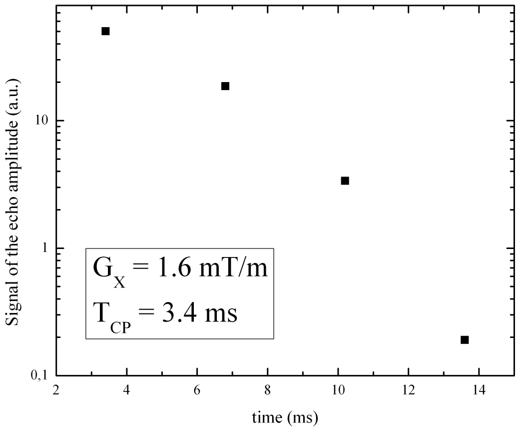

Figure 3.19: Typical echo amplitude decay trains in our GE experiments for sealed ^{3}He cells 67 mbar cell. Gradients are given in mT/m.

is detected. But time evolutions of echo amplitudes have unexpected behavior. In the very first part of the echo train, the decay is not exponential, but is decreasing faster than the exponential one. This effect is very noticeable starting from the 3rd echo of each train.

Despite on the fact that whole GE echo train can not be approximated by an exponential function, diffusion decay rates were obtained from the decay between the first and second echo of measured echo trains. Examples of decay rates for gradient strength up to 1.6 mT/m are shown together with rates found from CPMG experiment for cylindrical sealed cell 5 cm x 5 cm filled with ^{3}He gas at 67 mbar in Figure 3.21.

The obtained echo train attenuation in GE experiments is a product of diffusion-induced attenuation during applied gradient pulses and of signal decay in the inhomogeneous external magnetic field (see Figure 3.7). In order to remove the second contribution to the GE echo decay, the data must be corrected on the signal decay in the inhomogeneous external magnetic field, that can be found from simple FID experiments. Before each experiment the FID signal after tipping on a small angle of $\alpha = 8^0$ degrees was recorded. These recorded data allow to make a correction of the GE experiments data on a signal evaluation caused by an external magnetic field inhomogeneity. Figure 3.22 shows an example of gradient echo train with and without such type of correction. Correction on the FID signal does not change the general echo decay behavior. This type of

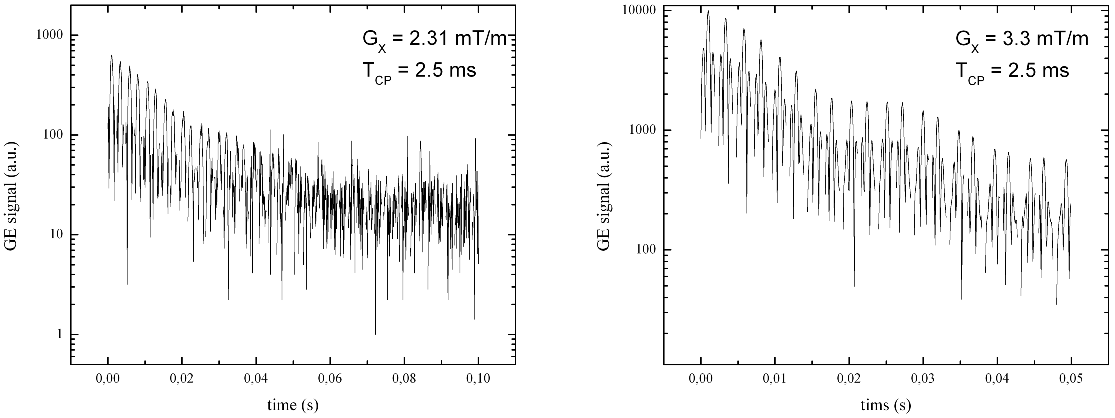

Figure 3.20: Typical echo amplitude decay trains in our GE experiments for set of 2 tubes filled with ^{3}He cells under 470 mbar pressure. Gradients are given in mT/m.

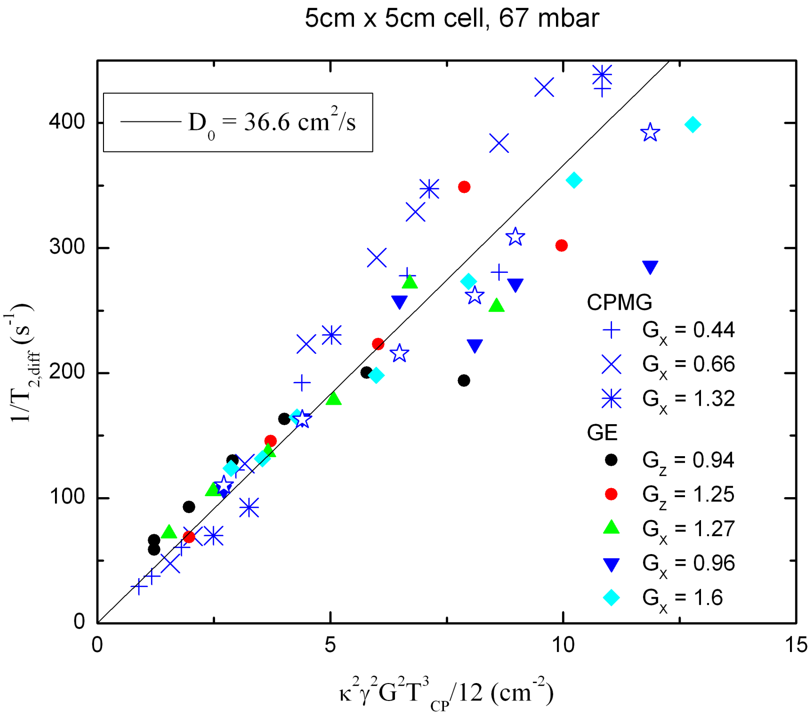

Figure 3.21: Diffusion rates (points) for sealed cylindrical cells 5 cm x 5 cm filled with ^{3}He gas at 67 mbar respectively. Black solid line corresponds to a diffusion rates of a calculated free diffusion coefficient D_0. Gradients are given in mT/m

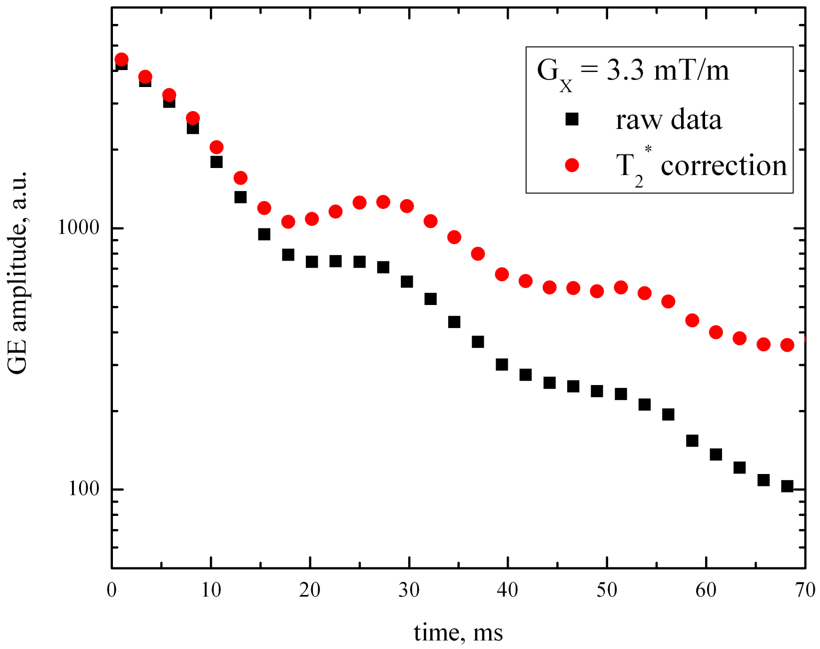

Figure 3.22: Gradient echo decay: raw data (black) and data after correction on the FID signal (red)

a GE echo amplitude decay can not be explained by static field inhomogeneity created by imperfect external magnet.

An explanation of such unexpected GE train decays can be found in the effect of concomitant gradients. Maxwell's equations requires that the divergence and the curl of a static magnetic field are zero. As a consequence, when a gradient coil generate gradient in one direction, concomitant terms arise in the other directions. Presence of concomitant gradients is noticeable especially at low fields and is well known to create artifacts in imaging [38, 60]. The local spin precession axis with angle β to z direction and precession frequencies ω are different for positive and negative gradient pulses [38].

$$\tan\beta_{\pm} = \pm\frac{G_x z}{B_0 \pm G_x x} \tag{3.40}$$

$$\omega_{\pm} = \gamma\left[(B_0 \pm G_x x)^2 + (G_x z)^2\right]^{1/2} \tag{3.41}$$

Spatial distribution of oscillating frequencies and magnetization values appears. This leads to a magnetization imbalance along the sample, i.e. additional losses and different additional attenuation. As a result, gradient echo measurements with bipolar gradients can be seriously affected.

In our experiments, for the set of 5 tubes with 5 cm length, the maximum calculated variations of the Larmor frequency are $\omega_+ \approx 89.49$ kHz for positive gradient and $\omega_- \approx 85.62$ kHz for the negative gradient. The angle of the local magnetization precession axis varies from $\beta_+ \approx 4.14^0$ to $\beta_- \approx 4.33^0$.

Effect of concomitant gradients also depends on the position of the local magnetization from the center: it grows from the center to the edges of the sample.

In all our measurements echo amplitude decay degrading can be noticed after 3rd and 4th echoes. Deviation from exponential decay is a result of cumulative error. Therefore, the same bipolar gradients can be used in imaging sequences with the number of echoes up to 2 - the maximum limit, that ensures the precision of the measurements. Having at least 2 reliable gradient echoes in the imaging sequence is a key point of ADC measurements and diffusion-weighted imaging.

One of the solution to avoid concomitant gradients is using low gradients, but the duration of the echo time T_{CP} is also limited by the T_2^* time. Also at low gradient values, the gradient echoes can be spoiled by the shimming currents that run in the gradient coils. Small deviation of the shimming currents changes the balance of the positive and negative lobes. This leads to shifts of the each echo center. Gradients, created by shimming currents in our setup vary with time within the range of 0.01 mT/m. For CPMG measurements it is not the case, because each echo is created by π pulse that refocuses the magnetization and the small spontaneous changes of shimming currents does not result in echo center shifts.

3.6 Comparison with other works

Several theoretical and experimental investigations on diffusion-induced magnetisation loss and signal attenuation in crossover diffusion regimes have been done by various groups [50, 51, 61], etc. More recently, a detailed study of ^{3}He gas diffusion was performed in cylindrical tubes by GE sequence at 3 T field by Sheffield group [52]. They show in particular that the commonly used “cylindrical model” of [61] is not valid for apparent diffusion coefficient mapping gradient strengths above 15 mT/m. They discuss an updated cylindrical model, show that standard approaches are not valid for localization regimes, and that besides b-value, it is important to include gradient waveforms, their timing and strength for correct data analysis. The other published extensive diffusion study [51] in cylindrical tube (5 cm i.d.) filled with ^3He at 1 torr pressure was performed at 0.6 mT field (with gradients up to 3 mT/m). In this series of experiments the localization regime was avoided, and the observed effective diffusion coefficient was well described by the Bloch-Torrey equations. The results obtained in our diffusion experiments bridge the gap between the very different ranges of parameters of these studies. They provide a large set of data in all diffusion regimes and their crossovers for the future work on validation of existing or new diffusion models that could be used to assess the micro- or macrostructure of lung airways.

3.7 Summary

Various diffusion regimes were explored by CPMG and GE techniques. CPMG sequence provide reliable information about diffusion. Implementation of GE sequences at ultra-low fields is complicated because of the concomitant gradients effect and shimming currents oscillations that significantly limit the range of possible sequence parameters.

Systematic diffusion-induced attenuation measurements in well-defined samples (cylinders in these experiments) have been performed over very wide range of conditions with high SNR using multiple echo and GE schemes. They provide a wide body of data, for direct comparison with existing theoretical models (whenever available: analytical in some limits and numerical) or with some other data. Ultra low field allows for a much wider range of parameters on the low gradient strength and long gradient duration side: there is no susceptibility problem from sample material as at high magnetic fields, and the only limitation comes from inhomogeneity of the static magnetic field. Inhomogeneity can be decreased by construction of a new accurate magnet system. However, measurements are limited on the high gradient side by concomitant gradients effect, especially for GE sequences that require complementary checks of the obtained results by CPMG sequence. In our experiments, similar diffusion conditions to that are met it lung airways (from trachea to bronchi) were reproduced and explored. It was shown, that diffusion regimes for these samples are distributed in the crossover of free diffusion regime, localization and motional averaging. And departure from the free diffusion has a strong dependence for the same sample on the certain experimental parameters as gradient strength and sequence echo time. Precise understanding of signal decays is important for a good control of data treatment and of extraction of apparent diffusion coefficient (ADC) values, which is a delicate and important point in lung MRI where regional ADC mapping has been proposed to be used in order to detect and stage various obstructive pulmonary diseases.

Chapter 4

^{3}He Gas MRI

Diffusion issues in the samples with simplified geometry were considered in previous Chapter 3. After a short theoretical introduction on MRI and imaging sequences, a new imaging sequence is introduced. The proposed sequence benefits from ultra low fields. Theoretical considerations on its advantages at low fields are made. Further experimental validation of the new sequence and its comparison with one of the traditional sequences is made using ^{3}He gas in tubes. Advantages of the new sequence are demonstrated experimentally. Series of obtained 2D images demonstrate the interest of this low field MRI setup. First 2D and 3D images of lungs of a small mammalian are presented. Diffusion maps based on acquired lung images are discussed and compared with preliminary results of a global diffusion measurements made by a CPMG sequence.

4.1 MR signal

Since the evolution of the local magnetization M under typical conditions of MR imaging has been determined in the previous chapter, we can estimate what MR signal $s(t)$ will be created by an ensemble of magnetic moments located in the imaging volume V:

$$s(t) = \int_V M_+(x, y, z)dV \tag{4.1}$$

$$M_+(x, y, z) = M_0(x, y, z)e^{-i\phi(x,y,z,t)} \tag{4.2}$$

$$s(t) = \int_x \int_y \int_z M_0(x, y, z)e^{-i\phi(x,y,z,t)}dxdydz \tag{4.3}$$

$$\phi(x, y, z, t) = \gamma \int_0^t B(x, y, z, \tau)d\tau \tag{4.4}$$

where ϕ is the local phase of spin magnetization with amplitude M_0.

When a rf pulse excites a certain slice of the sample Δz, the MR signal in the presence of the imaging gradient $G_x\vec{x} + G_y\vec{y}$ can be written as [40]:

$$s(t) = \int_x \int_y m_0(x, y)exp\left[-i\gamma \int_0^t (G_x(\tau)x + G_y(\tau)y)\, d\tau\right] dxdy \tag{4.5}$$

$$m_0(x, y) = \int_{z-\frac{\Delta z}{2}}^{z+\frac{\Delta z}{2}} M_0(x, y, \acute{z})e^{-i\phi(x,y,\acute{z},t)}d\acute{z} \tag{4.6}$$

where $m_0(x, y)$ is the magnetization inside the excited slice of the sample with coordinate z and thickness Δz.

Introducing a $\vec{k}$ vector [40] will simplify the solution

$$\vec{k}(\acute{t}) \equiv \gamma \int_0^{\acute{t}} \vec{G}(\tau)d\tau \tag{4.7}$$

$$s_0(t) = \int_x \int_y m_0(x, y)e^{-i2\pi(k_x(t)x+k_y(t)y)}dxdy \tag{4.8}$$

The last equation states that the acquired signal is the 2D Fourier transform (FT) of the spatially distributed magnetization of the sample. The image is the inverse 2D Fourier transform of the acquired signal in the so-called k-space of the k_x and k_y vectors.

$$s(k_x, k_y) = FT(m(x, y)) \tag{4.9}$$

$$m(x, y) = FT^{-1}(s(k_x, k_y)) \tag{4.10}$$

Diffusive motion in ^{3}He gas is rather fast ($D \approx 1.8\ cm^2/s$ for 1 bar at room temperature), thus it is important to consider the effects of diffusion on the MR signal. In the presence of diffusion, during the application of the gradients, the transverse magnetization progressively decays:

$$m_0(x,y) \to m_0(x,y)exp\left[-D\int_0^t \left(k_x^2(\tau)+k_y^2(\tau)\right)d\tau\right] \tag{4.11}$$

$$s(t) = s_0(t)exp\left[-D\int_0^t \left(k_x^2(\tau)+k_y^2(\tau)\right)d\tau\right] \tag{4.12}$$

The latter equation can be simplified after the introduction of the function $b(t)$:

$$b = -\int_0^t \left(k_x^2(\tau)+k_y^2(\tau)\right)d\tau \tag{4.13}$$

$$s(t) = s_0(t)exp\left[-bD\right] \tag{4.14}$$

Also, for the situation where T_2 is short and plays a significant role, the intrinsic relaxation introduces another contribution:

$$m_0(x,y) \to m_0(x,y)e^{-\frac{t}{T_2}} \tag{4.15}$$

A non-renewable total magnetization is a very important feature of HP gas MRI. All the sample longitudinal magnetization will be lost after applying a $\frac{\pi}{2}$ rf pulse. And therefore, a series of small tip angle (α) rf excitations are used in the MRI sequences. If the tipping angle α is constant throughout the whole sequence, the MR signal after n-th rf excitation will be

$$s_n(t) \propto \cos^n\alpha\sin\alpha \tag{4.16}$$

Of course, the latter equation is true only when T_1 relaxation time is long enough and corresponding magnetization decay throughout the sequence are negligible.

4.2 2D MRI in the cells

4.2.1 FLASH sequence

A typical schematics of the FLASH (Fast Low Angle Shot) sequence [62] without slice selection is illustrated in Figure 4.1. After the rf excitation that tips the magnetization

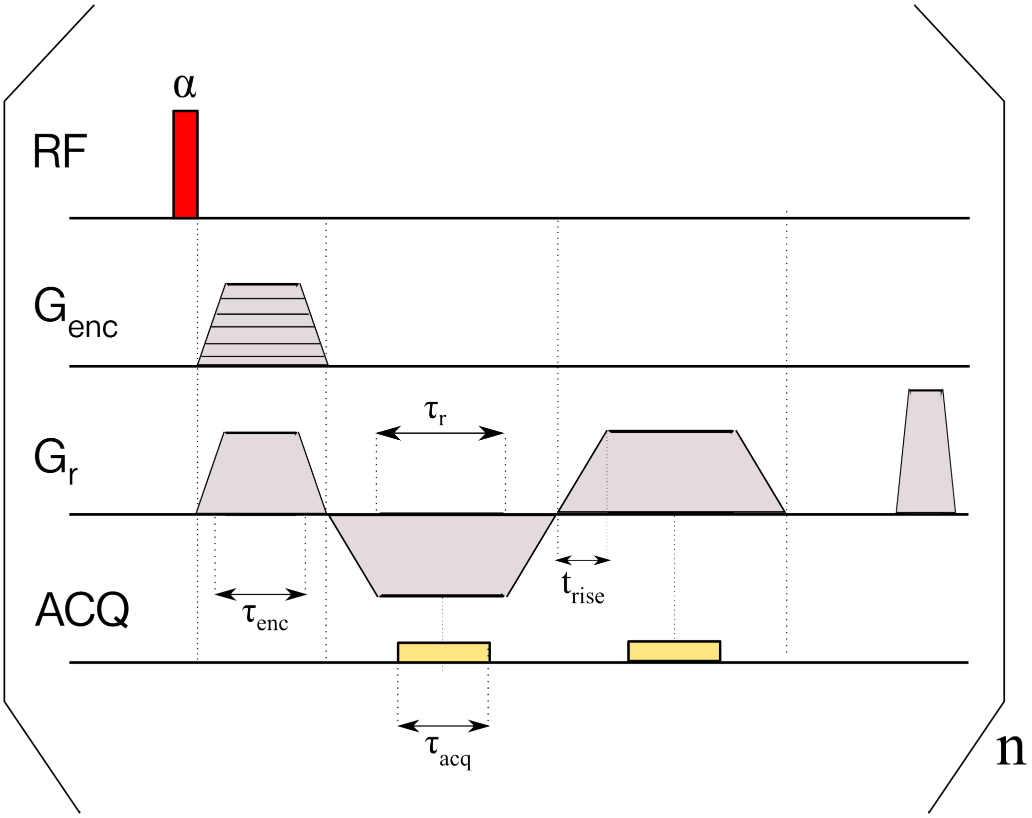

Figure 4.1: Schematics of the FLASH sequence

by an angle α, a phase encoding gradient pulse with amplitude G_{enc} and duration τ_{enc} is applied. Simultaneously, a preparation gradient pulse with amplitude G_r and duration τ_{prep} is applied in the readout direction. Further bipolar gradient pulses with duration τ_r are used to refocus the magnetisation and create echoes. If the area of the preparation pulse is twice smaller than the area of the readout pulse, then the echo will be centered in the middle of readout pulse. In the illustrated case, gradients have trapezoidal shape (with gradient switch time of t_{rise}) and two echoes will be successively created. Data are recorded during the acquisition time τ_{acq}, which satisfies $\tau_{acq} \leq \tau_r$ (due to blanking after gradient pulse switching). After the data acquisition, a strong crusher gradient pulse is applied in the readout direction in order to dephase completely all the spins before the next rf pulse. The value of the phase encoding gradient changes by equal steps of ΔG_e, N_e times with each new scan from the maximum possible G_e value to $-G_e$. Sampling time t_{samp} defines the number of data points acquired per echo N_r: $N_r = \tau_{acq}/t_{samp}$.

The illustrated scheme samples the k-space in a Cartesian way. In Figure 4.2 the

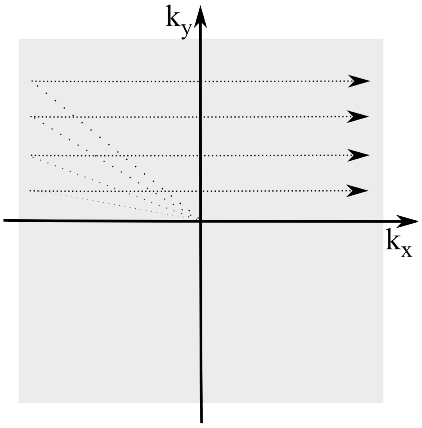

Figure 4.2: Schematics of the filling of the k-space with data using a FLASH sequence

corresponding k-space filling strategy is shown. Each phase encoding gradient pulse G_y moves us in the k-space along k_y axis to a corresponding k-space point. And then readout gradients G_x are scanning the k-space along the k_x direction. After the sequence, the k-space is filled by N_e equidistant sets of N_r points. The total number of the acquired data points $N = N_e N_r$.

In our experiments we used the FLASH sequence (illustrated in Figures 4.1 and 4.2) that samples the k-space by a Cartesian acquisition with double gradient echo. The second gradient echo allowed us to monitor and measure the attenuation induced by diffusion. Gradients and corresponding timings were chosen to have an attenuation between amplitude of 2 echoes by a factor smaller than 2. This condition ensures that the image resolution is not significantly reduced by diffusion. But it also restricts the range of spatial resolutions we can obtain using our setup. The resolution for this sequence is defined below by the equations 4.20 and 4.22 in Section (4.2.3) and it was computed in both readout and phase encode directions for various values of gradients and timings (see Figures 4.3 and 4.4). Families of lines corresponding to a resolution ranging from 1 mm to 5 cm are presented for both k-space directions: read and phase encode. Lines with the same diffusion conditions providing the same amplitude attenuation between two echoes of the sequence are plotted on the same figures. Diffusion-induced echo attenuation is proportional to $\exp(-bD)$, the line of $bD = 1$ that corresponds to attenuation of e times can be plotted for a various gas pressures and temperatures. In Figures 4.3, 4.4 the black line corresponds to condition $bD = 1$ for room temperature and ^{3}He gas at 1 bar pressure. The calculation of diffusion coefficients for ^{3}He gas in glass cells with different gas pressures was made using equation 3.36. These diagrams helps to determine the best possible gradients and timing for desired resolution and diffusion attenuation. The dashed line corresponding to a desired resolution should be picked up and be on the left side of the diffusion line for a given gas pressure: this will allow the diffusion attenuation to be within reasonable boundaries. Of course, some limitations should be taken into account when choosing proper timing and gradients. As soon as the ^{3}He gas pressure is defined, the corresponding diffusion line in the diagram should be picked up. Every point in the diagram on the right of picked diffusion line will represent unsuitable imaging conditions with highly diffusion affected images. The maximum gradient timing is limited by T_2^* and read gradient pulse time τ_r value should be within a reasonable range of times. The maximum available gradient amplitude is a property of each setup and in our case is 5.5 mT/m for X and Y directions , and 9 mT/m for Z direction. However, a minimum possible value of gradient amplitude also can exist, the imaging gradients amplitude should exceed the shimming gradients in order to do not have an affected image.

4.2.2 Signal evolution during rectangular gradient pulses

Since the imaging gradients waveforms are known, it is possible to consider what happens with the signal $s(t)$ when we apply a simple gradient pulse (phase-encoding pulse) and bipolar gradient pulse (readout gradient).

- Phase encoding gradient G_{enc}

  For a rectangular G_{enc} pulse with duration τ_{enc}:

$$s(t) = s_0(t) e^{-\frac{D\gamma^2 G_{enc}^2 \tau_{enc}^3}{3}} \int_y e^{-i2\pi k_y(t) y} dy \tag{4.17}$$

  Diffusion during a phase encoding gradient reduces the amplitude of the signal, but if the application time τ_{enc} is short enough and $\tau_{enc} \ll \left(\frac{3}{D\gamma^2 G^2}\right)^{1/3}$, this attenuation will remain small [46]. In terms of k-space, applying such gradients means mov-

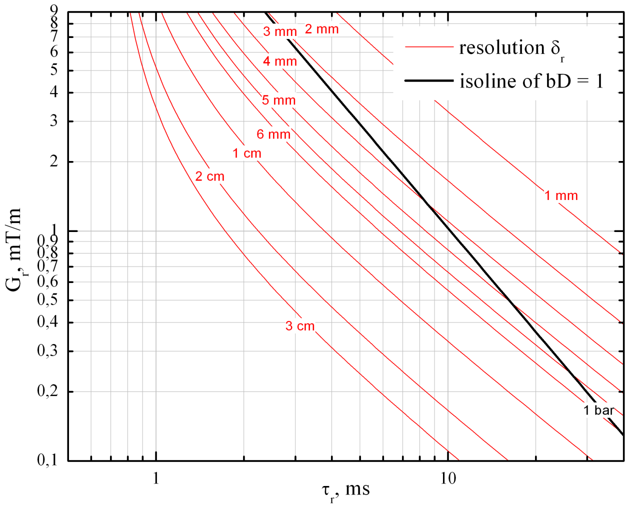

Figure 4.3: Computed resolution for FLASH sequence in readout direction (eq. 4.20) against the gradient strength G_r and timing τ_r. Resolution is represented by a family of dashed lines. Black solid line represents the isoline (same diffusion attenuation) -bD = 1 computed for ^{3}He gas under 1 bar pressure at room temperature

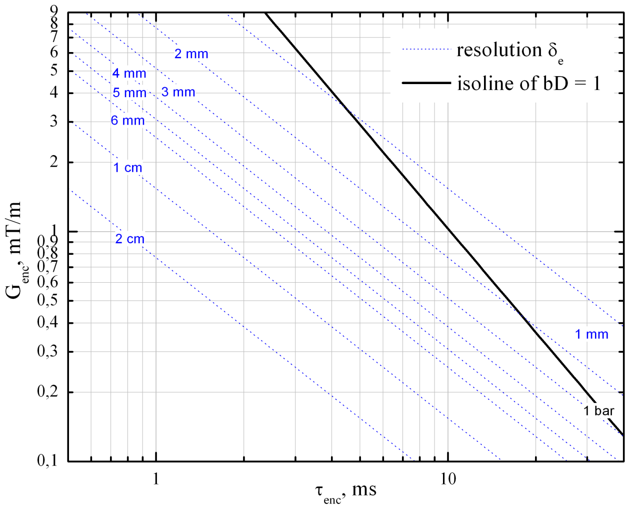

Figure 4.4: Computed resolution for FLASH sequence in phase encode direction (eq. 4.22) against the gradient strength G_{enc} and timing τ_{enc}. Resolution is represented by a family of dashed lines. Black solid line represents the isoline (same diffusion attenuation) -bD = 1 computed for ^{3}He gas under 1 bar pressure at room temperature

ing the position from the center of the k-space along k_y axis to value of k_y that corresponds to the applied gradient G_y.

- Readout gradient G_r

  For a bipolar rectangular G_r pulse with duration τ_{prep} for the first part and τ_r for the second part the signal will be written as:

  $$s(t) = s_0(t) e^{-DG_r^2\left[\frac{t^3}{3\tau_r^2} - \frac{t^2}{2\tau_r} + \frac{t+\tau_r}{4}\right]} e^{-\frac{D\gamma^2 G_r^2 \tau_{prep}^3}{3}} \int_x e^{-i2\pi k_x(t)x} dx \tag{4.18}$$

  Here we can see that attenuation of the signal due to diffusion happens during the whole duration of the readout gradient, hence the signal is attenuated during acquisition. This is a main difference with the phase encoding one. Moreover, for long gradient durations it can significantly reduce the signal amplitude. In terms of k-space, applying a readout gradient means scanning the k-space along k_x axis back and forth, with a direction and velocity depending on the sign and the value of the applied gradient G_x.

  For a trapezoidal bipolar G_r pulse with durations τ_{prep} of the first ('preparation') part, τ_r of the second, and t_{rise} time of each rise and fall lobe [46]:

  $$s(t) = s_0(t) e^{-DG_r^2\left[\frac{t^3}{3\tau_r^2} - \frac{t^2}{2\tau_r} + \frac{t+\tau_{prep}+\tau_r+2t_{rise}}{4}\right]} \int_x e^{-i2\pi k_x(t)x} dx \tag{4.19}$$

  Usually, in our experiments, the durations of the phase-encode pulse and preparation part of the readout pulse were similar $\tau_{prep} = \tau_{enc}$ and were applied simultaneously.

4.2.3 Image Resolution and field of view

If the read direction is x and the phase encode one is y, then the resolution in the read direction Δx can be written as [40]:

$$\Delta x = \frac{2\pi}{\gamma G_x \tau_{acq}} \tag{4.20}$$

The field of view (FOV) is usually defined as the size of the spatial encoding area of the image. With field of view in the readout direction $FOV_r = N_r \Delta x$, so we can write for the resolution in the read direction:

$$\Delta x = \frac{1}{N_r \Delta k_x} = \frac{FOV_x}{N_r} \tag{4.21}$$

In the phase encoding direction, the field of view FOV_e can be presented as $FOV_e = N_e \Delta y$, and we can write

$$\Delta y = \frac{\pi}{\gamma G_y \tau} = \frac{1}{N_e \Delta k_y} = \frac{FOV_e}{N_e} \tag{4.22}$$

Equations 4.20 and 4.22 determine the nominal resolutions Δx and Δy of the image. It should be noticed that, in all our experiments, the observation time τ_{acq} was shorter than the gradient pulse duration τ_r: $\tau_{acq} \leq \tau_r$.

4.2.4 Image SNR

In our experiments no slice selective pulses were applied, so only the case of imaging of the whole volume excitation will be considered. SNR for a voxel with a volume $\Delta x \Delta y \Delta z$ [40]:

$$SNR \propto \Delta x \Delta y \Delta z \sqrt{N_y N_z \tau_{acq}} \tag{4.23}$$

where N_y, N_z are the number of sampling points in the corresponding directions and $\tau_{acq} = N_x t_{samp}$ is the acquisition time, where t_{samp} is the sampling interval of data acquisition.

4.2.5 2D FLASH images

A few 2D projection FLASH experiments of ^{3}He glass cells have been made to verify our considerations about imaging properties, abilities, properties of our setup, and expected diffusion effects. Sets of 2 and 5 tubes were filled with a mixture of HP ^{3}He (500 mbar) and N_2 (500 mbar) gases. Mixture of the gases was prepared in order to decrease the ^{3}He diffusion coefficient and the diffusion attenuation during the readout process. According to equation 3.36, the diffusion coefficient of the ^{3}He in this mixture $D \approx 1.10\ cm^2/s$.

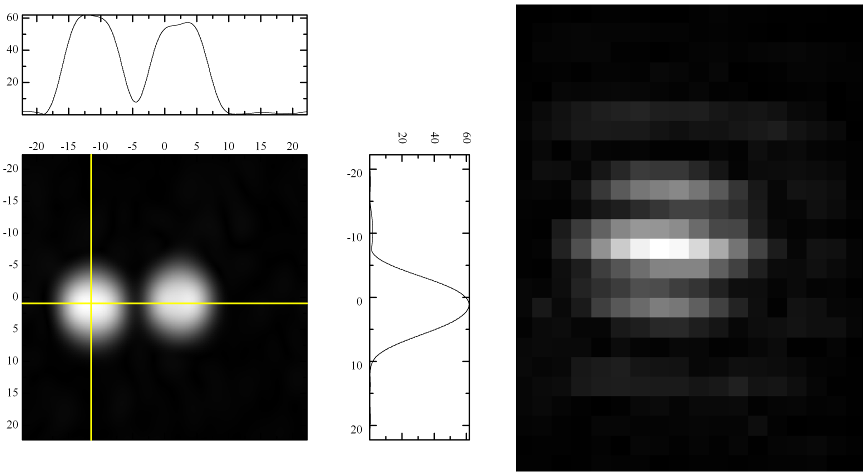

Figure 4.5: A 2D projection FLASH image (left) and the corresponding k-space signal map (right) of the set of 2 tubes filled with the mixture of HP ^{3}He (500 mbar) and N_2 (500 mbar) gases. Plots on the top and on the right to the image represents image profiles along a selected slice (marked by lines on the image). Imaging parameters: $N_e = 24$, $N_r = 18$, $\alpha = 18^o$, $\tau_r = 2.4$ ms, $G_r = 5.25$ mT/m, $\tau_{prep} = 2$ ms, $\tau_{enc} = 2$ ms, $G_e = 3.65$ mT/m, $\Delta_r = 2.5$ mm, $\Delta_{enc} = 1.8$ mm, FOV $= 53$ mm $\times$ 45 mm.

Polarization of the HP gas was up to 40%. 2D images were done in a plane perpendicular to the cells symmetry axis. They are shown in Figures 4.5 and 4.6. Image SNR up to 80 and resolution 2.5 mm were obtained for both samples. The effect of diffusion attenuation can be seen from the comparison of the images from the first and second gradient echoes (Figure 4.7). The amplitude of the second image is two times lower than the amplitude of the first image, which is close to our expectations (Figure 4.3).

4.2.6 SLASH sequence

Signal to noise ratio of the image is proportional to the square root of the acquisition time τ_{acq} (eq. 4.23), and the image resolution in the readout direction is proportional to τ_{acq}^{-1} (eq. 4.20). To increase the SNR, k-space should be scanned as slowly as possible. A slow acquisition strategy imposes certain limitations on the gradient pulses strength and duration (i.e., the sampled k-space dimensions), because the signal amplitude attenuation during read gradient pulse depends on the value of $G_r^2\tau_r^3$ (eq. 4.18). One of

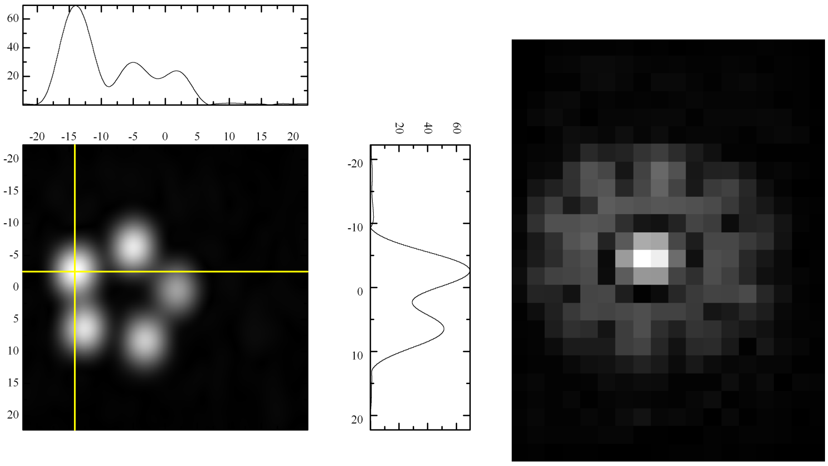

Figure 4.6: A 2D projection FLASH image (left) and the corresponding k-space (right) of the set of 5 tubes filled with the mixture of HP ^{3}He (500 mbar) and N_2 (500 mbar) gases. Plots on the top and on the right to the image represents image profiles along a selected slice (marked by lines on the image). Imaging parameters: N_e = 24, N_r = 18, $\alpha = 18^o$, τ_r = 2.4 ms, G_r = 5.25 mT/m, τ_{prep} = 2 ms, τ_{enc} = 2 ms, G_e = 3.65 mT/m, Δ_r = 2.5 mm, Δ_{enc} = 1.8 mm, FOV = 53 mm × 45 mm.

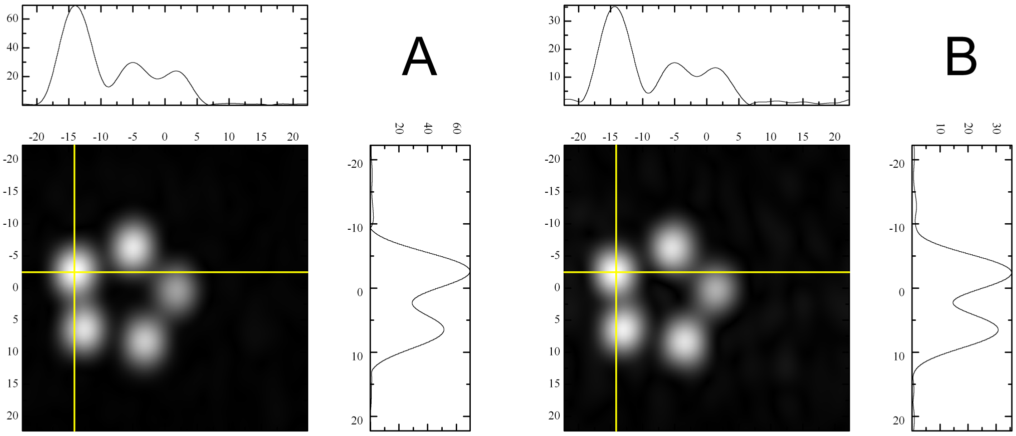

Figure 4.7: A 2D projection FLASH images (A - obtained from the 1st echo, B - from the 2nd echo) of the set of 5 tubes filled with the mixture of HP ^{3}He (500 mbar) and N_2 (500 mbar) gases. Imaging parameters: N_e = 24, N_r = 18, $\alpha = 18^o$, τ_r = 2.4 ms, G_r = 5.25 mT/m, τ_{prep} = 2 ms, τ_{enc} = 2 ms, G_e = 3.65 mT/m, Δ_r = 2.5 mm, Δ_{enc} = 1.8 mm, FOV = 53 mm × 45 mm.

the possible solutions to scan slowly the k-space and preserve desired k-space size (and spatial resolution) is to acquire data in k-space by segments or blocks. Of course, within each block there are still limitations on the gradient pulses values, as well as limitation on the position of the blocks in the k-space and scan direction within the blocks, due to the diffusion induced attenuation. One example of a split k-space sampling with short diffusion attenuation of the signal is presented in Figures 4.8. In this case, the k-space contains 3 rectangular parallel blocks with the same dimensions and scanning direction that are acquired separately (see schematics in the left of Figure 4.8).

Signal attenuation will be considered for set readout time τ_r within each acquired block. Assumption of rectangular gradient pulses is made. If the scan direction is the same for each of 3 blocks and is along k_x axis, then in the central block data samples from $-k_0$ to k_0 (first echo) and then back (second echo). In the left block, from $-3k_0$ to $-k_0$ and then back; in the right block, from k_0 to $3k_0$ and then back. The general idea and purpose of acquisition of the two echoes within each scan will be clarified in Section 4.3.5 that is dedicated to maps of an apparent diffusion coefficient.

During the scan, signal attenuation A is given by following equations:

$$A = exp(-bD) \tag{4.24}$$

$$b = \int_{t1}^{t2} k^2(\tau) d\tau = \frac{k^3}{3\gamma G} |_{k_1}^{k_2} \tag{4.25}$$

For scans within the central block, we will have signal attenuation A_{prep} during the preparation time of read gradient τ_{prep} (travel in k-space from the center $k_x = 0$ to the scan starting point $k_x = -k_0$), then attenuation during scans from $-k_0$ to k_0 and back. Usually in our experiments the preparation time τ_{prep} was equal to the encode time τ_{enc} as it is shown on Figure 4.1. Signal attenuations A_1 and A_2 in the center of both echoes (k_x=0) due to a diffusive motion during a scan can be found from following equations:

$$k_0 = \gamma G_{prep} \tau_{prep} \tag{4.26}$$

$$b_{prep} = k_0^2 \frac{\tau_{prep}}{3} \tag{4.27}$$

$$b_1 = k_0^2 \frac{\tau_r}{6} \tag{4.28}$$

$$b_2 = k_0^2 \frac{\tau_r}{2} \tag{4.29}$$

$$A_1 = e^{-Dk_0^2(\frac{\tau_{prep}}{3}+\frac{\tau_r}{6})} \tag{4.30}$$

$$A_2 = e^{-Dk_0^2(\frac{\tau_{prep}}{3}+\frac{\tau_r}{2})} \tag{4.31}$$

For scans within the right block, b_{prep} will be similar, but signal attenuation A_1 and A_2 in the center of both echoes ($k_x = 2k_0$) according to eq.4.25:

$$b_1 = k_0^2 \frac{\tau_r}{2} \left(\frac{2^3 - 1^3}{3} \right) = 7k_0^2 \frac{\tau_r}{6} \tag{4.32}$$

$$b_2 = 2k_0^2 \frac{\tau_r}{2} \left(\frac{3^3 - 2^3}{3} \right) = 38k_0^2 \frac{\tau_r}{6} \tag{4.33}$$

$$A_1 = e^{-Dk_0^2(\frac{\tau_{prep}}{3}+7\frac{\tau_r}{6})} \tag{4.34}$$

$$A_2 = e^{-Dk_0^2(\frac{\tau_{prep}}{3}+19\frac{\tau_r}{3})} \tag{4.35}$$

For scans within the left block, b_{prep} will be 3^3 times higher, but signal attenuation A_1 and A_2 in the center of both echoes ($k_x = -2k_0$) are the same as for right block:

$$b_1 = k_0^2 \frac{\tau_r}{2} \left(\frac{2^3 - 1^3}{3} \right) = 7k_0^2 \frac{\tau_r}{6} \tag{4.36}$$

$$b_2 = 2k_0^2 \frac{\tau_r}{2} \left(\frac{3^3 - 2^3}{3} \right) = 38k_0^2 \frac{\tau_r}{6} \tag{4.37}$$

$$A_1 = e^{-Dk_0^2(27\frac{\tau_{prep}}{3}+7\frac{\tau_r}{6})} \tag{4.38}$$

$$A_2 = e^{-Dk_0^2(27\frac{\tau_{prep}}{3}+19\frac{\tau_r}{3})} \tag{4.39}$$

Additional signal diffusion attenuation in the presence of the phase-encoding gradient G_y (steps along k_y axis) is the same for all blocks and can be written as

$$k_y = \gamma G_y \tau_e \tag{4.40}$$

$$b_y = k_y^2 \frac{\tau_e}{3} \tag{4.41}$$

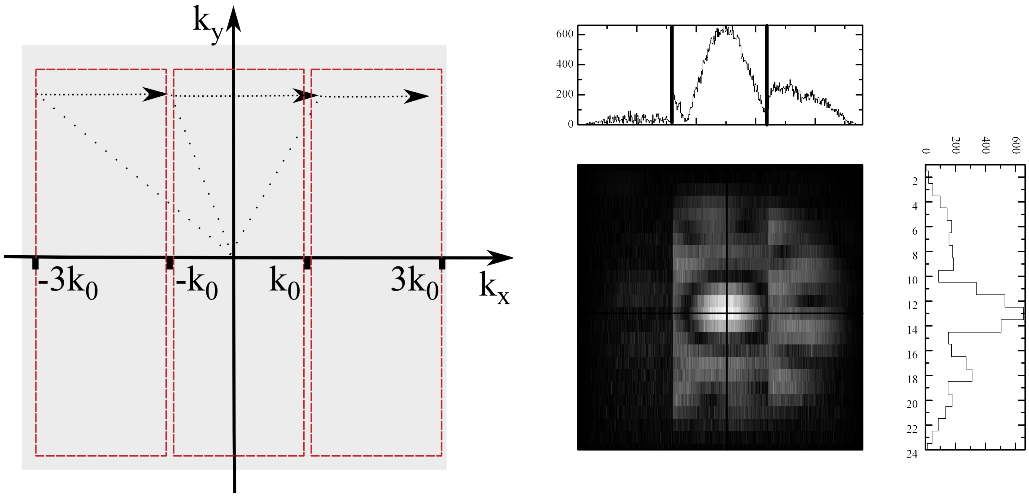

Figure 4.8: The k-space filling strategy with 3 blocks (left) and the experimentally acquired k-space map (right) for a set of 5 tubes filled with ^{3}He gas under 500 mbar pressure. Diffusion attenuation has strong impact on the k-space data.

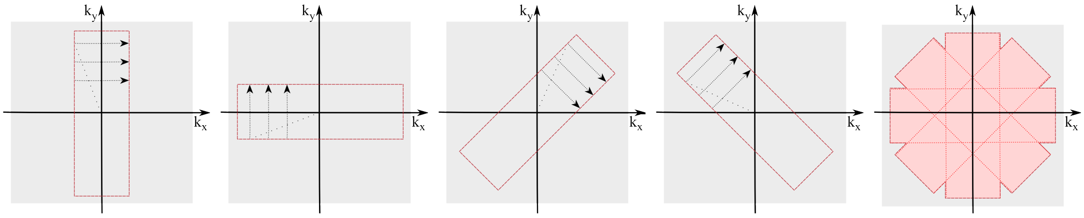

Figure 4.9: Illustration of k-space filling strategy for a SLASH sequence with 4 bands that form a double cross (DC): + and X. The k-space is covered by 4 bands.

Such heterogeneous signal attenuation during the scans and preparation gradient throughout the k-space is confirmed by experiment (right, Figure 4.8) and yields in image artifacts and does not allow to obtain any gain in the SNR or resolution.

The main idea of the Slow Low Angle Shot (SLASH) sequence is to sample the k-space by a series of highly anisotropic bands. Each of these bands is just a usual anisotropic sampling by a FLASH sequence along a given direction.

In our experiments we sampled the k-space with 4 blocks that are called as bands in this manuscript, as it is schematically shown in Figure 4.9. But, in the general case, the number of bands can be higher and is limited only by SNR value during each scan (high number of bands requires higher number of excitations and lower tipping angles). Slow filling of the k-space with 4 or more bands helps to avoid some mentioned above difficulties created by diffusion attenuation of the signal. In the case where diffusion affects the image intensity and resolution during set readout time τ_r using FLASH sequence, SLASH sequence allows to fill the k-space separately by segments with smaller dimensions in the k-space. This strategy increases the range of possible gradient values and timings. For the particular case used in all our experiments, the ratio of resolutions in readout and phase-encode directions $\Delta_r/\Delta_{enc} = 3$. The k-space was filled by four bands with 45 degrees change in orientation between each one, so the k-space was covered by a double cross (DC): one along $\vec{k}_x$, one along $\vec{k}_y$ and the other two rotated by 45 degrees (see Figure 4.9).

The maximum k values will be defined as $k_x^{FLASH} = k_y^{FLASH}$ for a square k-space sampled by FLASH sequence. Each band of the DC SLASH sequence will scan a rectangular segment of the k-space with dimensions k_x^{SLASH} on k_y^{SLASH}, where $k_x^{FLASH} = 3k_x^{SLASH}$ and $k_y^{FLASH} = k_y^{SLASH}$. Signal attenuation will be considered for a set read gradient G_x and timing τ_r for FLASH and DC SLASH sequences.

If the starting point for sampling of each line of k-space is the maximum k_x value, then the signal attenuation during the time τ_{prep} of the gradient pulse G_{prep} for both sequences (eq.4.24)

$$b = \int_{t1}^{t2} k^2(\tau)d\tau = \frac{k^3}{3\gamma G}\,\Big|_{k_1}^{k_2} \tag{4.42}$$

$$b_{prep}^{SLASH} = \left(k_x^{SLASH}\right)^2 \tau_{prep}/3 \tag{4.43}$$

$$b_{prep}^{FLASH} = \left(k_x^{FLASH}\right)^2 \tau_{prep}/3 \tag{4.44}$$

$$b_{prep}^{FLASH} = 27 b_{prep}^{SLASH} \tag{4.45}$$

Values of b_1^{SLASH} at the time of the first echo center ($k_x = 0$) during scan from k_x^{SLASH} to $-k_x^{SLASH}$ with read time τ_r and gradient pulse $G_x = G_r$:

$$b_1^{SLASH} = \left(k_x^{SLASH}\right)^2 \tau_r/6 \tag{4.46}$$

Values of b_2^{SLASH} at the time of the second echo center ($k_x = 0$) during the back scan from $-k_x^{SLASH}$ to k_x^{SLASH}

$$b_2^{SLASH} = \left(k_x^{SLASH}\right)^2 \tau_r/3 \tag{4.47}$$

Diffusion attenuation of the amplitude of the first echo A_1 and the second echo A_2

$$A_1 = e^{-D\left(k_x^{SLASH}\right)^2 \tau_{prep}/3} e^{-D\left(k_x^{SLASH}\right)^2 \tau_r/6} \tag{4.48}$$

$$A_2 = e^{-D\left(k_x^{SLASH}\right)^2 \tau_{prep}/3} e^{-D\left(k_x^{SLASH}\right)^2 \tau_r/2} \tag{4.49}$$

An important consequence that follows these equations is that it is possible to estimate an apparent diffusion coefficient after comparison of amplitudes of two images obtained from the first and the second echo (see Section 4.3.5).

For FLASH sequence, b-values can be written in the same way for scans from k_x^{FLASH} to $-k_x^{FLASH}$ and back $-k_x^{FLASH}$ to k_x^{FLASH}:

$$b_1^{FLASH} = \left(k_x^{FLASH}\right)^2 \tau_r/6 = \left(k_x^{FLASH}\right)^3 /(6\gamma G_x) \tag{4.50}$$

$$b_2^{FLASH} = \left(k_x^{FLASH}\right)^2 \tau_r/3 = \left(k_x^{FLASH}\right)^3 /(3\gamma G_x) \tag{4.51}$$

or

$$b_1^{FLASH} = 3^3 \left(k_x^{SLASH}\right)^3 /(6\gamma G_x) = 27 b_1^{FLASH} \tag{4.52}$$

$$b_2^{FLASH} = 3^3 \left(k_x^{SLASH}\right)^3 /(3\gamma G_x) = 27 b_2^{FLASH} \tag{4.53}$$

Then, for a given G_r and τ_r, difference in the signal attenuation during SLASH and FLASH scans for both echoes can be written as

$$A_1^{FLASH} = \left(A_1^{SLASH}\right)^{26} \tag{4.54}$$

$$A_2^{FLASH} = \left(A_2^{SLASH}\right)^{26} \tag{4.55}$$

Signal attenuation during FLASH sequence can be decreased but it requires shorter gradient timings τ_r and τ_{prep} and stronger gradients G_{prep} and G_r. First of all, these changes can exceed the setup potential and hence be impossible to perform. Second, such shortening of gradient timings decreases the SNR of the image and (for set sampling rate) will result in reduced resolution δ_x. One of the key points of the DC SLASH sequence is that the final image resolution is determined by the resolution in phase-encode direction that depends on the size of the phase-encoding steps and does not depend on the reading parameters τ_r and G_r. For given τ_r and G_r, the SLASH sequence provides better SNR due to lower diffusion-induced attenuation and can provide better resolution than the FLASH sequence. The same considerations can be made for the experiments where we are limited by a short T_2^* in the readout direction: using the same reading time, SLASH sequence allows to use sample the k-space by segments. It means that the SLASH sequence can provide a better resolution than the FLASH one.

In proton MRI flexibility of the imaging sequences is limited in many cases by a very short T_2^* (e.g., in solid state, in porous media, etc.). Images are much more affected by T_2^* than by diffusion. For imaging the systems with short T_2^* times it is possible to use the single-point imaging (SPI) method [63–65], in which it is possible only to acquire one data point per excitation based on FID amplitude in the k-space. This scheme is a phase-encoding technique that operates by acquiring a single data point in the free induction decay (FID) after a fixed delay (phase-encoding time τ_{enc}, that is constant for the whole data set), following the pulsed RF excitation, in the presence of static magnetic field gradients. But at low fields in MRI with HP gas T_2^* is long enough and allows to acquire more data points per each RF excitation. For instance, in our experiments $T_2^* \approx 50\ ms$ due to imperfect B_0 homogeneity. But much longer T_2^* values would be obtained in an improved setup, without significant contributions resulting from the magnetic susceptibility of the sample.

4.2.6.1 SNR

It is well known that central part of the image corresponds to the global shape of the final image, and that data on the edge of the k-space correspond to the finest details of the image [40]. With the DC SLASH sequence the central part of the k-space is scanned 4 times, which increases the SNR of the final image by averaging of the central k-space segment.

DC SLASH requires 4 times a higher number of rf excitations than FLASH as the total number of the phase encoding lines N_e is increased 4 times for a fixed field of view. The non renewable magnetization of the HP gas forces to reduce the tip angle α so as to keep $\cos^{N_e}\alpha$ constant.

$$\cos^{N_e}\alpha \approx 1 - N_e\alpha^2/2 \tag{4.56}$$

$$N_e\alpha^2 = const \tag{4.57}$$

$$SNR \propto \sin\alpha \approx \alpha \tag{4.58}$$

$$\alpha \propto 1/\sqrt{N_e} \tag{4.59}$$

Then, for DC SLASH, the signal is twice lower than for FLASH since $\frac{SNR^{SLASH}}{SNR^{FLASH}} \propto \frac{1}{\sqrt{4}} = \frac{1}{2}$. But averaging of the central part $N_{ave} = 4$ times of the k-space increases the SNR by $SNR^{SLASH}/SNR^{FLASH} \propto \sqrt{N_{ave}} = 2$. In other words, the effect of low tip angle on image SNR is compensated by averaging. We will relate the SLASH acquisition time τ_{acq}^{SLASH} and read gradient strength G_r^{SLASH} to the FLASH acquisition time τ_{acq}^{FLASH} and read gradient strength G_r^{FLASH}. For a similar resolution and diffusion-induced signal attenuation for both sequences, it can be written that

$$G_r^{FLASH}\tau_{acq}^{FLASH} = 3\tau_{acq}^{SLASH}\tau_{acq}^{SLASH} \tag{4.60}$$

$$\left(G_r^{FLASH}\right)^2\left(\tau_{acq}^{FLASH}\right)^3 = \left(G_r^{SLASH}\right)^2\left(\tau_{acq}^{SLASH}\right)^3 \tag{4.61}$$

And the ratio of the acquisition times

$$\tau_{acq}^{SLASH}/\tau_{acq}^{FLASH} = 3^2 \tag{4.62}$$

The image SNR is proportional to the square root of the acquisition time, so

$$SNR^{SLASH}/SNR^{FLASH} \propto \sqrt{\tau_{acq}^{SLASH}/\tau_{acq}^{FLASH}} = 3 \tag{4.63}$$

The image SNR for the SLASH sequence is at least 3 times higher for fixed resolution than for the FLASH sequence.

4.2.6.2 Point spread function

The point-spread function (PSF) provides a way to quantify the blurring of a point object on the obtained image. It depends on the sequence parameters and applied filters. For

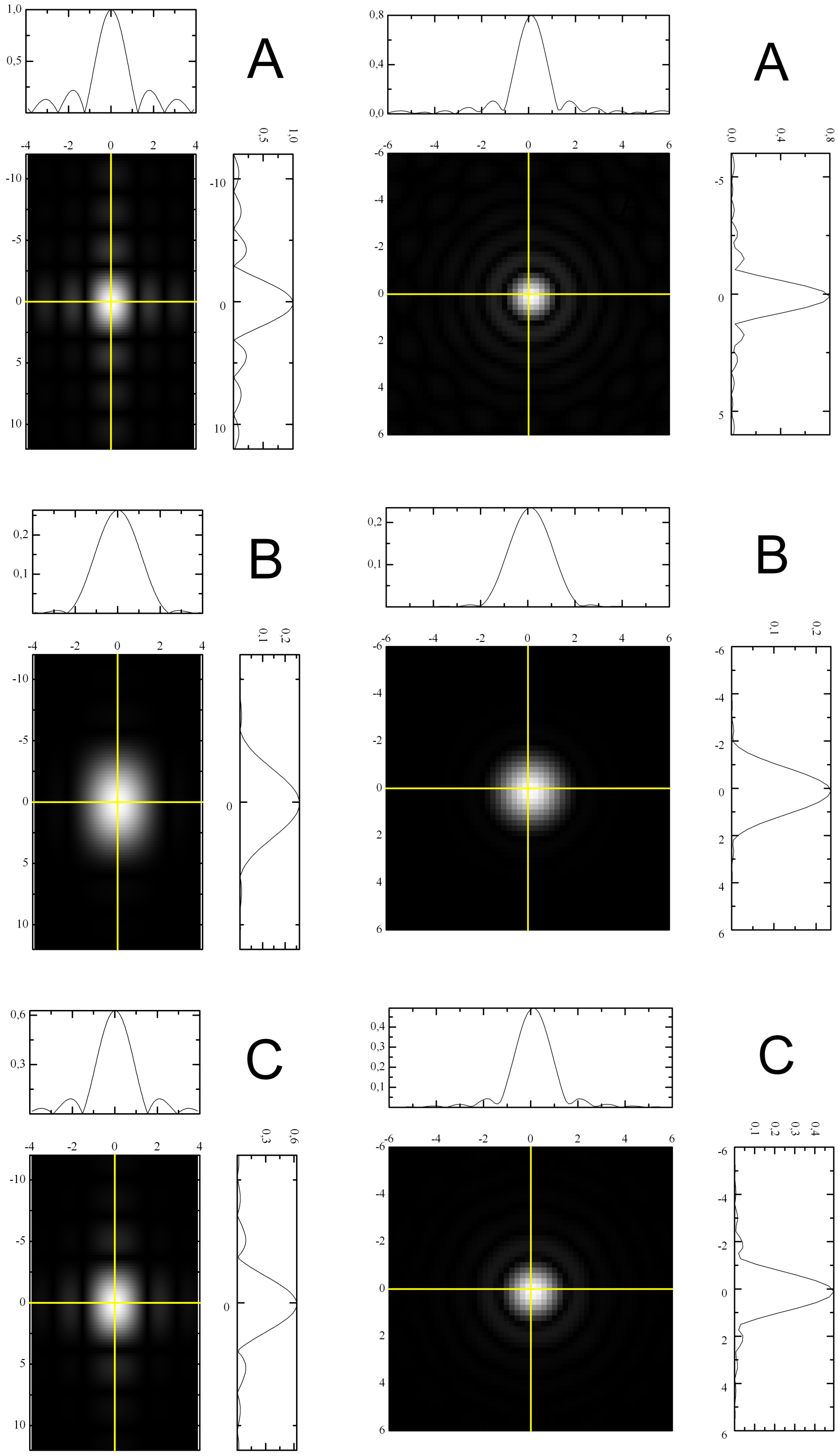

Figure 4.10: Point-spread function with a set of profiles on readout and phase encode directions for the FLASH (left column) and the SLASH (right column) sequences. (A): no apodisation, (B): Hanning window, (C): cosine function of 2nd order window (eq. 3.23). For FLASH sequence readout direction is vertical, phase encode direction is horizontal. Images are given in units of mm.

each imaging sequence, the final image is a convolution of the real image with the PSF corresponding to the sequence and filters.

For a one-point image that can be represented by a Dirac delta function the result of FFT is 1. In other words, k-space data corresponding to a one point image is constant and equal to 1 in any point. To obtain a PSF of the sequences, k-space was filled by ones and then processed using image reconstruction algorithms (detailed discussion in Section 4.2.7). The obtained image distribution is the sought-for point spread function. It must be noted that diffusion is not considered in this method. PSF for FLASH and SLASH computed by this methods are presented in Figure 4.10. The plotted PSF were obtained for various apodisation filters: Hanning window function, HBBR window function (eq.3.23) and without any apodisation. For FLASH sequence, if apodisation function is not applied on the data in k-space, a PSF should represent a sinc function due to the limited dimension of the k-space. Computed PSF without apodisation is a sinc function, as expected. Computed PSF associated with regridding for SLASH is radially isotropic. The PSF does depend on apodisation functions: they allow to reduce long-range oscillations but at the expense of the point blurring.

4.2.7 DC SLASH sequence reconstruction algorithm

4.2.7.1 Data structure

The acquired data are trains of double gradient echoes. Four 'bands' of DC sequence were acquired each one after another, in the following order: 'Vertical', 'Horizontal', 'Diagonal1', 'Diagonal2'. Within each 'band' the phase encoding gradient varies by a given step from $-G_{enc}^{max}$ to a G_{enc}^{max} (variation from $-k_{max}$ to a $+k_{max}$ in the k-space along the corresponding axis). An in-house software separates the initial data in 2 data files, the first file consists of the echo trains corresponding to the first gradient echoes, the second - one of second gradient echoes. These two sets of data are processed separately.

4.2.7.2 Regridding

Before assembling all the data (4 rectangular bands) in k-space, regridding on a square matrix was performed. It is needed because our image data in k-space have rectangular shape for each band. All the bands were regridded separately on a matrix with bigger dimensions. In order to expand each band to the bigger matrix, we must use an interpolation algorithm. Linear interpolation between lines in k-space of each band distorts the image and "moves" some signal outside of the range of interest. It also creates incorrect noise map around the object. Various approximate interpolation methods have been proposed in the literature. Interpolation using sinc function takes into account not only the two neighboring lines, but all the acquired data points. This method removes the artificial artifacts that appear after linear interpolation and preserves as low image distortions as possible for a given detection circuit resonance curve. Applications of the linear and sinc interpolation algorithms in the DC SLASH data processing are illustrated in Figure 4.11. These images show the noise maps acquired by the DC SLASH sequence (only the first band) and then processed by mentioned algorithms. The 1D projections of both noise images are shown on 4.12. Linear interpolation significantly distorts the shape of the noise map, that should have a rectangular shape. In Figure 4.13 results of both interpolation methods on the 2D image of 5 tubes set filled with ^{3}He gas obtained by DC SLASH sequence are presented. The image SNR after interpolation using sinc function is higher than for linear one. Both illustrations clearly shows, that interpolation using sinc function does not distort the image profile. At the same time, linear interpolation corrupts the image, decreases the overall signal amplitude from the sample and creates unexpected signal contribution in areas located outside of the sample. More about regridding using sinc function can be found in [66].

4.2.7.3 Averaging

After regridding pairs of orthogonal bands (vertical+horizontal and the 2 diagonals) are combined in two crosses. Then the two crosses are added up after simple rotation of the diagonal cross by 45 degrees. Since we are using a correction for tipping losses (eq.4.16), the last acquired bands have enhanced noise levels. All bands are thus combined with weighting coefficients that give more weight to the first acquired bands instead of using simple averaging.

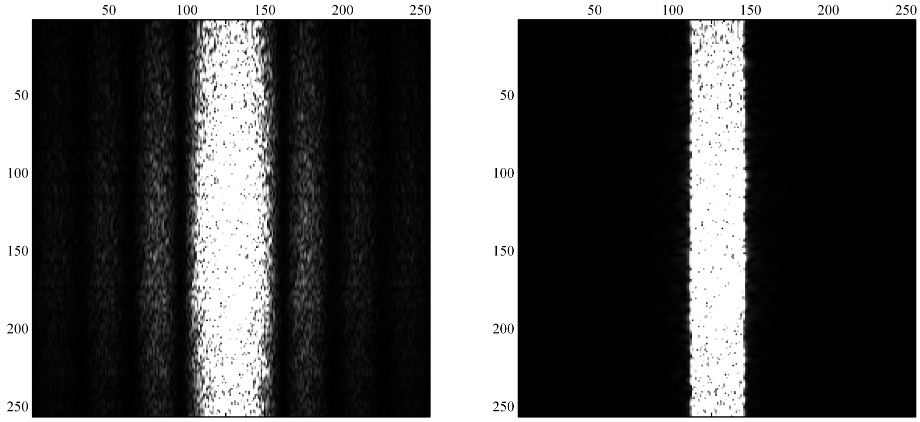

Figure 4.11: Noise map obtained by the first band of the DC SLASH sequence. Interpolations by linear function (left map) and sinc function (right map) were used. Linear interpolation distorts the image profile much more than interpolation with sinc function

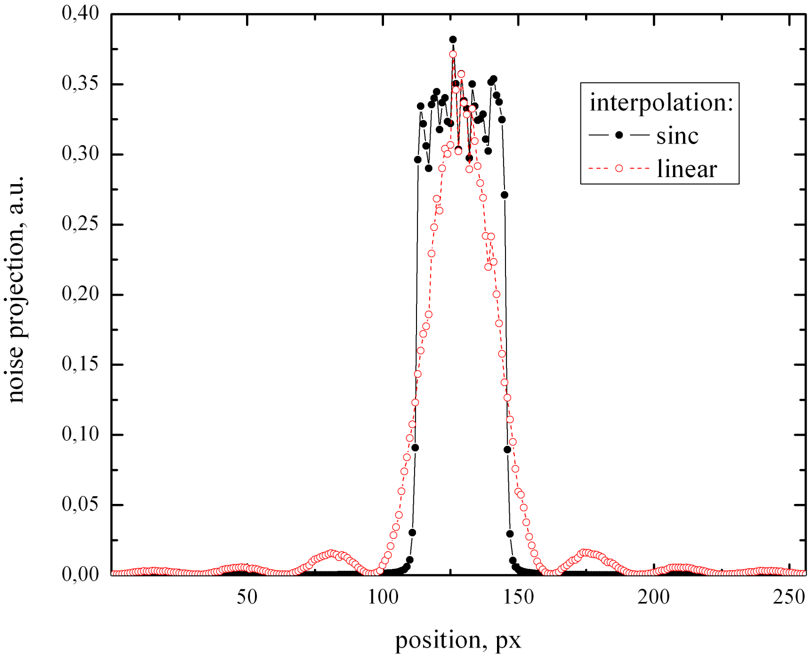

Figure 4.12: 1D projections of the noise maps shown in Figure 4.11. Linear interpolation distorts the image profile much more than interpolation with sinc function

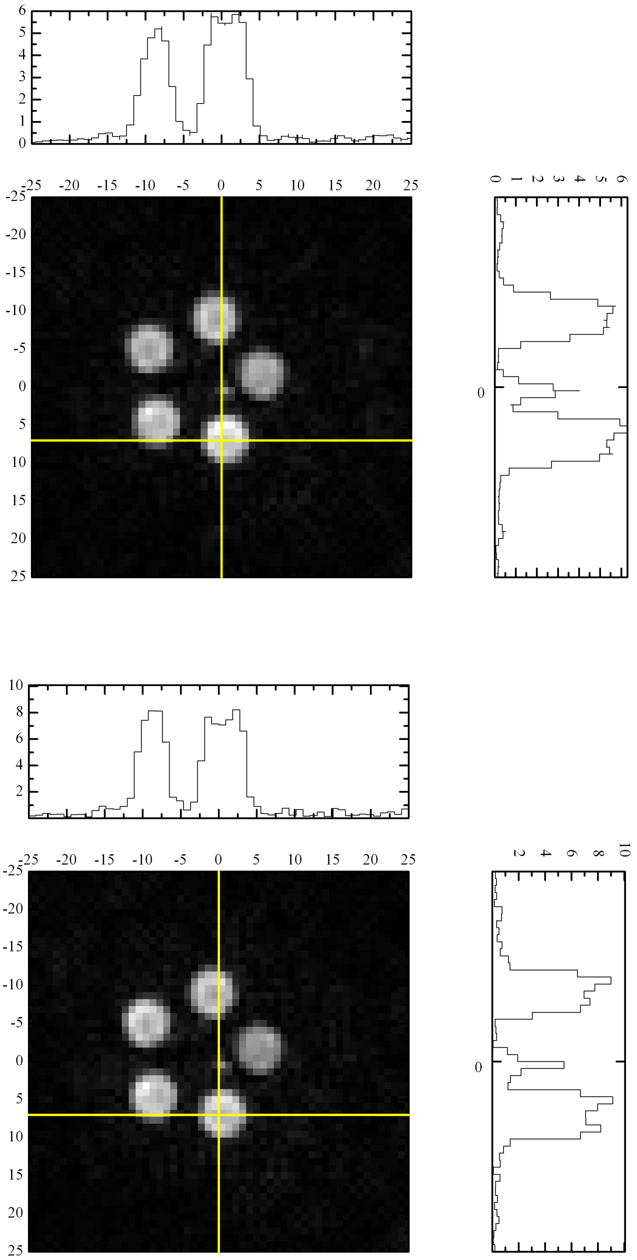

Figure 4.13: Results of obtained using of linear interpolation (top) and sinc interpolation (bottom) on the final images. Images were made on a set of 5 tubes (5 cm long, i.d. 0.7 cm each) were filled with mixture of HP ^{3}He (500 mbar) and N_2 (500 mbar) gases. Image intensity is ≈25% lower for the case of linear interpolation. Imaging parameters: $N_e = 31$, $N_r = 78$, $\alpha = 9^o$, $\tau_r = 9$ ms, $G_r = 1.2$ mT/m, $\tau_{prep} = 3$ ms, $\tau_{enc} = 2$ ms, $G_e = 5.0$ mT/m, $\Delta = 1$ mm, FOV = 236 mm × 236 mm (236 mm × 30 mm each band)

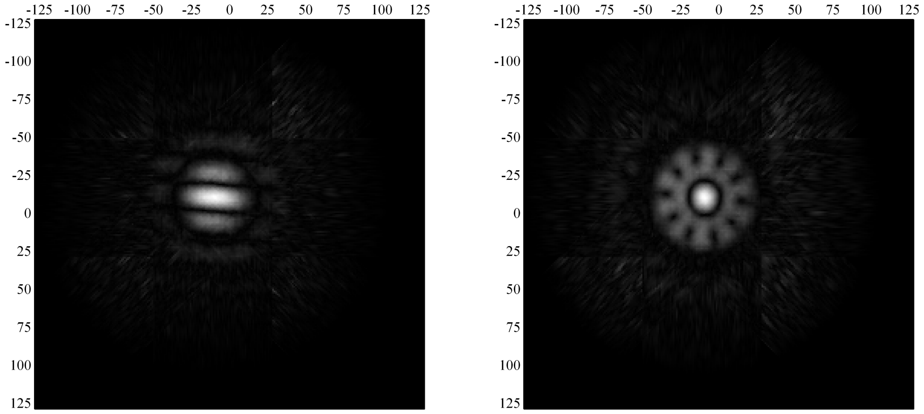

Figure 4.14: k-space signal maps of the imaging experiments performed on 2 tubes (left) and 5 tubes (right) after regridding and averaging processes. Imaging parameters: $N_e = 31$, $N_r = 78$, $\alpha = 9^o$, $\tau_r = 9$ ms, $G_r = 1.2$ mT/m, $\tau_{prep} = 3$ ms, $\tau_{enc} = 2$ ms, $G_e = 5.0$ mT/m, $\Delta = 1$ mm, FOV = 236 mm × 236 mm (236 mm × 30 mm each band)

4.2.7.4 Final matrix and FOV

After all these manipulations in k-space we get a square data matrix (Figure 4.14). Standard FFT is applied to the regdridded data matrix. Due to regridding on a bigger matrix size the final FOV can exceed the initial one by a factor of 10.

In addition, special window functions were applied to the k-space in order to remove Gibbs oscillations on the final image. In our work we considered application of the very typical for traditional MRI Hanning window function [47]. From our results it can be seen (Figure 4.15) that the image obtained using a Hanning window is almost free from Gibbs artifact and is not much distorted. But using cosine functions of 2nd and 3rd orders provide a better resolution with leftover distortions due to Gibbs artifacts. These window functions can be helpful to use when the size of the imaged object is quite small and when having a higher resolution is very important, even if it introduces some degree of Gibbs artifacts. When the imaged object is very large and its structure is important, using the Hanning window is an optimal solution.

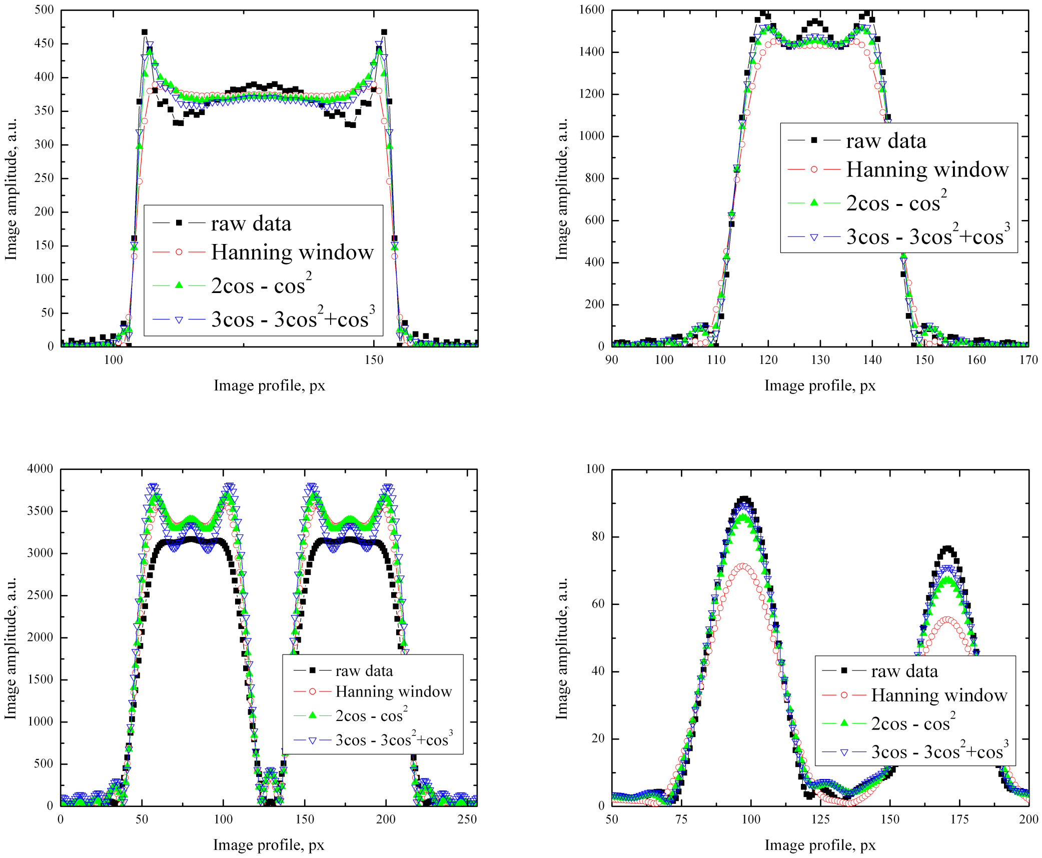

Figure 4.15: Illustration of the application of different window functions. Examples of 2D image profiles are shown. For small objects when higher resolution is important the 2nd or 3rd order cosine window functions are preferable. Imaging parameters: $N_e = 24$, $N_r = 18$, $\alpha = 18^o$, $\tau_r = 2.4$ ms, $G_r = 5.25$ mT/m, $\tau_{prep} = 2$ ms, $\tau_{enc} = 2$ ms, $G_e = 3.65$ mT/m, $\Delta_r = 3$ mm, $\Delta_{enc} = 1.9$ mm, FOV = 53 mm × 45 mm

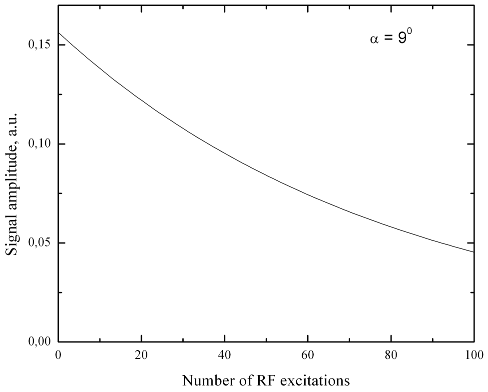

Figure 4.16: Plot of a function eq.4.16 demonstrates the magnetization (signal) losses during constant flip angle sequences for $\alpha = 9^o$.

4.2.7.5 Compensation of tip angle losses

One of the specific features of a constant tip angle application in HP gas MRI is the decrease of the total magnetization with each applied RF pulse. It results in a significant decrease of the signal between the first and the last applied RF pulses. Calculated illustration of the sample magnetization losses after series of 9^o rf pulses is shown on Figure 4.16. This “inhomogeneity” during k-space sampling leads to image distortions and decreases the resolution on the final image [67].

One of the solutions that helps to obtain the same signal in the beginning and in the end of the sequence is using a variable flip angle [68, 69]. In this method the amplitude of each RF pulse is adapted to the losses of magnetization and this provides almost the same level of signal throughout all the sequence. Another solution, that was actually used for processing all the images in this work, is a post acquisition correction of the signal based on the known tip angle. As a result of this correction, one recovers the image resolution to expected for uniform signal amplitude after rf excitation during whole sequence. Obviously after correction the SNR of the image decreases because of the noise enhancement. The difference in the noise levels between the first and fourth bands is illustrated in Figure 4.17. The applied correction increases the noise level for the last acquired bands. Higher noise level decreases the SNR of the image.

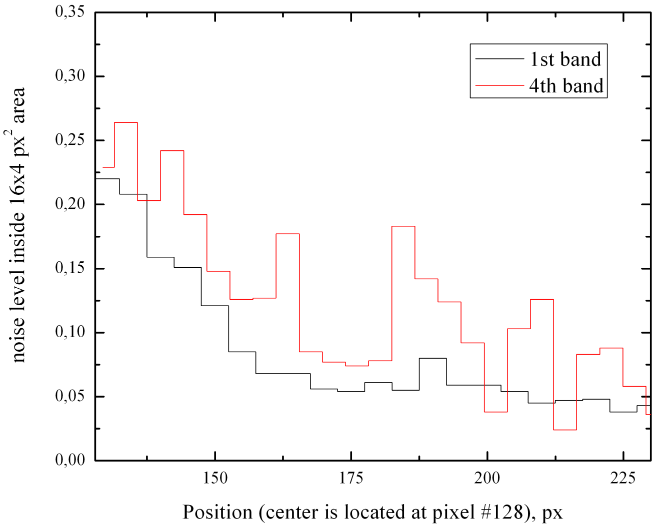

Figure 4.17: Illustration of the tip angle correction: enhanced noise level of the last band in k-space of the noise map.

4.2.7.6 Compensation of the diffusion effects

Diffusion attenuation during readout time of each echo is an another possible source of limitation of the resolution. In all our experiments we acquired 2 gradient echoes. Thus, it is possible to make a correction on the diffusion effects for each readout scan based on the measured ratios of the echoes. In the examples given in this chapter, the attenuation was rather small (within a range of 50%), and this correction was not performed.

4.2.7.7 Noise map for FLASH and DC sequences

For our obtained images SNR will be defined as the ratio between the signal amplitude in the ROI inside of the tube and the s.d. of values over the same ROI in a noise map obtained from a separate acquisition without HP gas. We do it because noise in the image outside of the sample is inhomogeneous and depends on the distance from the center of the image (there are unfilled parts of the k-space). An example of the noise map and corresponding k-space is presented in Figure 4.18. The round shape of the noise contribution in k-space map results from the apodization process. Each band in a DC SLASH sequence is an anisotropic FLASH sequence. A noise map obtained by one single

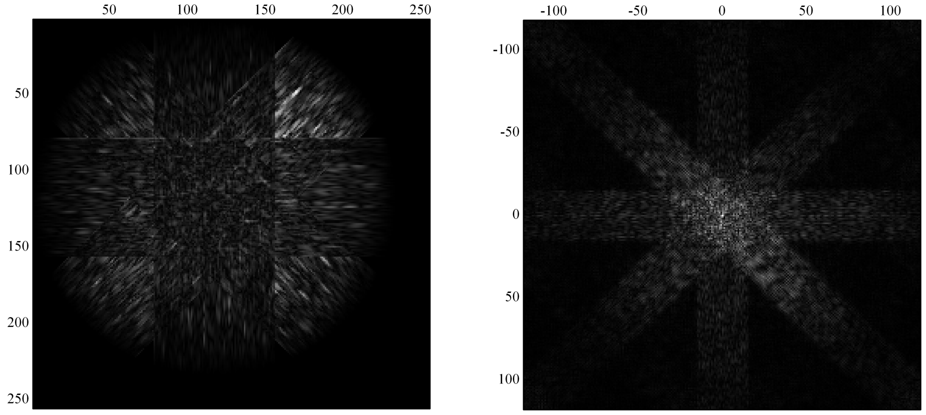

Figure 4.18: Noise map in k-space (left) and its image (right) obtained by the DC SLASH sequence. Imaging parameters for each band: $N_e = 31$, $N_r = 78$, $\alpha = 9^o$, $\tau_r = 9$ ms, $G_r = 1.2$ mT/m, $\tau_{prep} = 3$ ms, $\tau_{enc} = 2$ ms, $G_e = 5.0$ mT/m, $\Delta = 1$ mm, FOV = 236 mm × 236 mm (236 mm × 30 mm each band)

band is also anisotropic. The structure of the DC SLASH sequence with four separate bands leads to a fact that the noise map in k-space for a DC SLASH sequence has the shape of a star. Each band represents a "ray" of this star. The profile of the noise map for FLASH sequence in scan direction is wide and is limited by the detection bandwidth. It produces the resonance curve of the detection circuit. At the same time, the noise profile in the phase encode direction is narrow and the noise values within profile do not vary much (Figure 4.19). The application of the DC SLASH sequence mixes up readout and phase encode directions thus the profile of the noise map becomes a sum of them. It is uniform in every direction.

4.2.7.8 Resolution and SLASH sequences

The data obtained by a DC SLASH sequence is the sum of the data acquired using anisotropic FLASH sequences with resolutions Δx and Δy. After summation the highest resolution along the phase encode direction Δy becomes uniform for every orientation. An illustration of the evolution of the resolution from Δx across the image to Δy is presented in Figure 4.20. Imaging experiment was performed on the set of 2 tubes (5 cm long, i.d. 1.1 cm each) filled with ^{3}He gas under 500 mbar pressure using DC SLASH

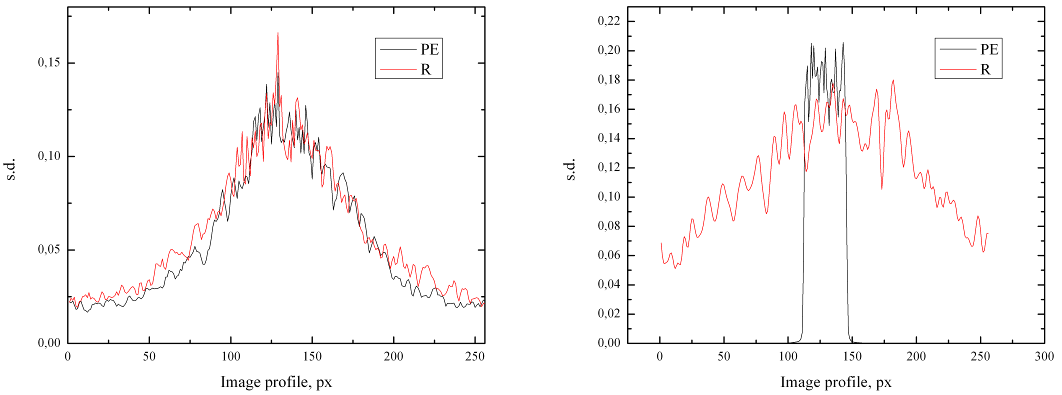

Figure 4.19: Profiles (projection) of the noise maps for the whole data set of the DC SLASH sequence (left) and only one band of the DC SLASH sequence (right). The profile of the noise map for one band of the DC SLASH sequence is that of the anisotropic FLASH sequence: in the readout direction it is wide and corresponds to a resonance curve of the detection circuit; in the phase encode direction it is narrow.

sequence. DC SLASH sequence contains of 4 bands. The series of images based on the first band, combination of first and second bands, combination of first, second and third bands, and all four bands are shown. It can be seen that with each new band acquired, the image resolution becomes more uniform and closer to Δy in all directions.

4.2.7.9 Limitations of the SLASH sequence

Since SLASH sequence takes advantage of quite long acquisition time τ_r, the main limitations are coming from the experimental conditions that can limit this time. SLASH sequence will not provide any gain in the image SNR or resolution if the readout time τ_r is short enough. This will not allow us to sample the k-space in read direction with an important number of data points that is suitable to obtain enhancement of the image SNR or the image resolution. Concerning HP gas lung MRI, such situation can be met in few situations. Definitely, T_2^* is short in lungs or porous materials at high magnetic fields. Automatically that means, that SLASH sequence (for which $\tau_r < T_2^*$) can be efficient only at low or moderate magnetic fields. However, at low magnetic fields situations of a very strong diffusion inside the sample caused by high applied gradients of the signal can

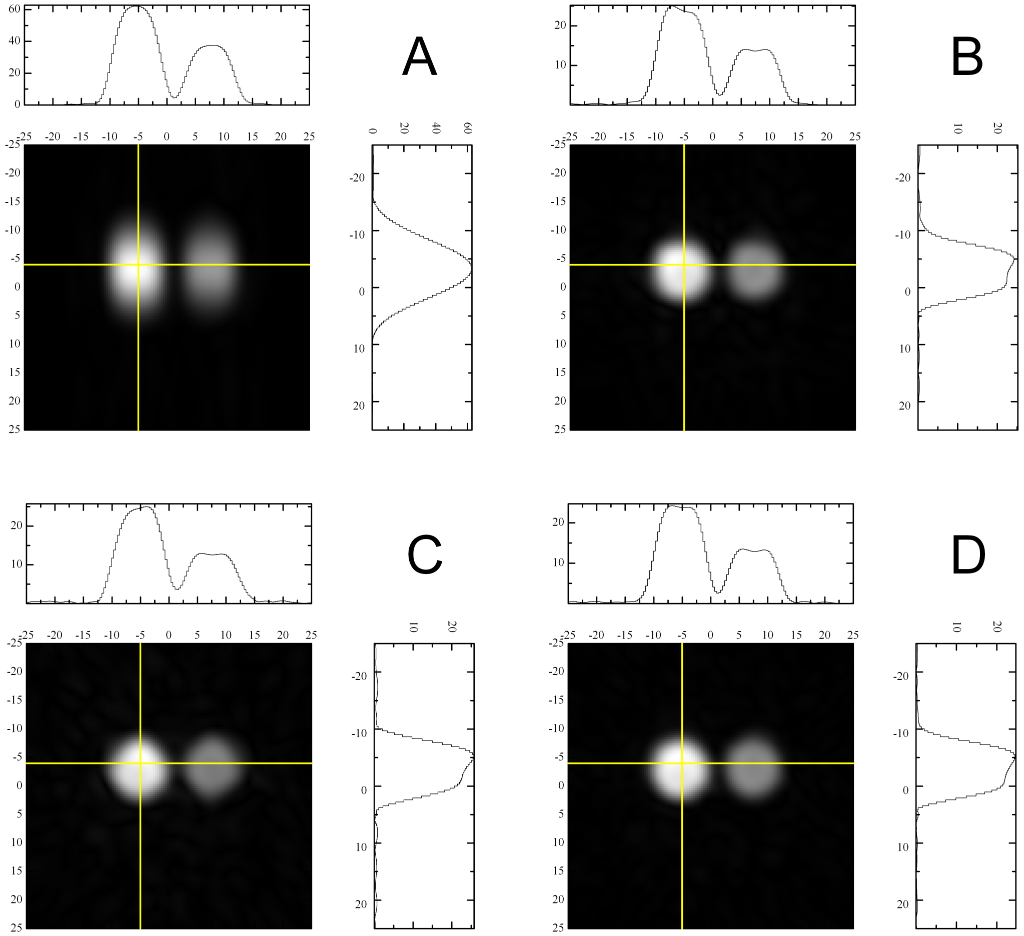

Figure 4.20: Illustration of the resolution enhancement with acquisition of each new band of the DC SLASH sequence. Image (A) is obtained for the only first acquired band, (B) - for the combination of first and second bands, (C) - for the three bands, and the fourth image is the final DC SLASH image. Resolution in the readout direction Δx on the first image is 3 times higher than the resolution in the phase encode direction Δy. In the image (D), they are almost equal $\Delta x \approx \Delta y$. Images were made for the set of 2 tubes (5 cm long, i.d. 1.1 cm each) filled with ^{3}He gas under 500 mbar pressure. Imaging parameters: $N_e = 25$, $N_r = 78$, $\alpha = 9^o$, $\tau_r = 9$ ms, $G_r = 0.62$ mT/m, $\tau_{prep} = 2$ ms, $\tau_{enc} = 2$ ms, $G_e = 3.54$ mT/m, $\Delta = 2$ mm, FOV = 472 mm × 472 mm (472 mm × 50 mm each band)

be met. Corresponding strong diffusion attenuation during acquisition also sets a limit on a τ_r. Imaging parameters in our experiments were chosen to avoid strong diffusion attenuation and in this case, the main limiting circumstance is the T_2^* value of a given static magnetic field inhomogeneity.

4.2.8 Comparison of DC SLASH and FLASH sequences

Imaging parameters for both sequences were chosen to demonstrate the specific advantages of the DC SLASH sequence. To check expected improvement of the image resolution or SNR with DC SLASH sequence, sets of 2 and 5 tubes filled with mixture of HP ^{3}He (500 mbar) and N_2 (500 mbar) gases were used as a samples. One FLASH sequence with a resolution that corresponds to 1.8 mm in the phase encoding direction and 2.5 mm in the readout direction was used as a reference. For DC SLASH sequences we used 2 sets of parameters, one of them providing nearly the same resolution (2.0 mm), but much better expected SNR (basing on eq.4.63), another set should provide better resolution (1.0 mm) with similar expected SNR. A resolution of 1.0 mm for the current samples was impossible to obtain with FLASH sequence due to strong diffusion effect and hardware limitations. The imaging parameters actually used are given in Table 4.1.

Table 4.1: Imaging parameters of used DC SLASH and FLASH sequences. Following parameters are presented in each column: tipping angle α^0, number of acquired points in read N_r and encode N_e directions, read G_r and maximum encode G_{enc} gradient values, corresponding gradient application times τ_r and τ_{enc}, final resolution of the image Δ and FOV of each acquired SLASH (or FLASH) band

	Sequence	α^0	N_r	N_e	G_r**, mT/m**	τ_r**, ms**	G_{enc}**, mT/m**	τ_{enc}**, ms**	Δ**, mm**	**FOV, mm**
A	DC SLASH	9	78	25	0.62	9	5.5	2	1.0	472 x 50
B	DC SLASH	9	78	31	1.32	9	5.5	2	2.0	236 x 30
C	FLASH	18	18	24	5.5	2.5	4.4	2	2.5 x 1.8	53 x 45

The SNR measured in every image was scaled to the initial gas magnetization value obtained from the FID signal recorded just before the sequence was applied. The SLASH sequence with the resolution of 2 mm provided images with SNR = 330, which is few times higher than the SNR of the images obtained by FLASH sequence with a similar

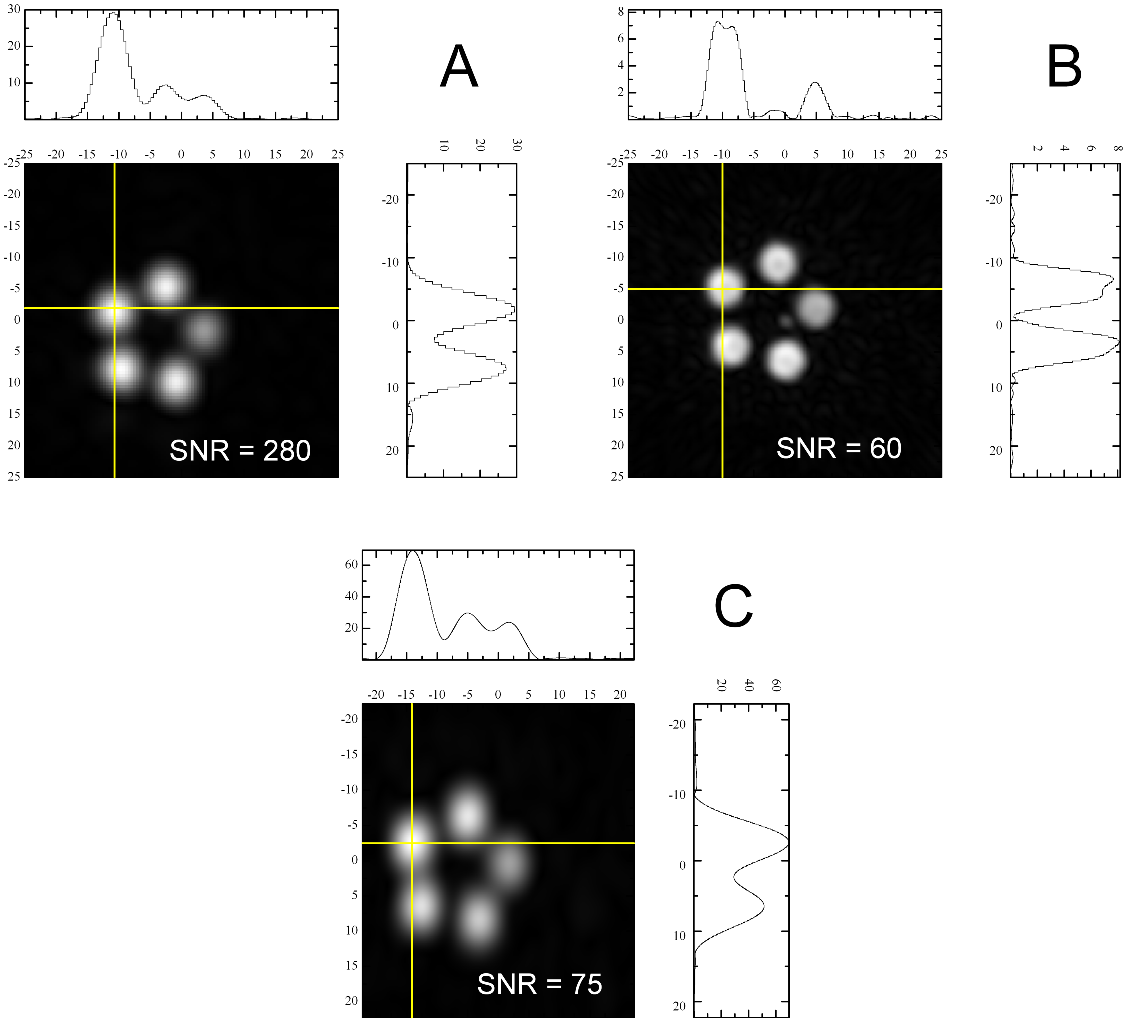

Figure 4.21: Three 2D images of 5 tubes obtained by DC SLASH (top left and top right) and FLASH (bottom) sequences. The imaging parameters are given in Table 4.1

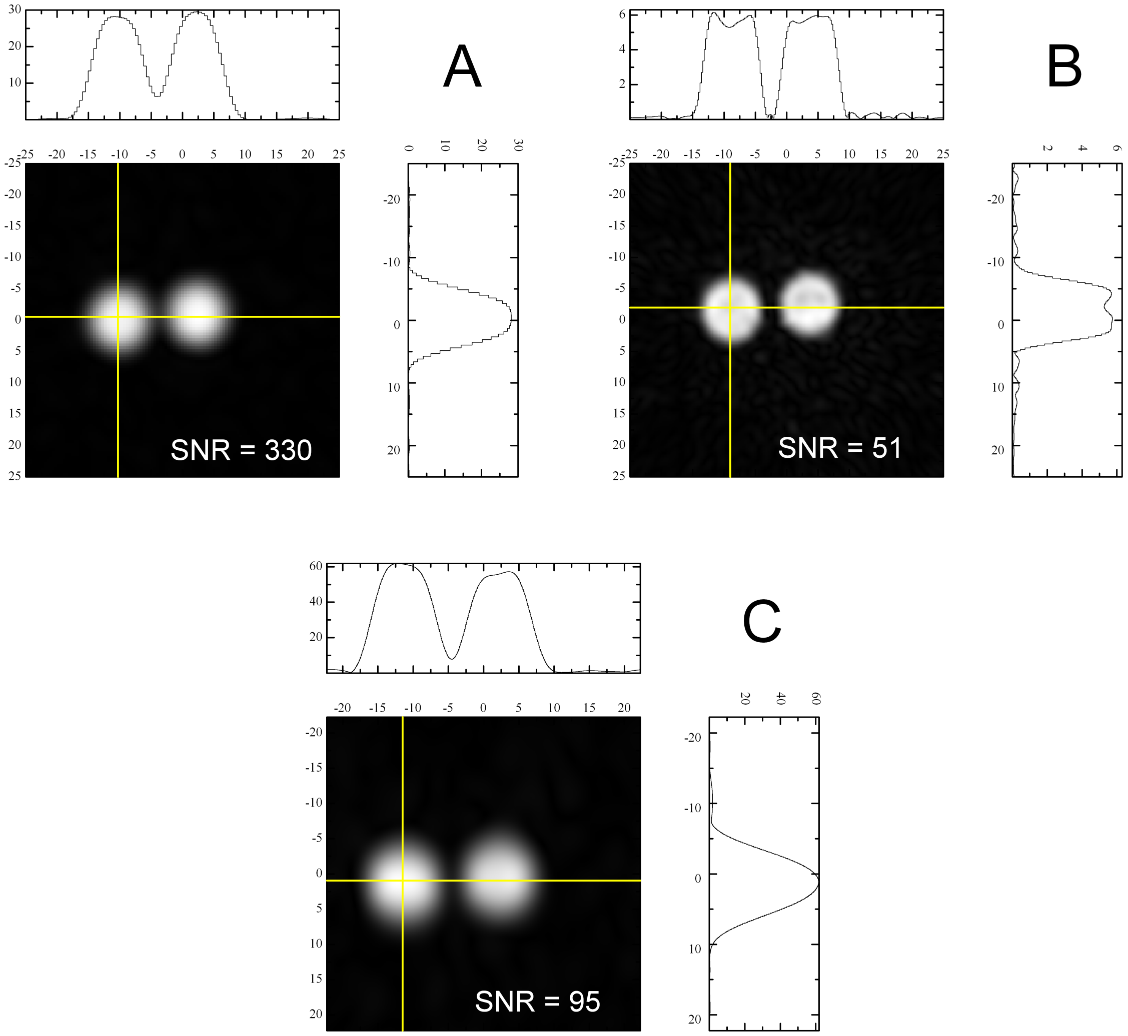

Figure 4.22: Three 2D images of 2 tubes obtained by DC SLASH (top left and top right) and FLASH (bottom) sequences. The imaging parameters are given in Table 4.1

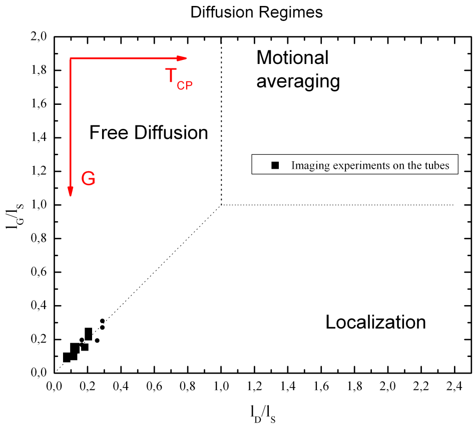

Figure 4.23: Diagram of the diffusion regimes met in our imaging experiments in reduced units of l_G/l_S, l_D/l_S for the set of 2 and 5 tubes filled with HP ^{3}He under 500 mbar pressure or mixture of HP ^{3}He and N_2 gas under 500 mbar pressure each. Arrows show how diffusion regime changes with increase of gradient strength G and (or) echo time T_{CP}

resolution (SNR = 95). At the same time, the SNR of the high resolution (1 mm) image obtained by SLASH sequence is SNR = 85. A clear improvement of the image SNR or resolution is obtained by using SLASH sequence instead of FLASH.

4.2.9 Diagram of the diffusion regimes in imaging experiments on tubes

In this section in our experiments we used sets of tubes with inner diameters 7 and 11 mm. Tubes were filled by pure ^{3}He gas (500 mbar) or a mixture with nitrogen (500/500 mbar). The diagram of the diffusion regimes for our samples and used imaging parameters is plotted in Figure 4.23. In all our imaging experiments on tubes (Table 4.1), the diffusion regime was a crossover regime between free diffusion and localization regime.

4.3 Lung imaging

4.3.1 2D FLASH projection images

Demonstrations and verifications of the imaging techniques were made using preserved lungs of a small mammalian provided by Nasco[1] (this product is not officially documented, but the smaller preserved lungs provided by Nasco for educational purposes are believed to be cat lungs). This lungs are convenient samples, they have a better and more complicated morphology than the sets of glass tubes used in the previous sections and their inner structure consists of connected airways and alveolar sacs with various sizes. However our samples tended to leak when they were inflated beyond 2-4 cm^3 (exact volume depended on the exact lungs), in contrast with the swine lungs also prepared by Nasco. T_1 measurements for the ^{3}He gas in the lungs were made by looking to FID amplitude decay after series of rf pulses with small tipping angle. In the lungs we have used, we found $T_1 \approx 6\ min$. Series of 2D projection FLASH imaging experiments in XZ and XY planes with double gradient echo were performed. According to the mentioned above limitation of the inflation volume, the lungs with highest one were chosen and were filled with up to 4 cm^3 of pure ^{3}He gas at atmospheric pressure. Examples of obtained lung images are demonstrated in Figures 4.24-4.26. The SNR of the images is up to 10 for a resolution $\Delta \approx 1.6\ mm$. The ratio between this imaging resolution in imaging plane $\Delta = 1.5\ mm$ and thickness of the imaging slice of 5 cm is significantly different, which makes such a high resolution meaningless. Slice selection or 3D imaging experiments look more sensible at this point.

4.3.2 2D SLASH projection images

Series of 2D projection DC SLASH imaging experiments in XY plane with double gradient echo were performed. The same imaging parameters that were used for the sets of tubes imaging were used for the lung imaging. Lungs were filled with up to 4 cm^3 of pure ^{3}He gas at atmospheric pressure. Examples of lung images are shown in Figures 4.27 and 4.28. Before the sequence, small rf excitation was applied to the samples in order

---

[1] 901 Janesville Avenue, P.O. Box 901, Fort Atkinson, WI 53538-0901, USA, www.enasco.com

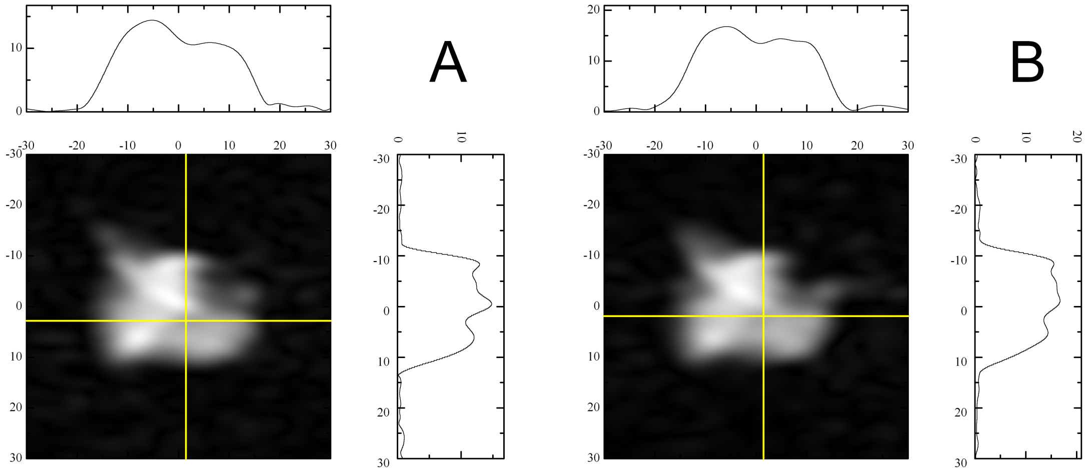

Figure 4.24: 2D transverse projection FLASH images in XZ plane (A - 1st echo, B - 2nd echo) of the preserved lungs filled with ^{3}He gas under 1 bar pressure. The part of trachea is visible and connects to the fill line, on the right side of the image. Imaging parameters: $N_e = 24$, $N_r = 60$, $\alpha = 17^o$, $\tau_r = 6.6$ ms, $G_r = 3.15$ mT/m, $\tau_{prep} = 4.9$ ms, $\tau_{enc} = 2$ ms, $G_e = 2.58$ mT/m, $\Delta_r = 1.5$ mm, $\Delta_{enc} = 2.7$ mm, FOV = 89 mm × 65 mm

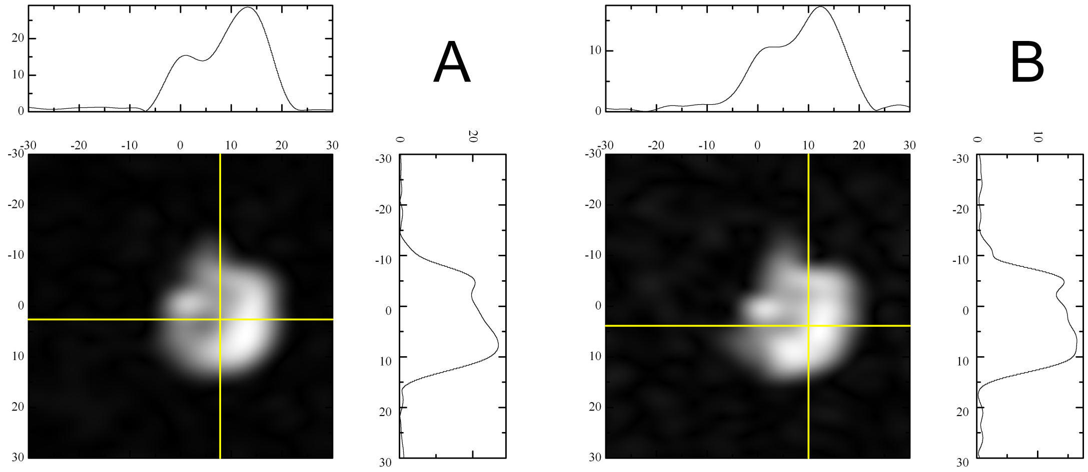

Figure 4.25: 2D axial projection FLASH images in XY plane (A - 1st echo, B - 2nd echo) of the preserved lungs filled with ^{3}He gas under 1 bar pressure. Imaging parameters: $N_e = 24$, $N_r = 60$, $\alpha = 18^o$, $\tau_r = 6.6$ ms, $G_r = 3.15$ mT/m, $\tau_{prep} = 3.45$ ms, $\tau_{enc} = 2$ ms, $G_e = 2.19$ mT/m, $\Delta_r = 2.2$ mm, $\Delta_{enc} = 3.2$ mm, FOV = 89 mm × 77 mm

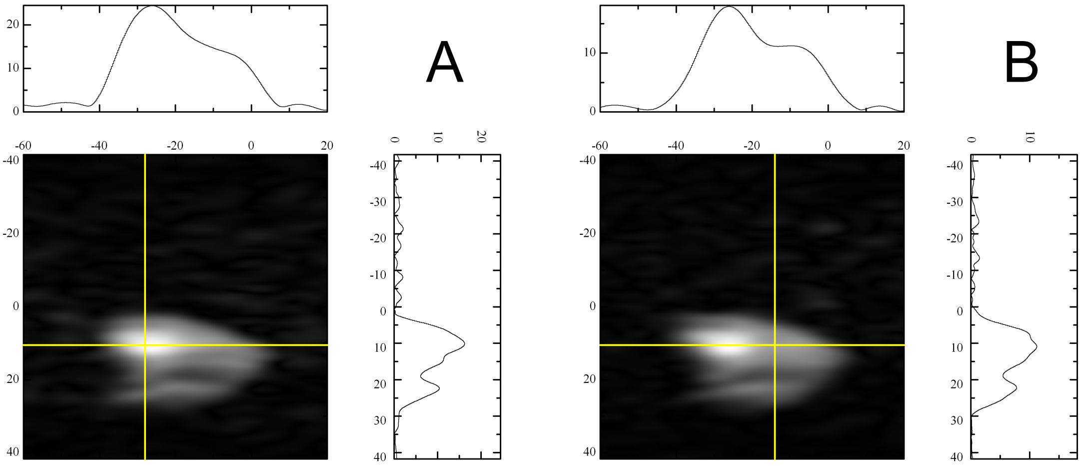

Figure 4.26: A 2D transverse projection FLASH images in XZ plane (A - 1st echo, B - 2nd echo) of the preserved lungs filled with ^{3}He gas under 1 bar pressure. Imaging parameters: $N_e = 24$, $N_r = 18$, $\alpha = 17^o$, $\tau_r = 2.4$ ms, $G_r = 3.36$ mT/m, $\tau_{prep} = 3.4$ ms, $\tau_{enc} = 2$ ms, $G_e = 1.20$ mT/m, $\Delta_r = 1.4$ mm, $\Delta_{enc} = 5.7$ mm, FOV = 84 mm × 140 mm

to check the total gas polarization value by FID signal amplitude. Unfortunately, the helium-3 gas polarization in these experiments was far from optimal value and lower than in FLASH experiments: 9.8% in 4.27 and 12.8% in 4.28. The SNR of these images is up to 20 for a resolution $\Delta \approx 2\ mm$ and 10 for a resolution $\Delta \approx 1\ mm$. Very low diffusion attenuation between two images (7%) points out to the fact that SNR or resolution can be increased in further experiments after optimization of the imaging parameters. However, resolution enhancement in this imaging plane is meaningless for such thick objects (structural variations inside a thick slice are significant) and non-slice selective sequences. But the obtained SNR values show a potential of the DC SLASH sequence, that can be used for slice-selective 2D imaging or 3D imaging in future.

4.3.3 3D Flash

Series of 3D FLASH imaging experiments with double gradient echo and without slice selective rf pulse were performed. Lungs were filled with up to 4 cm^3 of pure ^{3}He gas at atmospheric pressure. Examples of lung images are shown in Figure 4.29. According to these images value of SNR is up to 25.

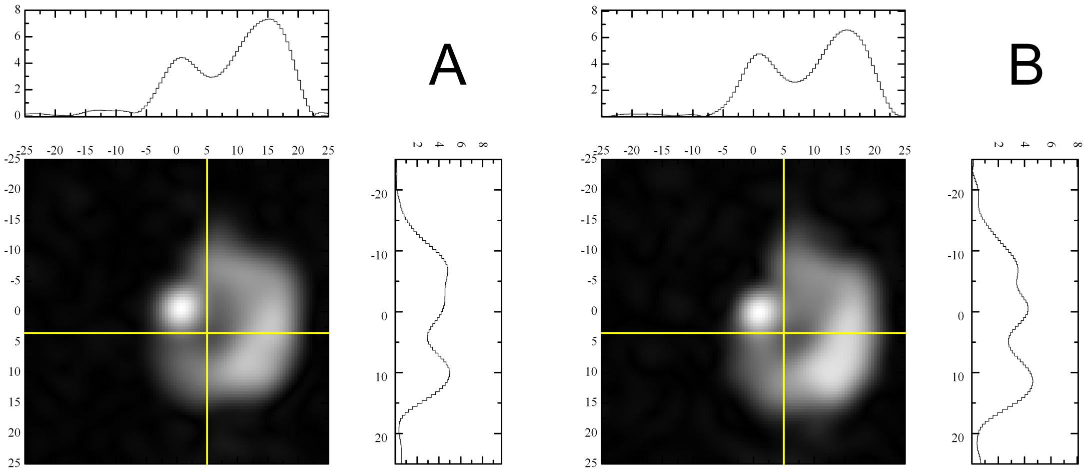

Figure 4.27: 2D axial projection SLASH images in XY plane (left - 1st echo, right - 2nd echo) of the preserved lungs filled with ^{3}He gas under 1 bar pressure. The trachea is visible in the center of the image. Imaging parameters: $N_e = 25$, $N_r = 78$, $\alpha = 9^o$, $\tau_r = 9$ ms, $G_r = 0.62$ mT/m, $\tau_{prep} = 2$ ms, $\tau_{enc} = 2$ ms, $G_e = 3.54$ mT/m, $\Delta = 2$ mm, FOV $= 472$ mm $\times$ 472 mm (472 mm $\times$ 50 mm each band)

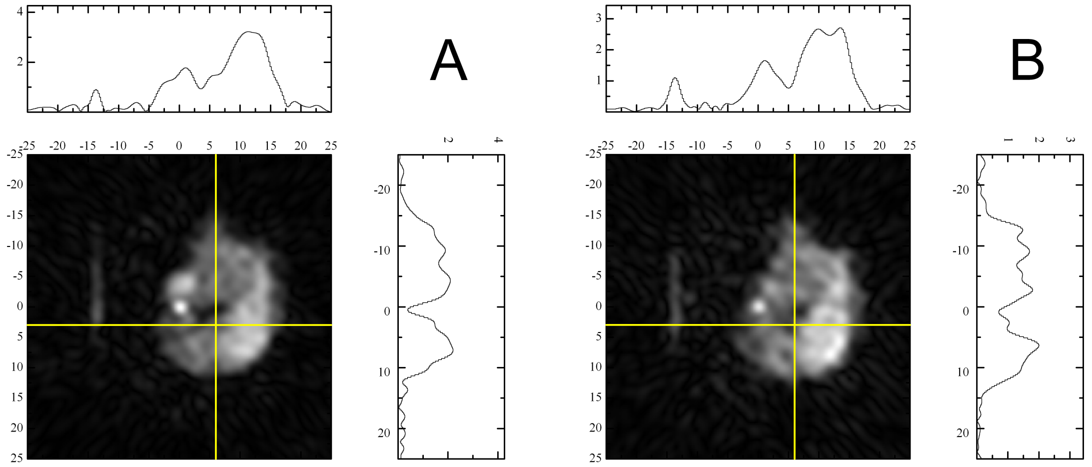

Figure 4.28: 2D axial projection SLASH images in XY plane (left - 1st echo, right - 2nd echo) of the preserved lungs filled with ^{3}He gas under 1 bar pressure. The trachea is visible in the center of the image. Imaging parameters: $N_e = 31$, $N_r = 78$, $\alpha = 9^o$, $\tau_r = 9$ ms, $G_r = 1.2$ mT/m, $\tau_{prep} = 3$ ms, $\tau_{enc} = 2$ ms, $G_e = 5.0$ mT/m, $\Delta = 1$ mm, FOV $=$ 236 mm $\times$ 236 mm (236 mm $\times$ 30 mm each band)

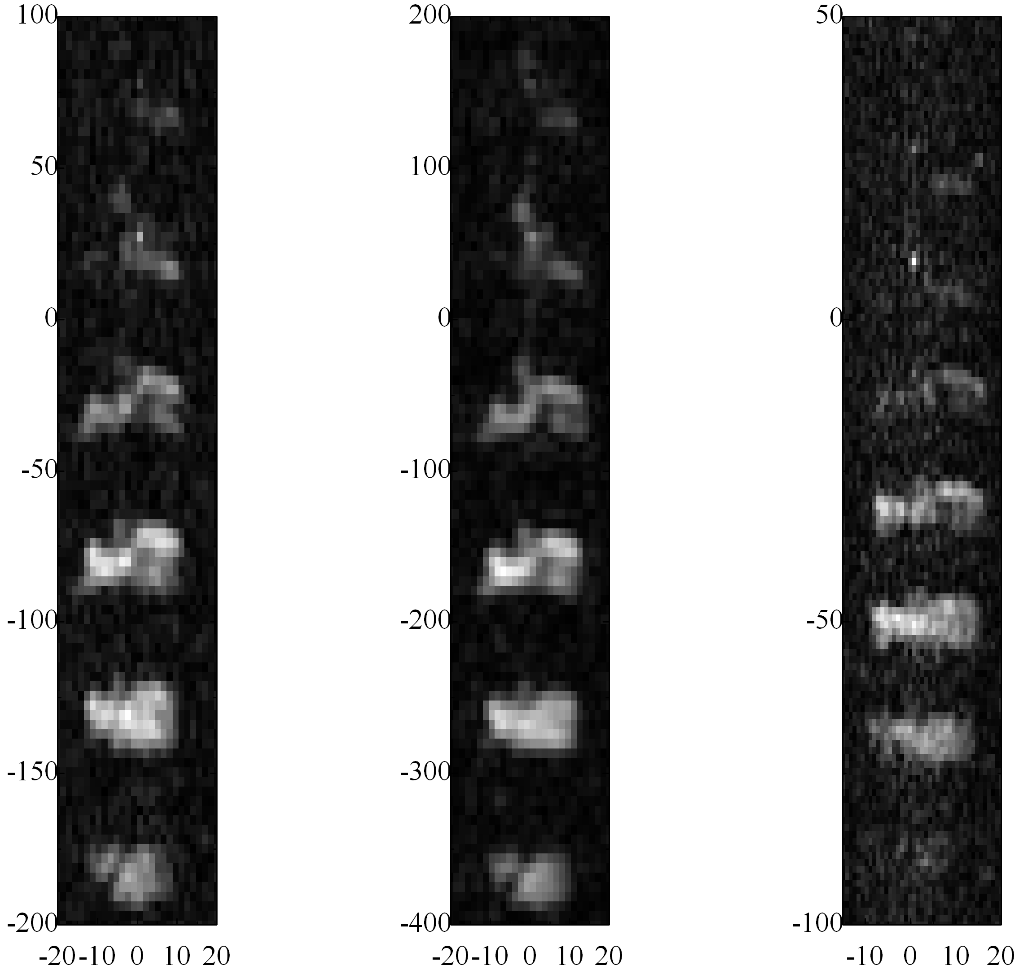

Figure 4.29: 3D FLASH images (as a stack of slices) of the preserved lungs filled with ^{3}He gas under 1 bar pressure. Imaging parameters: (A) 11 slices (only slices containing MR signal are shown), slice thickness 6.7 mm, $N_e = 11$, $N_r = 62$, $\alpha = 8^o$, $\tau_r = 6.8$ ms, $G_r = 3.15$ mT/m, $\tau_{prep} = 2$ ms, $\tau_{enc} = 2$ ms, $G_e = 1.12$ mT/m, $\Delta_r = 1.5$ mm, $\Delta_{enc} = 5.7$ mm, FOV $=$ 89 mm $\times$ 63 mm; (B) 11 slices (only slices containing MR signal are shown), slice thickness 6.7 mm, $N_e = 11$, $N_r = 40$, $\alpha = 8^o$, $\tau_r = 4.6$ ms, $G_r = 3.15$ mT/m, $\tau_{prep} = 2$ ms, $\tau_{enc} = 2$ ms, $G_e = 0.996$ mT/m, $\Delta_r = 2.2$ mm, $\Delta_{enc} = 6.4$ mm, FOV $=$ 89 mm $\times$ 70 mm, (C) 11 slices (only slices containing MR signal are shown), slice thickness 6.7 mm, $N_e = 11$, $N_r = 60$, $\alpha = 7^o$, $\tau_r = 6.6$ ms, $G_r = 5.25$ mT/m, $\tau_{prep} = 3.15$ ms, $\tau_{enc} = 2.25$ ms, $G_e = 0.996$ mT/m, $\Delta_r = 0.9$ mm, $\Delta_{enc} = 5.7$ mm, FOV $=$ 53 mm $\times$ 63 mm

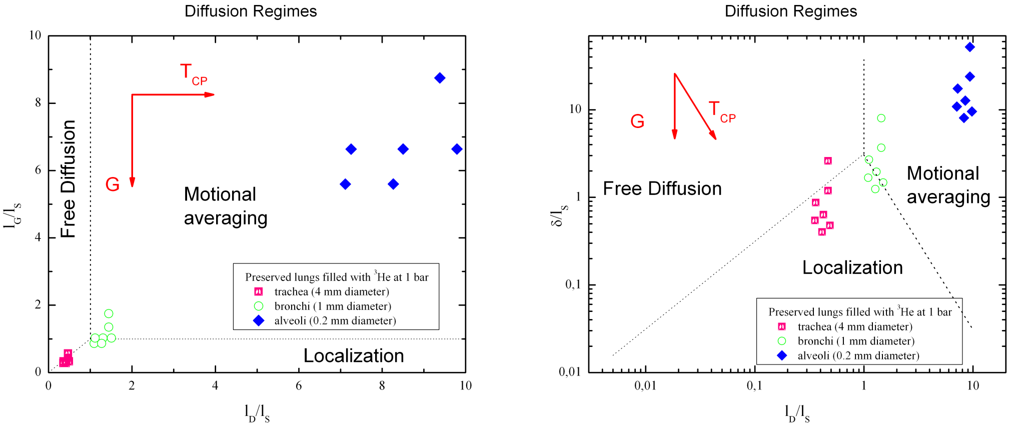

Figure 4.30: Diagram of the diffusion regimes met in our imaging experiments in relative units of l_G/l_S, l_D/l_S (left) and δ/l_S, l_D/l_S (right) for the preserved lungs filled with HP ^{3}He under 1 bar pressure. Arrows show direction of the diffusion condition changes with increasing of gradient strength G and echo time T_{CP} of the sequences

4.3.4 Diagram of the diffusion regimes in lung imaging experiments

Diagrams of the diffusion regimes (Figure 4.30) were created on the basis of all image sequences parameters used in this work on preserved lungs. Points in diagrams are plotted using basic dimensions of cat lung airways: trachea (4 mm diameter), bronchi (1 mm diameter) and alveoli (0.2 mm diameter) [57]. Diagrams show that in all our imaging experiments diffusion regimes are heterogeneous within the lungs and depending on the airway dimensions vary from motional averaging regime (alveoli) to crossover regime of localization and free diffusion (trachea).

4.3.5 ADC maps

The mean value of the apparent diffusion coefficient (ADC) distribution and its standard deviation provides information on the lung morphology and lung pore sizes, where the major part of the gas is concentrated. Such histograms are often used in clinical applications and deviations in the distribution of ADC's are used to detect morphology problems in the lungs. For the case of a healthy human lungs, the typical mean ADC value is 0.2 cm^2/s for He^3 mixed with normal air (20% ^{3}He and 80% N_2). Any increase of the ADC values from the usual ones reports about structural destructions and alveolar sizes larger than normal.

Diffusion attenuation in the presence of the gradients is proportional to $\exp(-bD)$ (eq.4.24). Pixel-per-pixel comparison of the two images obtained within the same scan by a double gradient echo technique can provide the apparent diffusion coefficient $D_{app,i}$ values for each i-th pixel of the image. We will consider two methods for $D_{app,i}$ calculations. The first method is based only on the image amplitudes. The second one considers also the noise values from the obtained noise maps just after the application of the imaging sequences and the advantage of squared signal values [48]. This method increases accuracy of the obtained $D_{app,i}$ values for the images with low SNR. Thus, D_{app} maps created using the second method are less biased. If the signal amplitude within the i-th pixel of the image based on the first echo is S_i, the signal amplitude on the second image is T_i, noise level on the noise map is N_i, then we can write

$$-bD^{(1)}_{app,i} = \ln \frac{T_i}{S_i} \tag{4.64}$$

$$-bD^{(2)}_{app,i} = \frac{1}{2} \ln \frac{\left|T_i^2 - \langle N_i \rangle^2\right| + \epsilon}{\left|S_i^2 - \langle N_i \rangle^2\right| + \epsilon} \tag{4.65}$$

Here the small number ϵ is added to avoid division by zero for some pixels during images processing.

The free diffusion coefficient D_0 can be calculated for the given experimental conditions using equation 3.36. Then, expected signal attenuation value $-bD_0$ for the free diffusion regime can be calculated using eq. 4.25 for the imaging sequence parameters. The ratio between the apparent diffusion coefficient and the free diffusion coefficient D_{app}/D_0 can be simply found.

We discussed a method of obtaining diffusion attenuation maps and D_{app}/D_0 histograms in lung imaging. In our case of 2D projection images voxel size is anisotropic and is much larger than size of the lung structure. Hence, attenuation maps have no sense. But implementation of this method for 3D images with a reasonable voxel size is possible. An in-house software was used for the analysis of the data. This software allows us to obtain signal attenuation $-bD_{app}$ maps from a couple of 3D FLASH images we made, and then to sort data as a histogram of attenuation ratios D_{app}/D_0. User-defined noise threshold removes a majority of error pixels in the image outside of the object created by noise spikes.

In Figures 4.31 and 4.32, 3D images based on the first and second echo and corresponding attenuation maps $-bD_{app}$ for each slice of 3D images are shown. Histograms of the apparent diffusion coefficient based on the attenuation maps and imaging parameters were computed and then normalized to the free diffusion coefficient (D_{app}/D_0). Examples of D_{app}/D_0 histograms obtained from our imaging experiments on presented lungs are shown in Figure 4.33.

The distribution of the D_{app} values per voxels displays a distribution of ^{3}He nuclei located in the lung alveoli and airways of different dimensions. In terms of our definition of local $D_{app,i}$ values all the values $D_{app}/D_0 < 0$ are incorrect. It is obvious that the signal amplitude cannot increase within a voxel with time during gradient applications. But such values can be met after processing the data with low SNR due to noise spikes. Such errors can be erased by defining strong noise threshold level. But a too strong threshold level significantly decrease amount of data in the histograms in our experiments with low SNR.

Acquired images using two gradient echo technique in imaging experiments allowed to obtain signal attenuation maps of the samples. 3D attenuation maps were obtained for a various imaging parameters providing similar b-values. In all presented cases, the local apparent diffusion coefficient differs and is lower than the expected coefficient for free diffusion with the same imaging parameters. These results are in total agreement with the fact that restrictive motion occurs for the gas inside the lungs, that can not be considered as system with a free diffusion. At the same time, b-values for used imaging parameters were calculated. The mean values of the D_{app}/D_0, as well as their standard deviation are presented in Table 4.2 for a various b values. It can be found that apparent diffusion coefficient D_{app} distribution depends not only on the b value. If the diffusion regime is not free diffusion, then signal decay is determined both by the b-value, gradient timing and dephasing length. For the close b values (lines number 3 and 4 in Table 4.2), the mean D_{app} values are significantly distinguishable for this two experiments. Thus, in all cases apparent diffusion coefficient D_{app} should be presented in a set of both b

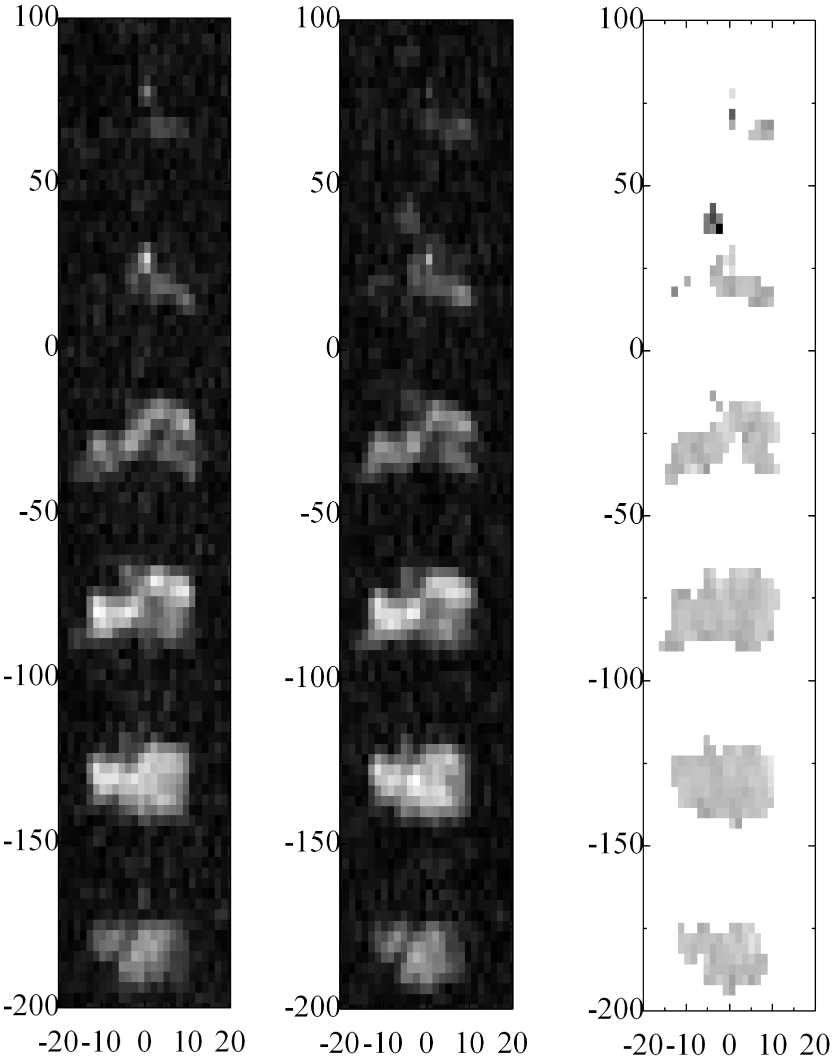

Figure 4.31: 3D FLASH images (first and second echo) and corresponding $-bD_{app}$ maps (as a stack of slices) of the preserved lungs filled with ^{3}He gas under 1 bar pressure. Horizontal and vertical scales are in mm. Imaging parameters: 11 slices (only slices containing MR signal are shown), slice thickness 6.7 mm, $N_e = 11$, $N_r = 62$, $\alpha = 8^o$, τ_r = 6.8 ms, $G_r = 3.15$ mT/m, $\tau_{prep} = 2$ ms, $\tau_{enc} = 2$ ms, $G_e = 1.12$ mT/m, $\Delta_r = 1.5$ mm, $\Delta_{enc} = 5.7$ mm, FOV = 89 mm × 63 mm

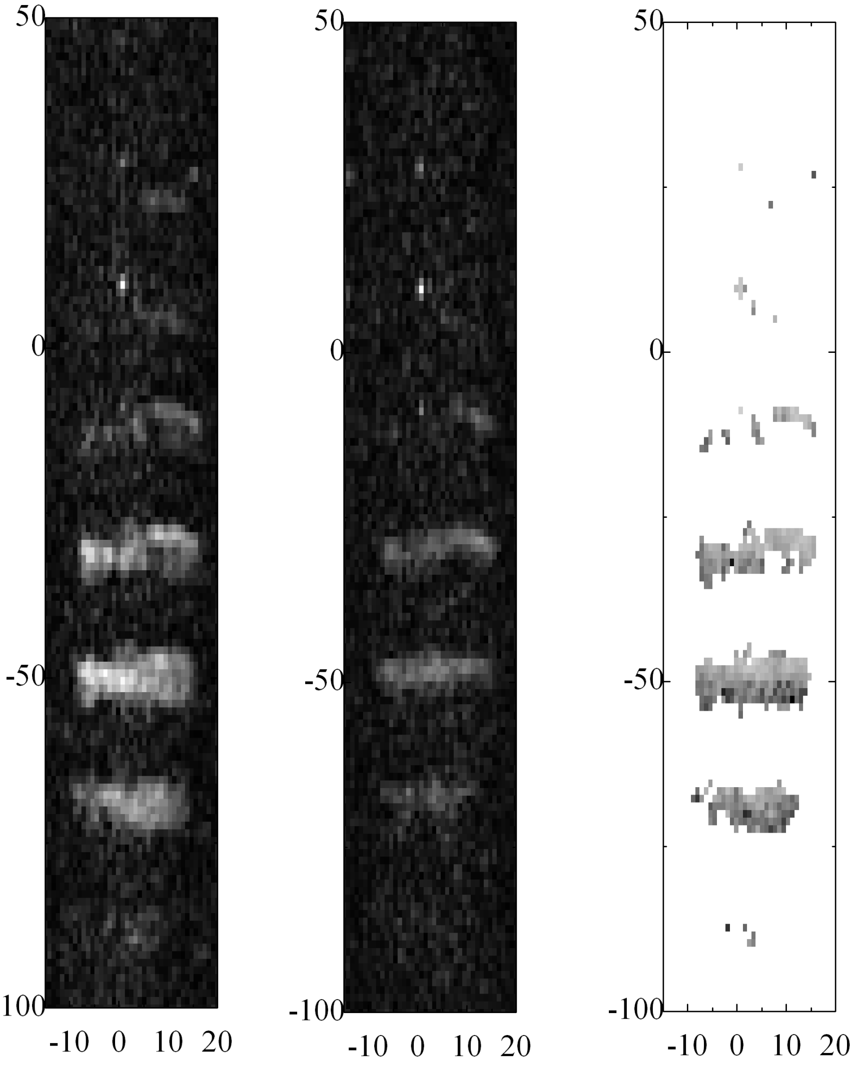

Figure 4.32: 3D FLASH images (first and second echo) and corresponding $-bD_{app}$ maps (as a stack of slices) and D_{app}/D_0 histograms of the preserved lungs filled with ^{3}He gas under 1 bar pressure. Horizontal and vertical scales are in mm. Imaging parameters: 11 slices (only slices containing MR signal are shown), slice thickness 6.7 mm, $N_e = 11$, $N_r = 60$, $\alpha = 7^o$, $\tau_r = 6.6$ ms, $G_r = 5.25$ mT/m, $\tau_{prep} = 3.15$ ms, $\tau_{enc} = 2.25$ ms, $G_e = 0.996$ mT/m, $\Delta_r = 0.9$ mm, $\Delta_{enc} = 5.7$ mm, FOV = 53 mm × 63 mm

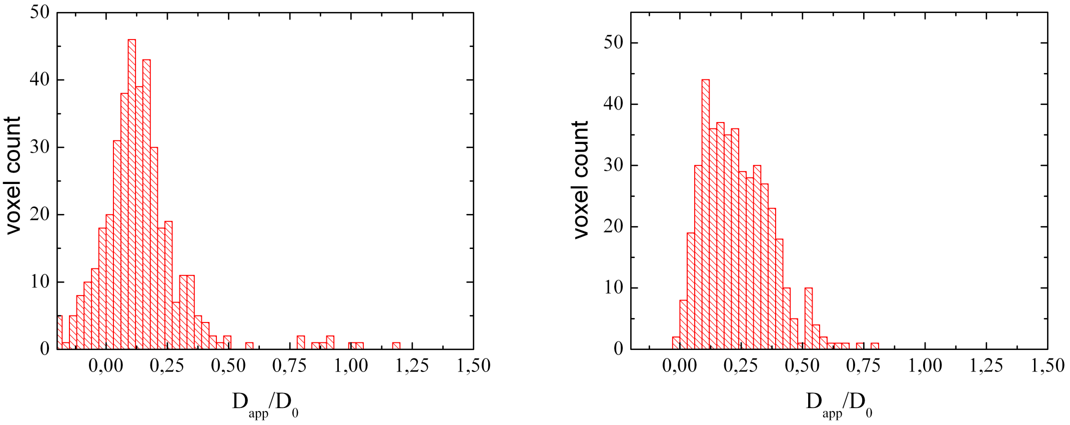

Figure 4.33: Global D_{app}/D_0 histograms of the preserved lungs filled with ^{3}He gas under 1 bar pressure. Experimental conditions correspond to the 2nd (left plot) and 3rd (right plot) lines of the Table 4.2.

value, gradient strength and gradient timing. Low field MRI gives a potential to explore diffusion coefficients over a wide range of gradient and diffusion times.

Table 4.2: Imaging parameters, corresponding b-values and measured D_{app}

#	G_r, **mT/m**	τ_r, **ms**	b, **s/cm^2**	$D^{(1)}_{app}/D$		$D^{(2)}_{app}/D$	
				Mean	**s.d.**	**Mean**	**s.d.**
1	5.5	4.5	0.79	0.257	0.240	0.268	0.234
2	3.3	6.7	1.00	0.135	0.189	0.138	0.179
3	5.5	6.5	2.53	0.219	0.135	0.235	0.137
4	3.3	9.1	2.6	0.086	0.061	0.092	0.072

Besides the ADC measurements, series of initial global CPMG measurements were performed for the same lung samples to check the feasibility of this method for a given sample. This experiments are the complementary to the ADC measurements based on comparison double echo gradient imaging sequence. Used CPMG parameters are given in Table 4.3. The range of gradient timings and strengths is very broad for the CPMG sequence. If, in imaging experiments, τ_r was not exceeding 10 ms, the CPMG sequence allowed to use long-time T_{CP} up to 48 ms in the same lung samples.

In preserved lungs, echo decay trains in CPMG measurements are usually found to be not mono-exponential, due to the heterogeneity of local D_{app} conditions. Examples of diffusion-attenuated echo trains are shown in Figure 4.34. In this experiments, the lungs were filled by 4 cm^3 (fully filled lungs) and 2 cm^3 (half filled lungs) of HP ^{3}He gas at 1 bar. In partially filled lungs the gas occupies less alveoli and is more concentrated in airways with bigger dimensions. Diffusion in bigger airways is less restricted and diffusion-induced attenuation is faster. Performed CPMG experiments confirm this fact. Diffusion-induced attenuation rate vary from the beginning to the end of the train echo. For rate $T_{2,diff}^{-1}$ in various parts of the echo train the apparent diffusion coefficient can be estimated using equation 3.16. For the gradient strength G_r = 0.2475 mT/m and echo time T_{CP} = 24 ms of the CPMG sequence, the obtained decay times change from $T_{2,diff}$ = 203 ms in the beginning of the echo train to $T_{2,diff}$ = 357 ms at the end of the echo train for fully filled lungs (Figure 4.34). Free diffusion coefficient for 1 bar ^{3}He gas at room temperature $D_0 = 1.967$ cm^2/s (eq. 3.37). Corresponding to the measured decay rates ratio of apparent diffusion coefficient and free diffusion coefficient $D_{app}/D_0 = 0.404$ in the beginning of the echo train and $D_{app}/D_0 = 0.229$ in the end of the echo train. Apparent diffusion coefficients for this experimental conditions vary within boundaries 0.229 and 0.404 for D_{app}/D_0. For a half filled lungs, D_{app}/D_0 varies between 0.237 and 0.461. Future implementation of the stretched exponential models for fitting will allow to obtain detailed and accurate D_{app}/D_0 histograms from the global CPMG measurements. A potentially wide range of CPMG parameters transforms it to a good tool for global D_{app} measurements in such heterogeneous systems as lungs.

4.3.6 Summary

The imaging abilities of our ultra-low field MRI setup were demonstrated. Series of 2D and 3D imaging experiments on lung phantoms were performed. A new imaging sequence (SLASH) was proposed for imaging at low fields. First tests of the SLASH sequence proving its strength and advantages were made. At low fields, the SLASH sequence definitely provides a better image resolution and SNR than FLASH sequence. Acquisition of the 2 gradient echoes in imaging experiments allowed to create ADC maps of the

Table 4.3: Parameters of the global CPMG experiments on the lung sample and corresponding b-values

#	**G_r, mT/m**	**τ_r, ms**	**b, s/cm^2**
1	1.98	10	1.356
2	1.98	3	0.037
3	0.99	6	0.073
4	0.495	12	0.147
5	0.2475	24	0.293
6	0.13475	48	0.695

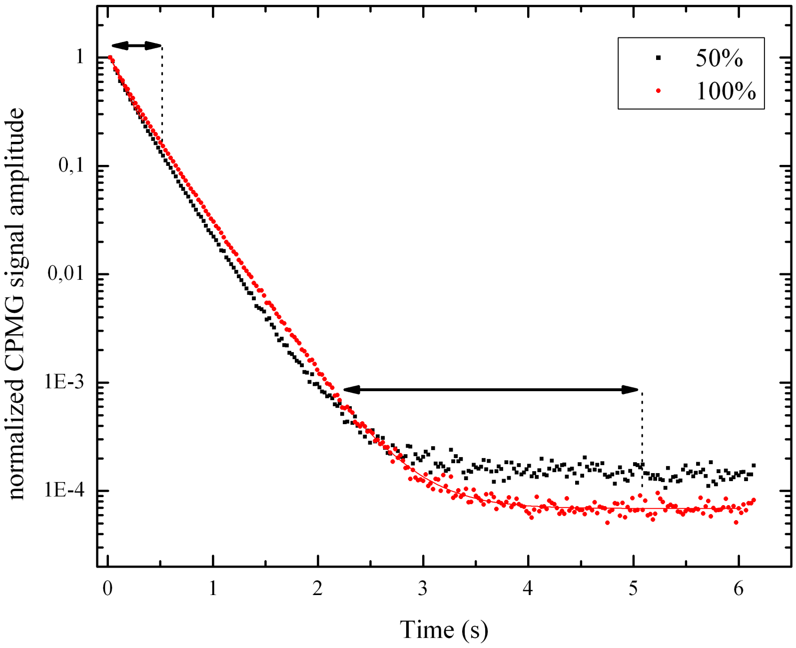

Figure 4.34: Typical echo amplitude decay trains in our CPMG experiments on preserved lungs filled with 4 cm^3 and 2 cm^3 of ^{3}He gas at 1 bar. Gradient strength G_r = 0.2475 mT/m and echo time T_{CP} = 24 ms. Regions of decay rate $T_{2,diff}^{-1}$ measurements are marked by the arrows

samples. The obtained ADC histograms are consistent with the results of global CPMG diffusion measurements in the same preserved lungs. The obtained ADC histograms are similar to in-vivo results, which makes this convenient inflatable porous system a relevant lung phantom for methodological studies. Low-field ADC measurements in lungs are immune to susceptibility gradients and can be performed over a wide range of diffusion times.

Conclusions

The active feedback scheme helps to avoid detection bandwidth problems at low fields. It stands out against the other possible bandwidth solutions like coupled coils or passive circuit damping. Combination of the preservation of high SNR values over the frequency region of interest and broad bandwidth makes it favorable solution to implement in the detection system at ultra-low fields. Moreover, the active feedback scheme allows for fast recovery of the detection system which makes it suitable for sequences with fast repetition rates. However, upgrades of the detection system for parallel imaging with coil arrays look like a potential solution for further image SNR improvement. Combination of inductively coupled coil arrays [70–72] and active feedback scheme should be considered in this case as a possible decoupling scheme. The active feedback scheme was implemented into the detection circuit of our MRI setup and then tested. Characterization of various parameters of MRI setup was made. It is suitable for various MRI and NMR experiments on HP gases. However, imperfect B_0 homogeneity places limitations on the observation times in the experiments. This problem can be solved by a new and more precise construction of the main coils.

Systematic diffusion attenuation measurements have been performed over very wide range of conditions with high SNR using CPMG and GE schemes in well-defined samples with cylindrical shape. Various diffusion conditions in these samples were studied by changing gas pressure, gradient strength and timing parameters. The results provide a wide body of data for direct comparison with existing theoretical models and experimental results at higher fields. It will help for precise understanding of signal decays, good control of data reduction and of extraction of "ADC values", which is an important point in lung MRI where regional ADC mapping has been proposed to be used in order to detect and stage various COPDs. At low field, a much wider range of gradients and timings can be used in the experiments. Use of long diffusion times was limited only by magnet inhomogeneity and only depends on the precision of its construction. However, carrying diffusion experiments at 2.7 mT field is limited at short diffusion times by impossibility to use high gradients values due to the effect of concomitant gradients. This effect plays an important role in the GE experiments and can make the results unreliable.

Ultra-low fields are suitable for MRI experiments. Preserved lung provide convenient phantoms for repeated imaging or diffusion measurements. Using lung phantoms or small animal lungs (for example, rat or rabbit lungs) with larger volume will allow to obtain 2D and 3D MR images with much better SNR. Experimental and diffusion conditions should be carefully checked before making every experiment to avoid having non reliable results of ADC measurements. Within a certain range of imaging parameters, diffusion regime inside the lungs does not depart from the expectations of free diffusion. At low fields, the new SLASH sequence that we have proposed provides better image resolution and SNR, than FLASH sequences. It makes it of special interest for static imaging. Further evaluation of the SLASH sequence at moderate magnetic fields is required to fully assess its potential interest for HP gas MRI.

Bibliography

[1] P.C. Lauterbur. Image formation by induced local interactions: Examples employing nuclear magnetic resonance. *Nature*, 242(5394):190–191, March 1973.

[2] M. S. Albert, G. D. Cates, B. Driehuys, W. Happer, B. Saam, C. S. Springer, and A. Wishnia. Biological magnetic resonance imaging using laser-polarized ^{129}Xe. *Nature*, 370(6486):199–201, July 1994.

[3] Edwin J.R. van Beek, Jim M. Wild, Hans-Ulrich Kauczor, Wolfgang Schreiber, John P. Mugler, and Eduard E. de Lange. Functional mri of the lung using hyperpolarized 3-helium gas. *Journal of Magnetic Resonance Imaging*, 20(4):540–554, 2004.

[4] R. W. Mair, M. I. Hrovat, S. Patz, M. S. Rosen, I. C. Ruset, G. P. Topulos, L. L. Tsai, J. P. Butler, F. W. Hersman, and R. L. Walsworth. 3he lung imaging in an open access, very-low-field human magnetic resonance imaging system. *Magnetic Resonance in Medicine*, 53(4):745–749, 2005.

[5] Trine Stavngaard, Lise Vejby Søgaard, Jann Mortensen, Lars G. Hanson, Jörg Schmiedeskamp, Anne Kiil Berthelsen, and Asger Dirksen. Hyperpolarised 3he mri and 81mkr spect in chronic obstructive pulmonary disease. *European Journal of Nuclear Medicine and Molecular Imaging*, 32:448–457, 2005. 10.1007/s00259-004-1691-x.

[6] Wolfgang G. Schreiber, Andreas E. Morbach, Trine Stavngaard, Klaus K. Gast, Anette Herweling, Lise Vejby Søgaard, Michael Windirsch, Jörg Schmiedeskamp, Claus Peter Heussel, and Hans-Ulrich Kauczor. Assessment of lung microstructure with magnetic resonance imaging of hyperpolarized helium-3. *Respiratory Physiology*

& Neurobiology, 148(1-2):23 – 42, 2005. Structure and Function in the Periphery of the Lung.

[7] Christopher P. Bidinosti, Jamal Choukeife, Pierre-Jean Nacher, and Geneviève Tastevin. In vivo nmr of hyperpolarized 3he in the human lung at very low magnetic fields. *J. Magn. Reson.*, 162(1):122 – 132, 2003.

[8] J. Parra-Robles et al. Theoretical signal-to-noise ratio and spatial resolution dependence on the magnetic field strength for hyperpolarized noble gas magnetic resonance imaging of human lungs. *Med. Phys.*, 32:221–230, 2005.

[9] Samuel Patz, Iga Muradian, Mirko I. Hrovat, Iulian C. Ruset, George Topulos, Silviu D. Covrig, Eric Frederick, Hiroto Hatabu, F.W. Hersman, and James P. Butler. Human pulmonary imaging and spectroscopy with hyperpolarized 129xe at 0.2t. *Academic Radiology*, 15(6):713 – 727, 2008.

[10] Leo L. Tsai, Ross W. Mair, Chih-Hao Li, Matthew S. Rosen, Samuel Patz, and Ronald L. Walsworth. Posture-dependent human He-3 lung imaging in an open-access MRI system: Initial results. *Acad. Radiol.*, 15(6):728–739, JUN 2008. International Workshop on Functional Lung Imaging, Philadelphia, PA, 2006.

[11] Andrew J. Swift, Jim M. Wild, Stan Fichele, Neil Woodhouse, Sally Fleming, Judith Waterhouse, Rod A. Lawson, Martyn N.J. Paley, and Edwin J.R. Van Beek. Emphysematous changes and normal variation in smokers and copd patients using diffusion 3he mri. *European Journal of Radiology*, 54(3):352 – 358, 2005.

[12] Chengbo Wang, Talissa A. Altes, John P. Mugler, G. Wilson Miller, Kai Ruppert, Jaime F. Mata, Gordon D. Cates, Larry Borish, and Eduard E. de Lange. Assessment of the lung microstructure in patients with asthma using hyperpolarized 3he diffusion mri at two time scales: Comparison with healthy subjects and patients with copd. *Journal of Magnetic Resonance Imaging*, 28(1):80–88, 2008.

[13] PJ Nacher, M Pelissier, and G Tastevin. Design and test of a magnet and gradient system for hyperpolarised gas lung MRI at ultra-low field. In *Proc. Intl. Soc. Mag. Reson. Med. 15*, page 3290, 2007. ISSN 1545-1428.

[14] M.P. Ledbetter, C.W. Crawford, A. Pines, D.E. Wemmer, S. Knappe, J. Kitching, and D. Budker. Optical detection of nmr j-spectra at zero magnetic field. *Journal of Magnetic Resonance*, 199(1):25 – 29, 2009.

[15] Stephan Appelt, Holger Kuhn, F. Wolfgang Hasing, and Bernhard Blumich. Chemical analysis by ultrahigh-resolution nuclear magnetic resonance in the earth/'s magnetic field. *Nat Phys*, 2(2):105–109, February 2006.

[16] Jeremy N. Robinson, Andrew Coy, Robin Dykstra, Craig D. Eccles, Mark W. Hunter, and Paul T. Callaghan. Two-dimensional nmr spectroscopy in earth's magnetic field. *Journal of Magnetic Resonance*, 182(2):343 – 347, 2006.

[17] Robert McDermott, Andreas H. Trabesinger, Michael Mack, Erwin L. Hahn, Alexander Pines, and John Clarke. Liquid-state nmr and scalar couplings in microtesla magnetic fields. *Science*, 295(5563):2247–2249, 2002.

[18] I. M. Savukov, S. J. Seltzer, M. V. Romalis, and K. L. Sauer. Tunable atomic magnetometer for detection of radio-frequency magnetic fields. *Phys. Rev. Lett.*, 95(6):063004, Aug 2005.

[19] I.M. Savukov, S.J. Seltzer, and M.V. Romalis. Detection of nmr signals with a radio-frequency atomic magnetometer. *Journal of Magnetic Resonance*, 185(2):214 – 220, 2007.

[20] Shoujun Xu, C. W. Crawford, Simon Rochester, Valeriy Yashchuk, Dmitry Budker, and Alexander Pines. Submillimeter-resolution magnetic resonance imaging at the earth's magnetic field with an atomic magnetometer. *Phys. Rev. A*, 78(1):013404, Jul 2008.

[21] F.E. Terman. *Radio engineer's handbook*. McGraw-Hill Book Company, 1943.

[22] Ahmad Raad and Luc Darrasse. Optimization of nmr receiver bandwidth by inductive coupling. *Magnetic Resonance Imaging*, 10(1):55 – 65, 1992.

[23] Hoult. Fast recovery, high sensitivity nmr probe and preamplifier for low frequencies. *Review of Scientific Instruments*, 50 Issue:2:193 – 200, 1979.

[24] Alain Louis-Joseph, Daniel Abergel, and Jean-Yves Lallemand. Neutralization of radiation damping by selective feedback on a 400 mhz nmr spectrometer. *Journal of Biomolecular NMR*, 5:212–216, 1995.

[25] P. Broekaert and J. Jeener. Suppression of radiation damping in nmr in liquids by active electronic feedback. *Journal of Magnetic Resonance, Series A*, 113(1):60 – 64, 1995.

[26] Baudin. *Dynamique RMN nonlineaire et renversement temporel dans les melanges d' 3He-4He hyperpolarises a basse temperature*. PhD thesis, Ecole Normale Superieure - Universite Paris VI (UPMC), 2011.

[27] Mehmet Bilgen. Inductively-overcoupled coil design for high resolution magnetic resonance imaging. *BioMedical Engineering OnLine*, 5(1):3, 2006.

[28] E. Stoltz. *Etude thermodinamique et de R.M.N. des melanges liquides d'Helium 3 polarise dans Helium 4*. PhD thesis, Ecole Normale Superieure - Universite Paris VI (UPMC), 1996.

[29] B. Villard. *Contributions a l'etude experimentale de l'Helium 3 liquide polarise*. PhD thesis, Ecole Normale Superieure - Universite Paris VI (UPMC), 1999.

[30] G. Tastevin, S. Grot, E. Courtade, S. Bordais, and P. J. Nacher. A broadband Yb-doped tunable fiber laser for ^{3}He optical pumping at 1083 nm. *Applied Physics B: Lasers and Optics*, 78(2):145–156, January 2004.

[31] Cavin Talbot, Marion Batz, Pierre Jean Nacher, and Geneviève Tastevin. An accurate optical technique for measuring the nuclear polarisation of he-3 gas. *J. Phys.: Conf. Ser.*, This volume:xxx, 2011.

[32] P.J. Nacher and M. Leduc. Optical pumping in ^{3}He with a laser. *Journal de Physique*, 46(12):2057–2073, 1985.

[33] E Baudin, K Safiullin, S W Morgan, and P J Nacher. An active feedback scheme for low field nmr experiments. *Journal of Physics: Conference Series*, 294(1):012009, 2011.

[34] Whittier R. Myers, Michael Mößle, and John Clarke. Correction of concomitant gradient artifacts in experimental microtesla mri. *Journal of Magnetic Resonance*, 177(2):274 – 284, 2005.

[35] Nathan Kelso, Seung-Kyun Lee, Louis-S. Bouchard, Vasiliki Demas, Michael Mück, Alexander Pines, and John Clarke. Distortion-free magnetic resonance imaging in the zero-field limit. *Journal of Magnetic Resonance*, 200(2):285 – 290, 2009.

[36] et al Xian Z. How to unwind in the low field limit. In *ISMRM07, book of abstract.*, 2007.

[37] Jaakko O. Nieminen and Risto J. Ilmoniemi. Solving the problem of concomitant gradients in ultra-low-field mri. *Journal of Magnetic Resonance*, 207(2):213 – 219, 2010.

[38] Dmitriy A. Yablonskiy, Alexander L. Sukstanskii, and Joseph J.H. Ackerman. Image artifacts in very low magnetic field mri: The role of concomitant gradients. *Journal of Magnetic Resonance*, 174(2):279 – 286, 2005.

[39] A. Abragam. *The Principles of Nuclear Magnetism.* Oxford at the Clarendon Press, 1961.

[40] E.M. Haacke et al. *Magnetic Resonance Imaging: Physical Principles and Sequence Design.* Wiley-Liss, 1990.

[41] Werner Heil, Hubert Humblot, Ernst Otten, Matthias Schafer, Reinhard Sarkau, and Michèle Leduc. Very long nuclear relaxation times of spin polarized helium 3 in metal coated cells. *Physics Letters A*, 201(4):337 – 343, 1995.

[42] E. Durand. *Imagerie de ventilation pulmonaire par RMN de l'hélium 3 hyperpolarisé.* PhD thesis, Université Paris-Sud XI, 2001.

[43] Terry Gullion, David B. Baker, and Mark S. Conradi. New, compensated carr-purcell sequences. *Journal of Magnetic Resonance (1969)*, 89(3):479 – 484, 1990.

[44] A.J. Shaka et al. An improved sequence for broadband decoupling: Waltz-16. *J. Magn. Reson.*, 52:335–338, 1983.

[45] J. Simbrunner and G. Zieger. Analysis of three-component composite 180° pulses. *Journal of Magnetic Resonance, Series B*, 106(2):142 – 146, 1995.

[46] Jim M. Wild, Martyn N.J. Paley, Magalie Viallon, Wolfgang G. Schreiber, Edwin J.R. van Beek, and Paul D. Griffiths. k-space filtering in 2d gradient-echo breath-hold hyperpolarized 3he mri: Spatial resolution and signal-to-noise ratio considerations. *Magnetic Resonance in Medicine*, 47(4):687–695, 2002.

[47] Mahesh et al. p. 178. In *ISMRM-99*, 1999.

[48] Bidinosti C Nacher PJ and G. Guillot. Decay analysis with limited snr - application to adc mapping. In *ESMRMB conference*, 2002.

[49] PT Callaghan. *Principles of nuclear magnetic resonance microscopy.* Oxford University Press, New York, 1991.

[50] M. D. Hurlimann, K. G. Helmer, T. M. Deswiet, and P. N. Sen. Spin echoes in a constant gradient and in the presence of simple restriction. *Journal of Magnetic Resonance, Series A*, 113(2):260 – 264, 1995.

[51] M. E. Hayden, G. Archibald, K. M. Gilbert, and C. Lei. Restricted diffusion within a single pore. *Journal of Magnetic Resonance*, 169(2):313 – 322, 2004.

[52] J. Parra-Robles, S. Ajraoui, M.H. Deppe, S.R. Parnell, and J.M. Wild. Experimental investigation and numerical simulation of 3he gas diffusion in simple geometries: Implications for analytical models of 3he mr lung morphometry. *Journal of Magnetic Resonance*, 204(2):228 – 238, 2010.

[53] Pabitra N. Sen, Martin D. Hürlimann, and Thomas M. de Swiet. Debye-porod law of diffraction for diffusion in porous media. *Phys. Rev. B*, 51(1):601–604, Jan 1995.

[54] Paul T Callaghan and Sarah L Codd. Generalised calculation of nmr imaging edge effects arising from restricted diffusion in porous media. *Magnetic Resonance Imaging*, 16(5-6):471 – 478, 1998.

[55] B. Saam, N. Drukker, and W. Happer. Edge enhancement observed with hyperpolarized 3he. *Chemical Physics Letters*, 263(3-4):481 – 487, 1996.

[56] Robertson. Spin-echo decay of spins diffusing in a bounded region. *Phys. Rev.*, 151:273–277, 1966.

[57] ER Weibel. *The Lung: Scientific Foundations, Vol. 1.* New York : Raven Press, 1991.

[58] Edwin J.R. van Beek, Jim M. Wild, Hans-Ulrich Kauczor, Wolfgang Schreiber, John P. Mugler, and Eduard E. de Lange. Functional mri of the lung using hyperpolarized 3-helium gas. *Journal of Magnetic Resonance Imaging*, 20(4):540–554, 2004.

[59] R.B. Bird J.O. Hirschfelder, C.F. Curtiss. *Molecular theory of gases and liquids.* New York : Wiley, 1954.

[60] David G. Norris and James M.S. Hutchison. Concomitant magnetic field gradients and their effects on imaging at low magnetic field strengths. *Magnetic Resonance Imaging*, 8(1):33 – 37, 1990.

[61] Dmitriy A. Yablonskiy, Alexander L. Sukstanskii, Jason C. Leawoods, David S. Gierada, G. Larry Bretthorst, Stephen S. Lefrak, Joel D. Cooper, and Mark S. Conradi. Quantitative in vivo assessment of lung microstructure at the alveolar level with hyperpolarized 3he diffusion mri. *Proceedings of the National Academy of Sciences*, 99(5):3111–3116, 2002.

[62] A. Haase, J. Frahm, D. Matthaei, W. Hanicke, and K. D. Merboldt. Flash imaging. rapid nmr imaging using low flip-angle pulses. *Journal of Magnetic Resonance (1969)*, 67(2):258 – 266, 1986.

[63] Steven D. Beyea, Bruce J. Balcom, Pablo J. Prado, Albert R. Cross, Christopher B. Kennedy, Robin L. Armstrong, and Theodore W. Bremner. Relaxation time mapping of shortt*2nuclei with single-point imaging (spi) methods. *Journal of Magnetic Resonance*, 135(1):156 – 164, 1998.

[64] Zhanjun Fang, Dieter Hoepfel, and K. Winter. Application of single point imaging (spi) to solid state materials. *Magnetic Resonance Imaging*, 19(3-4):501 – 503, 2001.

[65] Sankaran Subramanian, Nallathamby Devasahayam, Ramachandran Murugesan, Kenichi Yamada, John Cook, Andrew Taube, James B. Mitchell, Joost A.B. Lohman, and Murali C. Krishna. Single-point (constant-time) imaging in radiofrequency fourier transform electron paramagnetic resonance. *Magnetic Resonance in Medicine*, 48(2):370–379, 2002.

[66] M. Zaitsev, J. Hennig, and O. Speck. Point spread function mapping with parallel imaging techniques and high acceleration factors: Fast, robust, and flexible method for echo-planar imaging distortion correction. *Magnetic Resonance in Medicine*, 52(5):1156–1166, 2004.

[67] Salma Ajraoui, Kuan J. Lee, Martin H. Deppe, Steven R. Parnell, Juan Parra-Robles, and Jim M. Wild. Compressed sensing in hyperpolarized 3he lung mri. *Magnetic Resonance in Medicine*, 63(4):1059–1069, 2010.

[68] Simon Vinitski, Donald G. Mitchell, Jerzy Szumowski, D.Lawrence Burk Jr., and Matthew D. Rifkin. Variable flip angle imaging and fat suppression in combined gradient and spin-echo (grease) techniques. *Magnetic Resonance Imaging*, 8(2):131 – 139, 1990.

[69] Michael K. Stehling. Improved signal in flash by variable flip angles. *Magnetic Resonance Imaging*, 10(1):165 – 167, 1992.

[70] P. B. Roemer, W. A. Edelstein, C. E. Hayes, S. P. Souza, and O. M. Mueller. The nmr phased array. *Magnetic Resonance in Medicine*, 16(2):192–225, 1990.

[71] Daniel K. Sodickson and Warren J. Manning. Simultaneous acquisition of spatial harmonics (smash): Fast imaging with radiofrequency coil arrays. *Magnetic Resonance in Medicine*, 38(4):591–603, 1997.

[72] Klaas P. Pruessmann, Markus Weiger, Markus B. Scheidegger, and Peter Boesiger. Sense: Sensitivity encoding for fast mri. *Magnetic Resonance in Medicine*, 42(5):952–962, 1999.

Acknowledgements

I would like to thank Pierre-Jean Nacher and Geneviève Tastevin for the invitation and the opportunity to work in the Laboratoire Kastler Brossel for more than three and half years, warm reception, constant support and considerable assistance in any situation. I am very grateful to Pierre-Jean for a close cooperation, priceless supervision and updates of my point of view on experimental side of the scientific work.

I am thankful to my friends, and at the same time very nice colleagues, Bartosz Głowacz and Cavin Talbot for a warm friendship, valuable help. It was a pleasure to work together. Also many thanks to Cavin for a 24/7 gas production and visible improvement of my English, to Emmanuel Baudin for helpful and informative conversations and to Marion Batz for the help during her short stays in our lab.

I am gratefull to all members of the Laboratoire Kastler Brossel, especially to Fabien Souris, for making my life in France easier and more interesting. And thanks to the members of my very first lab (Magnetic Radiospectroscopy Laboratory and Department of Quantum Electronics and Radiospectroscopy of Kazan State University) for full-fledged trainings and a proper education.